LEVERAGING ARTIFICIAL NEURAL NETWORKS (ANN) FOR ENHANCING RELIABILITY AND PERFORMANCE OF PHASE CHANGE MATERIALS (PCM) IN THERMAL MANAGEMENT AND ENERGY STORAGE APPLICATIONS

A Thesis

by

ADITYA JAYKUMAR CHUTTAR

Submitted to the Graduate and Professional School of
Texas A&M University
in partial fulfillment of the requirements for the degree of

MASTER OF SCIENCE

Chair of Committee,	Debjyoti Banerjee
Committee Members,	Bryan Rasmussen
	Hadi Nasrabadi
	Debalina Sengupta
Head of Department,	Guillermo Aguilar

December 2021

Major Subject: Mechanical Engineering

ABSTRACT

Phase Change Materials (PCMs) have garnered significant attention over recent years due to their efficacy for thermal energy storage (TES) applications. High latent heat of PCMs enable enhanced storage densities which in turn translate into compact form factors of TES platforms utilizing PCMs. TES platforms mitigate the deviations between energy demand and supply, i.e., they absorb heat during periods of surplus in energy supply and release the stored energy during periods of deficit in energy supply. PCMs are envisioned for futuristic applications and are also deployed in a wide range of TES platforms in the industry - ranging from solar power plants, building energy management, HVAC, chemical process industries, waste heat recovery systems (such as desalination and food processing), domestic water heating, to thermal management of electronics (to list a few). Inorganic PCMs have high latent heat values (compared to organic PCMs) but suffer from several reliability issues. A major reliability issue with inorganic PCMs is the high degree of supercooling needed to initiate nucleation (which compromises the reliability, net energy storage capacity and power rating of the TES platform). “Cold Finger Technique (CFT)” can obviate these issues wherein a small fraction of the total mass of PCM is left in a solid phase to aid spontaneous nucleation (thus reliability is enhanced at a marginal expense to the net storage capacity while power rating of the TES remains unaffected). In this study, a machine learning (ML) technique, more specifically artificial neural networks (ANN), are implemented to enhance the efficacy of CFT. Temperature transients from PCM melting experiments are used as inputs to an ANN to

predict the time required to attain a predefined melt percentage in real time. Performance and efficacy of the machine learning techniques that utilize surface temperature transients (instead of measurement of PCM temperatures) is also investigated. Surface temperature-based monitoring strategies can be applied to PCM filled heat sinks to enhance operational reliability of thermal management platform using non-intrusive approaches (such as for electronics applications). The results show that an artificial neural network is capable of providing predictions *apriori* regarding the time to attain a chosen melt-fraction (e.g., 90% melt-fraction) with a considerable accuracy.

DEDICATION

This work is dedicated to my mother, father, and friends who have motivated and supported me during the course of my master's program.

ACKNOWLEDGEMENTS

I would like to thank my committee chair, Dr. Debjyoti Banerjee, and committee members, Dr. Bryan Rasmussen, Dr Hadi Nasrabadi, and Dr. Debalina Sengupta for their guidance and support throughout the course of this research.

I would also like to acknowledge Mr. Ashok Thyagrajan for his guidance during the experimentation phase of my research. I also extend my thanks to Mr. Nandan Shettigar for his early research in the Multiphase Flow and Heat Transfer Laboratory.

Finally, thanks to the faculty and staff of the J. Mike Walker ’66 Department of Mechanical Engineering at Texas A&M University, College Station for a great educational experience.

CONTRIBUTORS AND FUNDING SOURCES

Contributors

This work was supervised by a thesis committee consisting of Professor Debjyoti Banerjee (advisor) and Professor Bryan Rasmussen of the Department of Mechanical Engineering, Professor Hadi Nasrabadi of the Department of Petroleum Engineering, and Dr. Debalina Sengupta of the TEES Gas & Fuels Research Center.

All other work conducted for the thesis was completed by the student independently.

Funding Sources

Graduate study was supported by an assistantship from Engineering Academic and Student Affairs, Texas A&M University, College Station. This work was also made possible in part by Texas A&M Triads for Transformation (T^3) grant funded by the Office of the Vice President for Research (VPR).

The contents of this work are solely the responsibility of the authors and do not necessarily represent the official views of the Texas A&M University.

NOMENCLATURE

PCM	Phase Change Material
ANN	Artificial Neural Network
MLP	Multilayer Perceptron
LHTESS	Latent Heat Thermal Energy Storage System
TES	Thermal Energy Storage
RBF-NN	Radial Basis Function Neural Network
AWG	American Wire Gauge
CFT	Cold Finger Technique
u_{DAQ}	Uncertainty due to DAQ precision (%)
u_s	Statistical uncertainty (%)
u_t	Uncertainty due to thermometer precision (%)
T	PCM temperature (^oC)
T’	Cylinder Surface Temperature (^oC)
t	Elapsed time (s)
t_m	Total time taken by the PCM to reach a melt-fraction m (s)
t'_m	Time remaining to reach melt-fraction m (s)
V	Actual volume of PCM in the graduated cylinder
V'	Apparent volume of PCM in the graduated cylinder

Greek letters

τ'_M	Non-dimensional time remaining to reach melt-fraction M.
τ_m	Non-dimensional elapsed time w.r.t. melt-fraction m.
ρ	Density (kg/m^3)
σ	standard deviation

Subscripts

S	solid
L	liquid
m	melt-fraction (%)
amb	ambient

TABLE OF CONTENTS

Page

LIST OF FIGURES

Page

LIST OF TABLES

Page

CHAPTER I

INTRODUCTION

1.1 PCMs for Latent Heat Thermal Energy Storage

Thermal Energy Storage (TES) platforms mitigate the deficits during unbalanced fluctuations in energy supply and demand. Latent heat thermal energy storage systems (LHTESS) are an effective means to store energy in small form factors and they provide the added benefit of yielding higher systemic efficiencies due to their operating envelope being limited to a narrow temperature range (i.e., the phase transition temperature). TES platforms leveraging Phase Change Materials (PCM) have been explored for a variety of applications, such as: in building energy management and concentrated solar power generation [1, 2]. One of the most promising applications of PCM based LHTESS is a supplemental cooling platform for electric power plants as it can relieve the stress on freshwater resources for cooling [3].

A variety of factors (e.g., rapid economic development, population explosion, and global climate change) have led to rising demands for freshwater resources. An ever-increasing strain on these resources have led to the interdependencies in the food-energy-water (FEW) nexus. The issues associated with FEW nexus are predicted to intensify in the near future. A major proportion of the total electricity generation in the United States (and globally) is from thermoelectric power plants - which use coal, oil, natural gas, or nuclear fissionable materials as fuel (and in turn, require the cooling of steam from the turbine exhaust). The cooling platforms typically rely on cooling towers that consume

large amounts of freshwater resources. In 2015, thermoelectric electric power producers alone consumed 4.3 billion gallons of freshwater per day [4].

As mentioned before, for power plants operating on the Rankine cycle, the steam powered turbines require cooling of the steam exhaust in order to generate electric power. Conventionally, cooling water derived from cooling towers is used condense the steam from the turbine exhaust. In this process, the evaporative cooling strategies used in cooling towers (to obtain the cooling water that are fed to the condensers) result in consumption of massive amounts of freshwater resources. In the United States, 40 % of the total water withdrawals were by thermoelectric power plants. Much of this water (85-95%) is utilized for operating the cooling towers. In 2015, power plants withdrew 133 billion gallons of surface water per day, 72% of which were freshwater withdrawals [4]. After withdrawal, significant portion of the water is lost through evaporation while a major portion of the consumed water is discharged at a higher temperature and is typically diverted into neighboring waterbodies (the hot water discharged from the power plants - in turn - stresses the aquatic eco-system). For coal fired power plants utilizing wet cooling (which provides better systemic efficiencies and lower cost of power), more than 80% of the withdrawn water is consumed in this process [5]. Thus, energy generation is highly dependent on the accessibility to and availability of freshwater resources. However, the conventional cooling methods are not sustainable in the long run due to declining water resources in various regions of the world. Freshwater scarcity will in turn cause heavy reliance on energy intensive sources of water supply such as desalination. It is projected

that desalination shall account for 15% of the end energy use in the Middle East in 2040 [6].

Dry cooling (instead of 'wet' cooling) can decrease the consumption of cooling water for steam condensation by 95%. These systems cool or condense a fluid in a heat exchanger without using water. Fig. 1 shows a schematic of a dry cooling system. Dry cooling platforms condense the steam from the turbine exhaust - directly in finned-tube air-cooled heat exchanger platforms and return the condensate to the boiler (without using any makeup water). Indirect dry cooling configurations circulate water through a condenser and a convective air-cooled heat exchanger in a closed loop. Unsurprisingly, dry cooling systems suffer from a couple of challenges making them unattractive for power producers. Firstly, the air-side heat transfer coefficients are significantly lower than the water side heat transfer coefficients. This translates into large surface area requirements. Larger systems require higher upfront investments and operation costs. Secondly, from a thermodynamic standpoint, the lower limit of the steam condensation temperature in an air-cooled condenser is the ambient dry bulb temperature. Whereas, for evaporative cooling ('wet' cooling), the steam condensation takes place at the ambient wet bulb temperature. On an average, the dry bulb temperature is higher than the wet bulb temperature by about 3-5 ^{o}C [7]. A higher temperature at the turbine exhaust means a loss in power output and lower systemic efficiencies (thus resulting in higher cost of electrical power production). In addition, on hot days the systemic efficiencies and reliability are severely compromised for power plants that are dry-cooled.

Since the performance of dry cooled power plants are highly sensitive to ambient air temperatures, supplemental cooling solutions can alleviate the limitations imposed by the inefficiencies inherent in air cooling, primarily due to temperature excursions. Hot days lead to elevated turbine back pressures, thus decreasing the power output. Ultimately, the energy conversion efficiency of the power plant is diminished on the days with elevated temperatures.

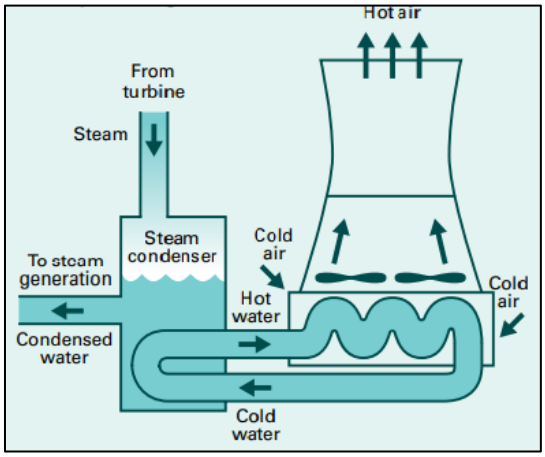

Figure 1 Schematic of a dry cooling sytem. Reprinted from [4]

A supplemental cooling platform can be realized typically by deploying LHTESS (such as by utilizing a suitable PCM candidate). In such a system, during the day, the air temperature is lowered by cooling it in the LHTESS prior to passing it into the air inlet section of the air-cooled steam condenser (in which case, the PCM in the LHTESS melts while cooling the incoming air from the ambient). Alternately, the steam can be condensed directly in the LHTESS platform (while melting the solidified PCM in the process). During the night, the stored energy in the melted PCM is released to the ambient (which

is typically at a significantly lower temperature at night) and in the process the PCM is solidified during the cooler night time conditions.

Typically, inorganic PCMs (such as salt hydrates) pack in higher levels of specific enthalpy for phase change, than that of the organic PCMs. For salt hydrates - the storage temperatures (i.e., the phase change temperature) can be tuned by varying the water content in the chemisorbed states. This customization capability highlights the versatility of inorganic PCMs, particularly salt hydrates with varying levels of hydration, in supplemental cooling platforms for a wide range of operating conditions (and therefore can be designed to respond to wide variability in climatic or ambient conditions).

A system perspective can be adopted to appreciate how TES can enhance the resilience of a dry-cooled powerplant. Resilience of a system refers to its ability to decrease the impact of negative shocks on its performance and respond to the disruptions in a favourable manner. Creation of resilient industrial processes can reduce the losses faced by the stakeholders and end users in the face of expected or unexpected disaster. These disasters could include natural calamities, economic collapses or even terrorist and cyber-attacks. With industrial processes in mind, a set of 12 principles/ strategies can be applied to create disaster resilient designs [8]. One of the strategies is reliability — i.e., the ability of the designed process to function without failing. Reliability can be defined as “the probability that a unit shall perform its intended function until a specified point in time under *encountered* use conditions” [9]. The conditions of operation are critical in determining a system’s reliability. This determination often involves modelling the probability of failure and time to failure.

For dry cooled powerplants operating in arid climates, the summer daytime temperatures can be high enough to warrant a powerplant shutdown. The increasing turbine backpressures pose an acute risk of damage to the turbine itself. These temperature excursions can lead to the disruptions in operations. Currently, the emergency response for powerplant operators is to shut down the powerplant which is not a hallmark of a resilient design. Resilient systems are fail-safe by design, adapt to changing conditions, and recover rapidly. Figure 2 shows the various stages that a resilient system goes through following a disruptive event [8]. For dry cooled powerplants thermal energy storage is an example of a design which adapts the system to respond to high ambient temperature conditions. During the night, when the temperatures are lower, the process flow changes to ensure solidification of the PCM, thus displaying reconfigurability (which is yet another strategy to design resilient processes). Hence, in a broad sense, TES using PCM is a strategy for a resilient design of a dry-cooled powerplant.

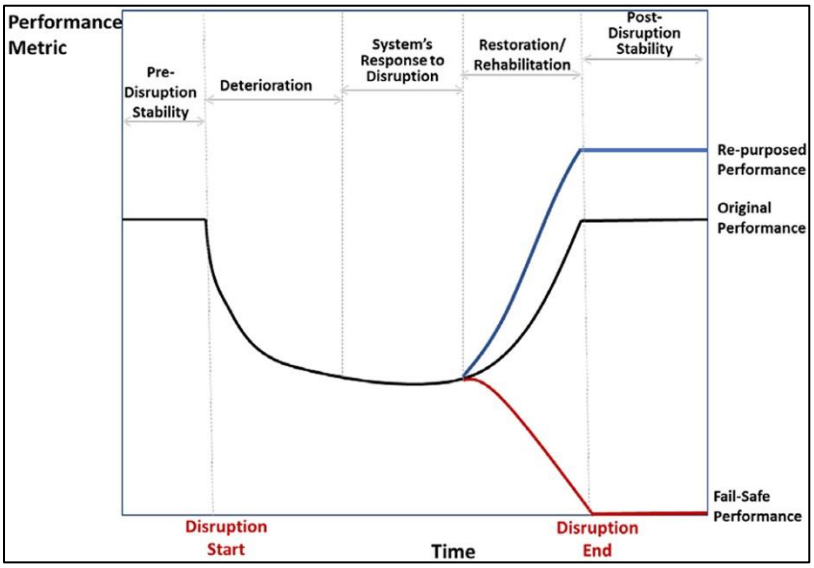

Figure 2 Stages of resilience after a disruptive event. Reprinted from [8]

1.2 PCMs for Electronics Thermal Management

Thermal management of electronics is important for maintaining their operating temperatures since lower operating temperatures are necessary for extending their life-span and reliability of operation as well as for maximizing their performance. Progressive miniaturization of device features in electronics products (such as computers and processors) has resulted in a widespread deployment of electronics that are ubiquitous in domestic and industrial scenarios. The sharp rise in the demand for high performance computing in every aspect of consumer and commercial segments (e.g., internet-of-things/ IoT, block-chain commerce, social media, GPS navigation in cell phones using cloud computing, etc.) is fueling the trend for miniaturization and real-time computing at a rapid pace. Consequently, heat flux and temperature levels in electronics are escalating, in devices ranging from hand-held products (e.g., cell phones, gaming consoles, etc.) to large-scale platforms (e.g., computing farms and data centers). However, semiconductor reliability and performance diminish at elevated operating temperatures as well as non-uniformities in temperature distribution within chips and packages (e.g., due to formation of hot spots arising from transient surge in computing threads allocated non-uniformly to processor arrays). The rate of heat removal has to be greater than or equal to its generation in order to maintain the right junction temperatures. In addition, the acute monitoring and reliable management of transient and localized hot spots in individual chips and packages (particularly in computer-server farms) is needed urgently. Higher junction temperatures result in a shortened lifespan of a semiconductor device, particularly due to hot spots (as

it causes local thermo-mechanical stresses that reduces the operational life-span of the chips and packages). In fact, the chances of failure increase exponentially, if a localized area on a chip heats up beyond the specified temperature limits [10]. This result is based on the widely known Black's equation [11]. Moreover, integration—a direct consequence of miniaturization—has resulted acute severity in non-uniform heat flux generation within individual chips and packages. The rapid progression of miniaturization in semiconductor technologies has largely followed the famous Moore's law [12]—which simply states that the number of transistors on a microchip will double every two years. However, the doubling rate has started to falter in recent times, primarily due to the failure of the industry in meeting the heat dissipation loads and temperature uniformity requirements [13]. Removal of a high heat flux at appropriate temperatures is a constant challenge faced by the electronics industry. Researchers have considered varied approaches for electronics cooling over the years.

Traditional cooling techniques typically consist of external air-cooled heat sinks, and are inadequate for modern electronics applications. Emerging technologies include: (i) Heat pipes; (ii) Heat pumps; (iii) Microchannels; (iv) Spray cooling; (v) Phase Change Material (PCM) based cooling strategies; (vi) Free cooling; (vii) heat-sinks leveraging liquid-vapor phase change; and (viii) Thermoelectric cooling [14]. A number of studies on these techniques have highlighted their efficacy [15-17]. Among these, passive cooling methods based on PCMs has garnered significant attention in recent times. Properties like high latent heat, narrow operating temperature envelope, high specific heat, and small volume expansivity (during melting) translate into compact form factors. A numerical

study of a novel design of a heat sink utilizing hollow aluminum pin fins filled with PCM showed that a small amount of PCM could stabilize the microprocessor temperatures [18]. An experimental study of cooling of a personal digital assistant (PDA) using n-eicosane as a phase change material for heat storage showed that the PCM stabilized the junction temperatures and the effectiveness of such a heat storage unit (in terms of storage capacity and power ratings) depends on the amount of PCM used as well as the shape of the package [19]. PCMs can be used for thermal control of intermittently used electronics such as mobile phones, digital video cameras, wearable electronics (or portable electronics) and similar electronics devices. The thermal resistance of the device (which in turn governs the power rating) and storage capacity of the TES platform (i.e., the PCM mass and shape of the package) are the critical design parameters in this type of a passive system where the prior knowledge of the duty cycle is also important [20]. A PCM based heat sink (where the PCM was deployed typically within the cavities of the packaging in the heat sink)—placed on a plastic quad flat package mounted on a printed circuit board—was shown to have an improved cooling performance as compared to the case without PCM at high power levels ($q > 2$ W) [21]. Another study reported that at higher power levels, the operation time (i.e., time required for the heat sink to reach a set temperature) was enhanced for a given volume of PCM in the heat sink (compared to the case without PCM) [22]. It has been established that combining a PCM based heat sink with forced air convection is superior in reducing peak temperatures than a traditional air-cooled heat sink without PCM. Moreover, the latent heat of the PCM extends the duration of operation and delays the time required for reaching the peak temperature. However, in order for TES

platforms to be effectively used in thermal management of electronics - prior knowledge of the typical duty cycle is crucial for ensuring success of the design and in operation. In addition, PCMs should exhibit the following characteristics—(i) appropriate phase transition temperature; (ii) low volume expansion; (iii) high thermal conductivity, latent heat, and specific heat; (iv) material compatibility (non-corrosive) including chemical stability; (v) low supercooling during freezing (or preferably, no supercooling); (vi) low cost [23]. All the criteria can be seldom met and often a trade-off must be made for achieving the desired design conditions.

1.3 Supercooling in PCMs

Based on their chemical composition, PCMs can be categorized as follows: (1) organics, (2) inorganics, and (3) eutectics. Examples of organic PCMs include paraffins, waxes and bio-derived fats (long-chain fatty molecules or organic polymer materials). Salt hydrates such as $LiNO_3 \cdot 3[H_2O]$ and metallics like Gallium are popular inorganic PCMs. Eutectics are a combination of two or more PCMs with similar melting and freezing points (e.g., metal eutectics and metallic or semiconductor-based alloys). Salt hydrates have a higher volumetric energy storage capacity (40-125 kWh/m^3) than paraffins (40-60 kWh/m^3) due to their high densities [24]. So, in systems where volume is a constraint, salt hydrates can be a better option. However, salt hydrates undergo incongruent melting and often require large supercooling to initiate nucleation. When salt hydrates melt, the solid crystal structure breaks and releases chemisorbed water molecules (depending on their stoichiometric ratio for the chemical hydration process). The amount of water is not

always sufficient to dissolve the anhydrous salt completely causing incongruent melting. As a result, upon freezing, the salt fails to recombine with water immediately. On the other hand, supercooling is the phenomenon where solidification is achieved only when the PCM temperature is significantly lower than the thermodynamic phase transition temperature. At the fusion temperature, the rate of nucleation is very low. A low nucleation rate limits the efficacy of a PCM heat sink—as the latent heat is not released spontaneously. In a TES application, supercooling hinders the reliability of the energy storage platform and often compromises their performance metrics.

Methods to address supercooling can be categorized into passive and dynamic techniques. Addition of nucleating agents is a widely studied passive technique to mitigate supercooling. Using Borax as a nucleating agent (at 1.9% mass fraction) the degree of supercooling for a thickened sample of Glauber's salt was reduced from 15 ^{o}C to 3~4 ^{o}C [25]. Supercooling in sodium acetate trihydrate (SAT) was entirely obviated upon addition of aluminum nitride (AlN) nanoparticles (at mass fraction of 5%) and mixed with carboxyl methyl cellulose (CMC) as a thickening agent at 4% mass fraction [26]. Supercooling in SAT was also reduced by adding silver nanoparticles and the authors reported that the efficacy of this additive is a function of the concentration of the particles [27]. Similarly, copper hydroxyl nitrate hydrate (CHNH) catalyst enhances nucleation in lithium nitrate trihydrate (LNT). Models suggest that the minimizing the mismatch in the lattice structure of the salt and the additive (e.g., catalyst) is effective in reducing the degree of supercooling [28]. Zinc hydroxyl nitrate and zinc oxide nucleators were shown to reduce the supercooling in zinc nitrate trihydrate by 8.8 ^{o}C and 8.2 ^{o}C, respectively [29]. The

effect of various additives (e.g., nucleating agents) on reducing the degree of supercooling in salt hydrates has been reviewed extensively [30, 31].

In contrast to the heterogenous seeding techniques, the 'cold finger technique' (CFT) is an example of a homogenous nucleation technique where a small portion of the salt hydrate is un-melted and maintained in a solid phase (which is in contact with the liquid phase), and this un-melted portion is very effective in promoting spontaneous nucleation. A localized spot can be maintained in a solid phase by adding extra insulation or exerting pressure. Another way to implement the cold finger technique is to halt the melting process of the PCM just prior to achieving complete melting and starting the freezing process prior to complete melting (during thermocycling involving repeated melting and solidification). For instance, the heat source could be removed when the PCM reaches 85% melt, leaving 15% un-melted to serve as the promoter for spontaneous nucleation (when the freezing cycle is initiated). Hence, by leveraging CFT spontaneous nucleation can be achieved quite effectively albeit at the expense of a reduction in the energy storage capacity. For a TES application deployed for thermocycling (i.e., repeated melting and freezing cycles), CFT afforded a reliable and effective strategy for reducing the degree of supercooling in LNT (from 16 ^{o}C for completely melted mass of PCM) to 0.5 ^{o}C ~ 1 ^{o}C for over 800 cycles of repeated melting and freezing [32].

A successful implementation of this technique depends on the ability to reliably control (and also predict) the duration of the melting cycle of the PCM. A possible way to implement this technique necessitates achieving a particular target value of melt-fraction (e.g., 90% melt-fraction) with sufficient precision and accuracy for the purpose of

maximizing the storage capacity while also achieving the desired reliability of operation. When the system reaches this target point (say 90% melt-fraction), the solidification process could be initiated (i.e., without proceeding to a 100% melt-fraction). Ideally, the time to reach the target point needs to be predicted in real time as the PCM undergoes melting. Hence, combining CFT with a time forecasting technique can successfully mitigate supercooling. Machine learning (ML) algorithms can be of significant utility, especially in situations mentioned here for LHTESS platforms (e.g., using salt hydrates), where there is a lack of accurate theoretical models describing coupled and non-linear thermal-hydraulic behavior at the system level. ML models are inherently robust as they are device independent and are based on behavioral data. ML models are most effective where large volumes of prior data are available for "training".

1.4 Artificial Neural Network Principles

Artificial neural networks are capable of fitting complex, non-linear mappings between inputs and outputs [33]. An ANN can be defined as a parallel distributed processing system capable of learning from experiences [34]. ANNs are built to construct relationships between parameters without detailed knowledge about the system. The most basic kind of an ANN is the fully connected multilayer perceptron (MLP) model. In such networks, the neuron is the fundamental processor of information. These neurons (also referred to as 'nodes') are arranged in progressive layers. In case of a fully connected MLP, a neuron receives and processes the input from the neurons in the previous layer into an output. A neuron can be mathematically characterized by: (i) bias (***b***); and (ii)

activation function (***f***). Each synaptic connection is associated with a weight (***w***). Inside every node the activation function acts on the weighted inputs from the previous layer. Let the subscript ***n*** denote the serial number of the layer. The input vector to the layer can be represented by $\boldsymbol{a_n}$. The functional relationship between the output of one layer (which is the input to the subsequent layer, $\boldsymbol{a_{n+1}}$) is shown below:

$$\boldsymbol{a_{n+1} = f(w^T a_n + b)} \quad (1)$$

Developing an ANN involves three steps: training, validation, and testing. The input output data can be divided into three sets, i.e., one unique set of data that is dedicated for each stage. The weights and biases are randomly initialized. Output is obtained using these random parameters. A cost function is implemented to quantify the degree of disagreement between the generated output and the actual output (which serves as the validation step). The error values obtained in the validation step is propagated backwards from the output to the input layer which is then used for adjusting the weights and biases. A gradient descent algorithm is typically applied to modify the biases and weights to optimize (minimize) the cost function. This combination of feedforward and backpropagation process is continued iteratively until the target error (or desired value of the gradient) is achieved; or the number of passes (epochs) reaches a specified value. A typical example of the cost function is the sum of squared errors (SSE) on the validation dataset depicted in Equation (2) where ***p*** is the actual output and ***p'*** is the value predicted by the ANN model at any given iteration. Also, ***N*** denotes the size of the validation set. The third stage involves testing the efficacy of the ANN on the test dataset which was not encountered by the ANN during the training or the validation stage.

$$\boldsymbol{SSE} = \sum_{\boldsymbol{i=1}}^{\boldsymbol{N}} (\boldsymbol{p} - \boldsymbol{p'})^{\boldsymbol{2}} \qquad (\boldsymbol{2})$$

Radial Basis Function Network (RBF-NN) is another class of ANNs which has gained popularity particularly in modelling thermophysical properties, such as that of nanofluids [35]. RBF-NNs were first introduced by Broomhead and Lowe [36]. This kind of an ANN is characterized by three layers – input, hidden, and output layer. Application of RBF-NN has been popular in contemporary literature reports, especially for function approximation. The fundamental difference between an MLP model and an RBF-NN network is in the computation taking place in the neurons. A radial basis function, $\boldsymbol{\varphi}$ is the activation function in the latter type of an ANN which operates on the Euclidean norm between the neuron center and the input vector. A connection weight then acts on the resultant to yield an output as shown below:

$$\boldsymbol{y}\,(\boldsymbol{x}) = \sum_{\boldsymbol{i=1}}^{\boldsymbol{n}} \boldsymbol{w_i}\boldsymbol{\varphi}(\|\boldsymbol{x} - \boldsymbol{x_i}\|) \qquad (3)$$

1.5 Motivation and Goals

The availability of freshwater is becoming increasingly scarce and costly due to increased demand while it is geographically unevenly distributed (with a few regions having large freshwater resources while geographical regions with arid climates facing severe shortages and scarcity along with other regions facing acute seasonal fluctuations or severe flooding that is accelerated by climate change). Hence, with rapid population growth and increased demand of freshwater resources along with impacts of climate

change, there is an acute strain on this valuable resource. Power plants consume trillions of gallons of freshwater annually. It may be noted that 36% of the thermoelectric power production capacity in the U.S. is from powerplants that use once-through cooling systems [37]. These plants withdraw large amounts of water from nearby waterbodies and release it back at higher temperatures (that can cause issues associated with thermal pollution of water bodies – such as biofouling and adversities to flora and fauna in the eco-systems associated with these water bodies). The sustainability of such cooling system is a topic of concern. Innovations are sought in the field of dry cooling technologies. Current state of the art of dry cooling technologies is insufficient and are a detriment to achieving satisfactory levels of plant efficiency and therefore to their techno-economic feasibility.

Supplemental cooling systems are needed to facilitate dry cooling particularly in warmer regions of the world. PCM based LHTESS can be a potential solution to provide additional cooling and mitigating these debilitating issues.

On the other hand, rapid advances in electronics have resulted in a superior performance that have accrued from squeezing larger number of device features into progressively smaller length scales. As a result, waste heat generation has increased exponentially while the operating temperature limits are at the risk of being violated (thus degrading device performance, reducing the operational life-spans and compromising the operational reliability due to frequent formation of transient, localized and acute hot-spots; which in turn has increased the frequency of failures that have resulted from maldistribution of debilitating thermo-mechanical stresses within the electronics chips and packages). Hence, efficient cooling technologies are needed to avoid device failure due to

overheating and maldistribution of temperature profiles within these electronics devices and packages. PCMs can rapidly absorb the excess heat while melting partially in the process within the contained packages, thus damping the peaks in temperature fluctuations caused by the maldistribution of the heat released during intermittent operation (duty-cycles) and can slowly release the excess heat while solidifying back to the initial state (when the device is idle). Thus, this strategy can extend the operational capabilities of the heat sink under critical load conditions [38]. As a result, the heat sinks can be designed for base load while the TES platform (with PCM) can be designed to absorb the peak loads and therefore deployed in tandem for meeting the supplemental cooling needs.

Passive thermal management for electronics using phase change materials (PCM) has significant potential in this regard. Passive systems are simpler and require less maintenance (since there are no moving parts). For this application, an ideal PCM should exhibit favorable material and thermophysical properties, such as, high heat capacity, high latent heat of fusion, and small volumetric changes during phase transition (with preferably, tunable melting or freezing points). Such properties enable high energy storage capacities to be achieved in compact form factors while enhancing reliability of operation and extending the life-span of electronics devices and packages.

For the two applications outlined above, salt hydrates are particularly promising PCM candidates due to their favorable thermophysical and thermodynamic properties. However, one of the main drawbacks of salt hydrates is the need for supercooling to initiate nucleation. The motivation of this study is to enhance the systemic reliability of a PCM-based energy storage. For electronics thermal management applications,

supercooling hampers the effectiveness of a PCM filled heat sink. Hence, obviating the need for supercooling can be projected to have a significant impact on the state of the art. It is preferable that the temperature distribution of the electronics devices and packages are monitored in a non-intrusive manner (as insertion of additional sensors into packages can be a costly maneuver and add to the manufacturing as well as operational costs). Surface mounted temperature sensors can be an effective way to monitor the thermo-mechanical "health" of electronics devices. A control scheme that is effective and efficacious (by leveraging surface mounted sensor arrays) is highly desirable. Also, there is an acute need for robust forecasting strategies that minimize the number of sensors required for these monitoring and control schemes.

Hence, a goal of this study is to develop a novel method and to test the efficacy of this novel method for implementing the "cold finger technique (CFT)" with the intent of obviating supercooling, particularly for inorganic PCMs. An additional goal of this study is to explore the efficacy of this novel method for TES applications involving both: (a) monitoring the PCM temperature (for mitigating freshwater usage in power production applications); and (b) monitoring the surface (package) temperature of the PCM containment (for electronics thermal management applications). Artificial neural networks (ANN) based techniques are therefore utilized to use the measured temperature values as inputs in order to predict in real-time - the time remaining to reach a predefined melt-fraction as the PCM melts. Secondly, a large volume of experimental data was generated in this study (temperatures recorded by an array of thermocouples, thermography images recorded by Infra-Red (I.R.) cameras, melt-fraction data, etc.) with the goal of validating

the efficacy of the ANN models for future studies involving computational fluid dynamics (CFD) simulations. These data sets can also be utilized in the future for developing machine learning (ML) based algorithms (that leverage image processing of the thermography images recorded by the I.R. cameras at fixed intervals in time and are linked to the particular melt-fraction estimated using the thermocouple data obtained in tandem with the acquisition of these I.R. images) for predicting the melt-fraction, perhaps based on just a single I.R. image. Such future approaches envisioned from this study will magnify the impact of ANN and ML models in enhancing the efficacy of TES (PCM) platforms.

1.6 Objective and Scope

The objective of this study is to accurately predict in real time, the time remaining to reach a preselected melt percentage for a PCM undergoing phase transition from solid to liquid. The intention is to use the temperatures recorded at specific locations within the melting mass of PCM - as inputs to an ANN model – for the purpose of estimating the instantaneous values of melt-fraction as well as the time remaining to attain a preselected melt-fraction. With electronics applications in mind, another objective is to use surface temperature data (recorded by a fixed set of thermocouples that are mounted on the exterior surface of the containment wall) for estimating the time remaining to achieve a desired (and set) value of melt-fraction. Hence, the efficacy of two different approaches utilizing the same ANN model is compared. These are:

1. using temperature data from sensors immersed within the body of the PCM at locations corresponding to meniscus levels of the liquid coinciding with specific

values of melt-fraction of the PCM (i.e., transient PCM-temperature data for training of the ANN model); and

2. using temperature data from sensors mounted on the surface of the cylindrical container at locations corresponding to meniscus levels of the liquid coinciding with specific values of melt-fraction of the PCM (i.e., transient surface-temperature data for training of the ANN model).

Since ANNs fall under the category of supervised learning, labelled data is needed for the training step. The data for training the network is obtained from PCM melting experiments. The ability to make *apriori* predictions (i.e., forecasting using ANN techniques) is significant for power generation (improving reliability by using supplemental cooling, eliminating freshwater usage, etc.) and electronics thermal management (reducing hot spots, extending life-span of electronics, enhancing computing performance, elevating operational reliability, etc.) as it enables the successful implementation of the cold finger technique (CFT) and thus obviates supercooling.

The scope of the experiments is limited to a specific PCM only (since this study is focused on proving the feasibility of the proposed ANN techniques and the focus of this study is not on improving the performance of any PCMs). PureTemp 29 (with a melting point of 29 ^{o}C) is selected for these experiments and for obtaining the data set needed for both developing and validating (training and optimizing) the ANN models as well as testing the efficacy of the predictions (forecasting in real-time) from the ANN models. Ease of performing the experiments (with minimal complications) and reliability of acquiring the temperature data (as well as the desire for maintain simplicity of the

experimental apparatus) guide the selection of this particular PCM. Further, the topology of the artificial neural network (ANN) is fixed. Optimization of the ANN topology is out of scope of this study – since proving the feasibility of this strategy is the main goal of this study. The neural network is composed of three hidden layers and each layer has 512 nodes. The Rectified Linear Unit (ReLU) activation function is used in the network nodes. The cost function for the training purpose is the Mean Squared Error (MSE). ADAM optimizer is deployed as the gradient descent algorithm.

CHAPTER II

EXPERIMENTAL METHODS AND DATA PROCESSING*

2.1 Experimental Apparatus and Procedure

The experimental apparatus and procedures (to generate the raw data which is subsequently modified for ANN training purposes) is presented in this chapter. The description of the experimental procedure is categorized as follows:

1. Calibration of thermocouples (using water bath).
2. Calibration of the thermocouple location and placement (using measured aliquots of water).
3. Melting-cycle experiments (for acquisition of transient PCM-temperature and transient surface temperature data) along with flow visualization (using digital camera) and thermography (using Infra-Red / I.R. Camera).

The PCM melting experiments involve melting a known volume of PCM (that is completely solidified initially) in a graduated measuring cylinder with thermocouples located at certain heights from the bottom of the cylinder. The thermocouples were mounted at specific locations – both within the volume of the cylinder as well as on the outside surface of the cylinder. These locations were determined strategically in order to measure the temperature transients at particular heights (from the bottom).

---

*Part of the data reported in this chapter is reprinted with permission from "Leveraging Machine Learning (Artificial Neural Networks) for Enhancing Performance and Reliability of Thermal Energy Storage Platforms Utilizing Phase Change Materials" by Aditya Chuttar, Ashok Thyagarajan, and Debjyoti Banerjee, 2021. *Journal of Energy Resources Technology,* 144(2): 022001, Copyright 2021 by ASME

The vertical heights were chosen strategically to correspond to the level of the liquid meniscus of the melted PCM for a pre-determined value of melt-fraction. The heat source for melting is a current carrying Nichrome coil that was mounted inside the cylinder and at the base of the cylinder. The melt front (solid-liquid interface) originates at the base and propagates upwards during the course of the melt-cycle.

2.1.1 Thermocouple Calibration

PFA insulated, fine gage (36 AWG) K-type thermocouple wires (make: Omega) are chosen for fabrication of the temperature sensors. The fine diameter ensures the thermocouple wires occupy least possible volume within the PCM mass. Chromel (+) and Alumel (-) wires of adequate lengths are welded together (at one end) using a thermocouple-wire welder (make: Omega). The thermocouple wires are labelled and the thermocouples are then ready to be calibrated.

The thermocouples were calibrated in a water bath under steady state conditions. The bath temperature was varied from 20 ^{o}C to 40 ^{o}C. An NIST calibrated thermometer (Least Count: 0.1 ^{o}C) was used for measuring the bath temperature. The isothermal water bath setup used in these calibrations experiments is manufactured by Cole Parmer (Model: Polystat). After the calibration step, the measurement uncertainty of the temperature transients recorded by the thermocouples were estimated to lie in the range 0.3% to 0.8%.

Thermocouples were calibrated in the temperature range of 20 to 40 ^{o}C. Steady state temperature values that were recorded by the thermocouples immersed in the water bath were recorded for ~2 minutes at a rate of 0.25 Hz using a digital data acquisition

apparatus (DAQ). The DAQ consisted of NI SCXI 1303 board with the NI SCXI 1000 chassis (National Instruments), for connecting the thermocouple lead wires and for recording the temperature data. The data acquisition was automated using LabView™ software (National Instruments). Calibration was performed for water bath temperature maintained at: 20 ^{o}C, 25 ^{o}C, 30 ^{o}C, 35 ^{o}C, and 40 ^{o}C. The calibration constants were computed in these temperature ranges by fitting a linear function between the values recorded by the NIST thermometer and temperature values measured by each thermocouple – based on the voltage output from each thermocouple (for the five temperatures listed above). Since the NIST thermometer can be used to measure temperature with a precision of 0.1 ^{o}C, while the DAQ platform can record the output from each thermocouple with 16-bit precision: the calibration-step decreases the precision of the temperature measurements but increases their accuracy (closeness to the actual value of the temperature). The calibration curves for the different thermocouples used in this study are provided in Appendix A. The uncertainty in temperature measurement can arise from various sources: (1) uncertainty due to the DAQ precision (u_{DAQ}), (2) statistical uncertainty (u_s), and (3) the precision of the NIST thermometer (u_t). The component of the measurement uncertainty arising from the precision (or truncation errors) of the DAQ (u_{DAQ}) is expressed as:

$$\boldsymbol{u_{DAQ}}\,(\%) = \frac{\frac{\left(\boldsymbol{T_{cal.h} - T_{cal,l}}\right)}{\boldsymbol{2^{N_{bit}} - 1}}}{\boldsymbol{T_{DAQ}}} * \mathbf{100} \qquad (\mathbf{4})$$

where, $T_{cal,h}$ denotes the higher end of the calibration temperature range and $T_{cal,l}$ is the lower end. N_{bit} is corresponds to the DAQ resolution (16-bits). It is a measure of the

number of discrete levels that can represent an analog signal. T_{DAQ} is the temperature measured by the data acquisition system.

$$\boldsymbol{u_t}\,(\%) = \frac{\boldsymbol{L.C.}}{\boldsymbol{T_{therm}}} * \mathbf{100} \qquad (\mathbf{5})$$

L.C. is the least count of the thermometer and T_{therm} is the temperature measured by the thermometer.

$$\boldsymbol{u_s}(\%) = \frac{\boldsymbol{\sigma_s}}{\boldsymbol{T_{DAQ}}} * \mathbf{100} \qquad (\mathbf{6})$$

where, σ_s is the standard deviation of the steady state temperature data. The total uncertainty, u_{total} in a thermocouple reading is the root of the sum of squares of each uncertainty and is given by (7). Thus, we obtain a value of u_{total} corresponding to each temperature—20 ºC, 25 ºC, 30 ºC, 35 ºC, and 40 ºC. The average value for u_{total} from these is the uncertainty in the thermocouple measurement.

$$\boldsymbol{u_{total}}(\%) = \sqrt{\boldsymbol{u_{DAQ}^2 + u_t^2 + u_s^2}} \qquad (\mathbf{7})$$

While reporting the average ambient temperature during a PCM melting experiment, an additional source of statistical uncertainty needs to be accounted for. This is attributed to the spread of the ambient temperature over a range of values throughout the experiment. This additional component of uncertainty, u_{amb}, is quantified by the standard deviation of the ambient temperature data recorded in any experiment.

$$\boldsymbol{u_{amb}}\,(\%) = \frac{\boldsymbol{\sigma_{amb}}}{\boldsymbol{T_{amb,DAQ}}} * \mathbf{100} \qquad (\mathbf{8})$$

Table 7 in Appendix B summarises the uncertainties (in percentage) for different thermocouples used for obtaining the transient temperature data. The total uncertainty in

measurement for any thermocouple lies between 0.3 % and 0.8 %. The steps followed to obtain the total uncertainty (for the thermocouple located at a height corresponding to 30% melt-fraction within the PCM as an example) are also summarised in Appendix B.

2.1.2 Mounting of Thermocouples

The location of the thermocouples along the axis of the cylinders and its outer surface is based on the particular location of the liquid meniscus of the PCM (as it melts progressively) corresponding to chosen and specific values of melt-fraction of the PCM. A series of volume calibration experiments were performed in the measuring cylinder (before performing the PCM experiments) to determine the height corresponding to a particular value of the volume of liquid phase. This was performed by filling the measuring cylinder with a fixed quantity of water and noting the level of the liquid meniscus, as follows. With the heater assembly and the thermocouple positioning apparatus inside the cylinder, water is poured in 5 ml aliquots. The water level rise is recorded until the water reaches the 50 ml mark. Due to the volume occupied by the apparatus inside, the volume level shown by the cylinder is higher than the actual volume of water in it. Fig. 3 shows the filled volume as a function of the actual volume. Using the densities of the solid and liquid PCM phases, the cylinder markings corresponding to the chosen melt-fractions are determined.

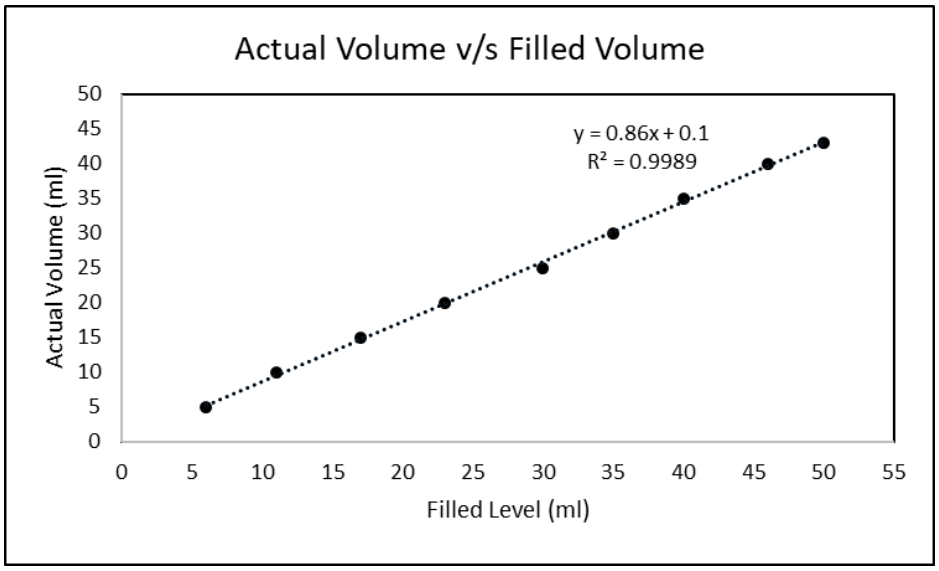

Figure 3. Actual volume versus apparent volume of water in the cyllinder.

The following expressions help us to determine the location of a thermocouple, i.e., for co-location with the corresponding height of the meniscus - for a specific melt-fraction, M (%). In what follows, V (ml) stands for actual volume when the apparent volume measured by the cylinder is V' (ml). Let $V_{L,100}$ (ml) be the actual volume of 100% liquid PCM in the cylinder when the liquid meniscus is at the maximum mark (the cylinder capacity). $V'_{L,100}$ denotes the apparent volume of liquid in the cylinder. For experiments in this study, $V'_{L,100}$ is equal to 50 ml. The actual volume of the PCM upon solidification is denoted by $V_{S,0}$ and is given by (9).

$$\boldsymbol{V_{S,0} = \frac{\rho_L}{\rho_S} * V_{L,100}} \qquad (\mathbf{9})$$

The apparent volume of the PCM is given by the linear relationship from Fig. 3. For a generalized expression, let the linear relationship between apparent volume and actual volume be given by (10).

$$\boldsymbol{V = C_1 V' + C_2} \quad (\mathbf{10})$$

The volume of liquid PCM in the cylinder (for melt-fraction, *M*) is denoted by $V_{L,M}$ and is given by (11). In these calculations the melt-fraction (*M*) is expressed as a percentage value. In (11), $V'_{L,M}$ is the corresponding milliliter level of the solid-liquid interface measured by the graduated cylinder.

$$\boldsymbol{V_{L,M} = C_1 V'_{L,M} + C_2} \quad (\mathbf{11})$$

Hence, the actual liquid volume, $V_{L,M}$ is given by (12).

$$\boldsymbol{V_{L,M} = \frac{M}{100} * \frac{\rho_S}{\rho_L} * V_{S,0}} \quad (\mathbf{12})$$

Combining (9), (11) and (12) to compute $V'_{L,M}$ (the level of the liquid-solid interface corresponding to a melt-fraction *M*) is the final step. The obtained $V'_{L,M}$ (ml) provides level of the thermocouple along the axis of the cylinder corresponding to a melt-fraction, *M*. Thus, a correlation is derived using this method in order to determine the location of a thermocouple as a function of a selected value of melt-fraction.

Interestingly, there exists a maximum value of melt-fraction such that the thermocouple at that point remains inside the PCM mass throughout the experiment. This occurs due to PCM volume shrinkage. Upon solidification of the PCM, the thermocouples mounted at locations corresponding to higher values of melt-fraction (which are initially submerged in the liquid PCM) are then exposed to air (instead of being submerged in the solidified mass of PCM) since the air-PCM interface recedes upon complete solidification of the PCM. In this experiment, thermocouples mounted at locations corresponding to melt-fraction exceeding 95% - therefore - would not be immersed in the PCM during the entirety of the experiments. Hence, at the beginning of the melt-cycle these thermocouples

would be exposed to air (and will record the temperature of the surrounding air). However, towards the final stages of the melt cycle (when the melt-fraction exceeds 95%), these thermocouples will be submerged in the liquid PCM and would record the temperature of the liquid phase of the PCM.

2.1.3 PCM Melting Experiments

Thermocycling experiments were conducted in this study to obtain a dataset consisting of temperature transients and the corresponding values of melt-fraction. PureTemp 29™ is chosen as the candidate PCM in these experiments. The salient properties of Pure Temp29^{TM} are listed in Table 1 [37]. The data from these experiments were used for training an ANN model. The goals of these experiments and numerical simulations were focused on deploying the ANN model for real-time prediction of the time required to reach a target value of melt-fraction (e.g., 85%). The errors in the predictions (compared to experimental data) were obtained from this study with the goal of identifying the ANN model that yields the best performance.

Solid sample of PCM was heated in a graduated measuring cylinder (with total volume of 50 ml) and with a least count of 1 ml. The experiments were performed until the PCM was melted completely. Broadly, the apparatus consists of four components: (i) the graduated measuring cylinder; (ii) K-type thermocouples; (iii) heater coil; and (iv) Data acquisition system.

The heater assembly is composed of a Nichrome wire (coil) connected to a DC power supply. The coil is placed at the bottom of the cylinder for melting the PCM for a

fixed value of input power. The ends of the coil are connected to a DC supply by means of insulted connecting wires. Such a configuration means that when the liquid meniscus is at 0 ml marking (i.e., there is no melting), the PCM is at a 0% melt-fraction. Whereas, when the liquid meniscus is at the 50 ml marking, the PCM is at 100% melt-fraction. The thermocouples are placed at particular locations (within the volume of the PCM) and along the axis of the cylinder corresponding to 30%, 60%, 85%, 90%, 95%, and 99% melt-fraction. On the outer surface of the measuring cylinder, the surface-mounted thermocouples are located at heights corresponding to 30%, 60%, 90% and 99% melt-fraction. In addition to these sets, another thermocouple is located at a distance of 1 cm above the 50 ml mark on the outside surface of the measuring cylinder, i.e., at a distance of 1 cm above the height of the meniscus corresponding to 100% melt-fraction. Thermal paste (Omegabond^{TM}) is used as a glue to mount the thermocouples on the outside surface of the measuring cylinder. The thermocouples are calibrated in the temperature range of 20 ^{o}C to 40 ^{o}C. The calibration step involves the measurement of the steady state temperature of each thermocouple when placed in a water bath and the temperature measurements were recorded by an automated digital data acquisition system for a period of 2 minutes. The calibration was performed for fixed temperature values (of the water bath) corresponding to 20 °C, 25 °C, 30 °C, 35 °C, and 40 °C. The calibrations were performed using a NIST calibrated mercury thermometer with a least count of 0.1 °C . The resultant calibration error (instrument/ bias error and statistical error) is estimated to be less than ± 0.1°C with a 68% statistical confidence (i.e., within one standard deviation of the average value).

Table 1 Salient Properties of PureTemp29™ [39]

Property	Value
Enthalpy of Phase Change	202 J/g
Heat Capacity of Solid	1.77 J/g ^{o}C
Heat Capacity of Liquid	1.94 J/g ^{o}C
Density of Solid	0.94 g/ml
Density of Liquid	0.85 g/ml
Conductivity of liquid	0.15 W/m ^{o}C
Conductivity of solid	0.25 W/m ^{o}C

A digital data acquisition system (NI SCXI 1303 board with the NI SCXI 1000 chassis, from National Instruments Inc.) was used for recording the transient temperature data from the thermocouples. The data acquisition process was automated using Labview^{TM} software (from National Instruments Inc.). The photograph of the experimental setup is shown in Fig. 4. Figure 5 schematically depicts the different components of the experimental apparatus. A plastic tube was inserted into the measuring cylinder (prior to filling it with PCM). The plastic tube was used for mounting the thermocouples and for the purpose of placing the beaded ends of the thermocouples at specific locations precisely along the vertical direction. The lower end of the plastic tube was sealed to prevent PCM from seeping in, and the thermocouple wires emerged out of the upper end of the plastic tube. The cylinder is filled with liquid PCM up to the 50 ml mark and allowed to solidify under ambient conditions. Digital images of the whole volume of PCM within the

measuring cylinder were captured every 60 s during the melting experiments in order to monitor the rise of the liquid-solid interface along the vertical direction. An infra-red (I.R.) camera was used to capture I.R. images intermittently at specific intervals of time. The I.R. images were used to monitor the temperature distribution and ascertain temperature uniformity within different parts of the experimental apparatus. Representative I.R. images are shown in Fig. 6. Appendix G includes the I.R. images generated during the course of experiments done in this study. Each image corresponds to a specific time of its capture after the heating process has commenced (i.e., after the heater is switched on). The time of capture is stored along with the image.

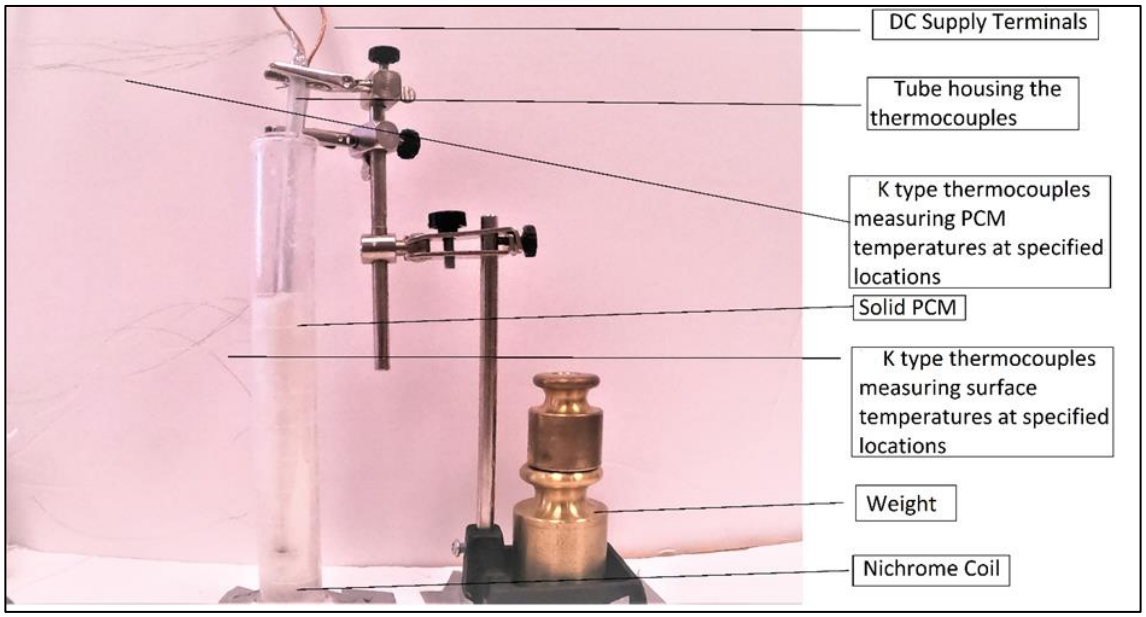

Figure 4 Photograph of the experimental apparatus used in the study.

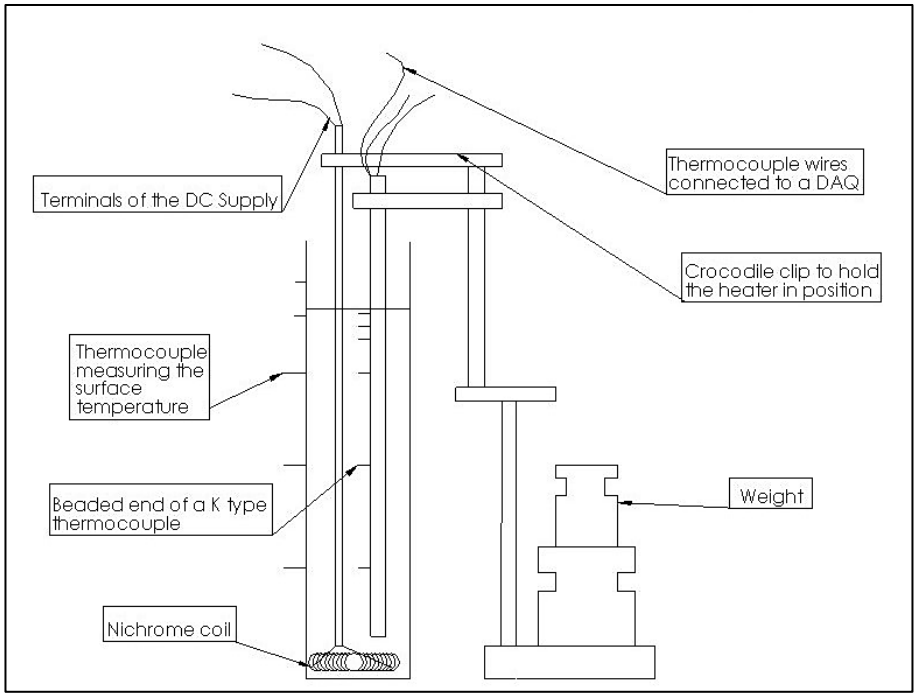

Figure 5 Schematic of the experimental apparatus used in this study.

Using the apparatus, melting experiments were performed by setting the heater voltage at a constant value. The thermocouple and the visual data (digital images and IR images) were recorded until complete melting of the PCM was achieved. Experiments were performed for three sets of heater input voltages—2.8V (1.6W), 2.6V (1.4 W), and 2.3V(1.08W). Each experiment was conducted twice to verify repeatability of the experimental data. The transient temperature data recorded by the thermocouples is plotted using a line graph.. Figure 7 shows the transient temperature profile recorded by thermocouples that were mounted within the mass of PCM ("transient PCM-temperature data"). Fig. 8 shows the transient temperature profile recorded by thermocouples mounted on the surface of the measuring cylinder ("transient surface-temperature data"). In these plots, the abscissa denotes the elapsed time in seconds [s].

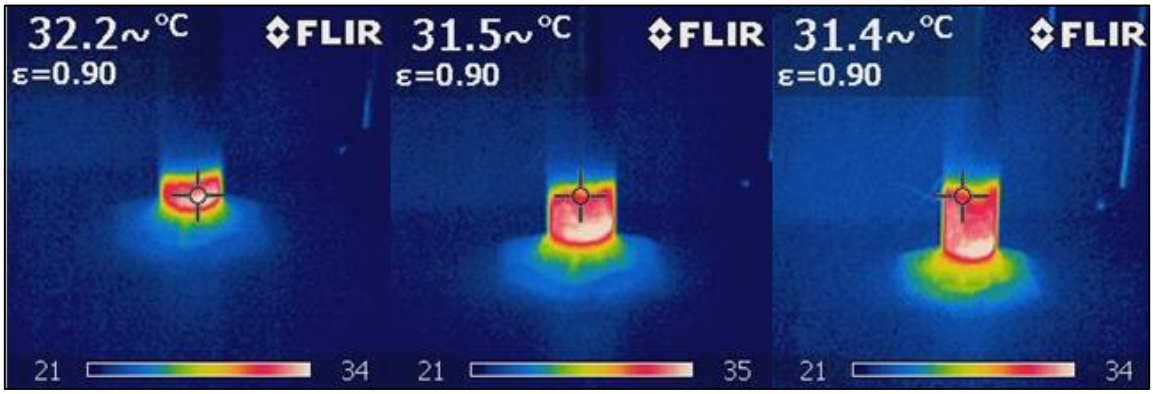

Figure 6 Images of the PCM undergoing melting in the cylinder for heater input power of 1.6 W (2.8 V input condition).

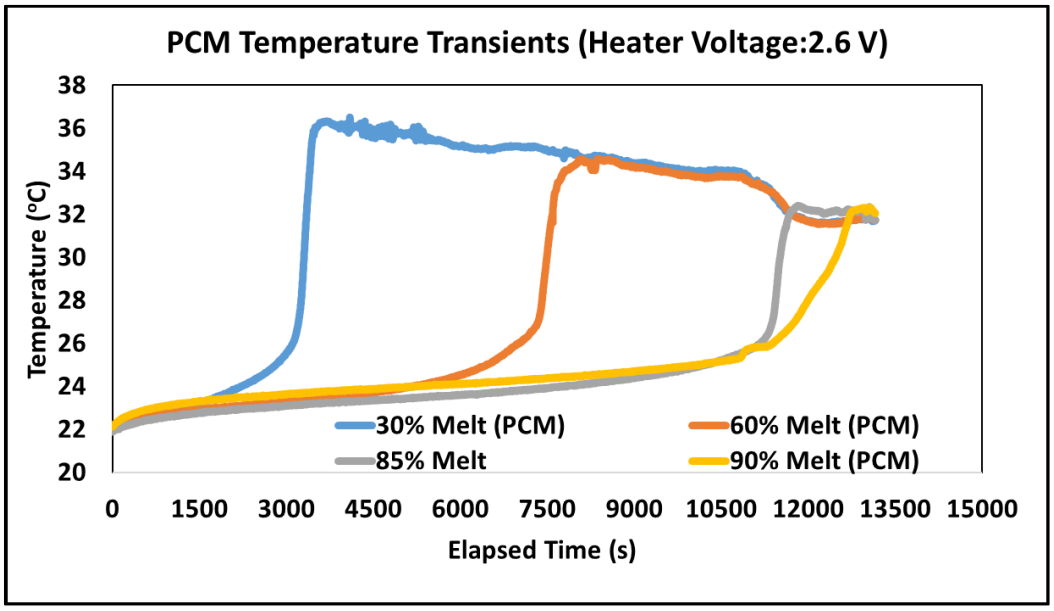

Figure 7 Temperature transients of the PCM recorded by the thermocouples mounted within the experimental apparatus for a heater input voltage of 2.6 V (1.4 W power input).

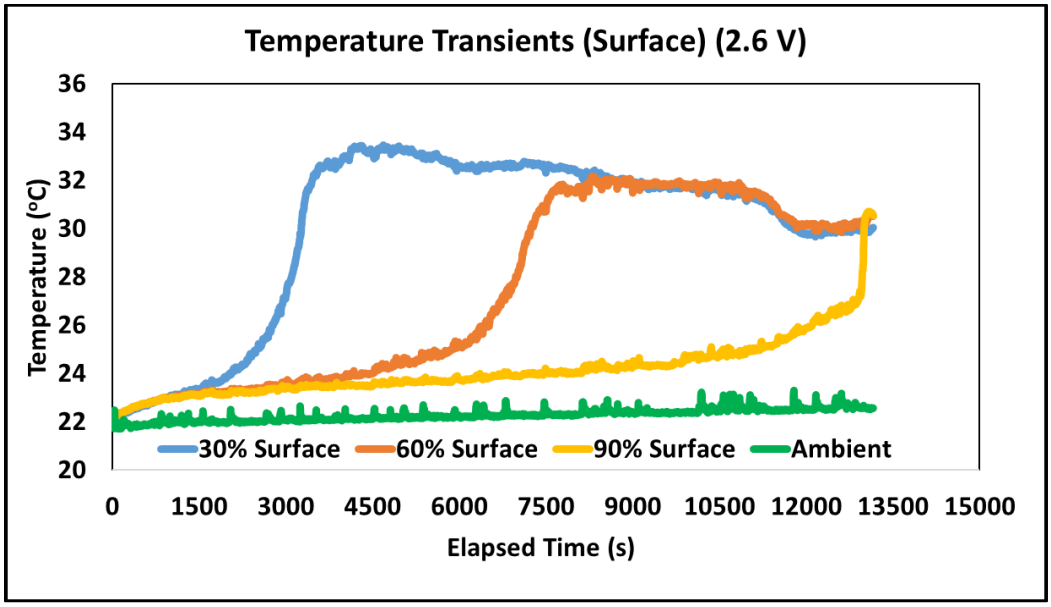

Figure 8. Temperature transients recorded by the thermocouples measuring the cylinder surface temperatures for a heater input voltage of 2.6 V (1.4 W power input).

2.2 Data Preparation for ANN Training and Validation

The goal of this study was to predict in real-time (i.e., at any instant during the melting process) — the time remaining to attain the target melt-fraction, for instance an 85% melt-fraction. In deep learning terms, for this case, the "time to reach 85% melt-fraction" is the label. This label is obtained by subtracting the time recorded corresponding to each temperature measurement (consisting of the following set: [T_{30}, T_{60}, T_{85}, T_{90}, T_{95}, T_{99}, T'_{30}, T'_{60}, T'_{90}, T'_{99}, $T_{ambient}$]) from the time when melt fraction of 85% is attained. The target value of 85% melt-fraction is achieved when the melt front hits the particular thermocouple inside the PCM mass (indicated by the sudden rise in temperature recorded by that particular thermocouple). This point is indicated by the temperature profile of that thermocouple (Fig. 7). The temperature curve begins to plateau after a sharp increase. The

time stamp on this point serves our purpose for generating the labels. Thus, in the example, the label is obtained from the T_{85} temperature transient.

However, if the label is in the form of dimensional time in seconds, this technique would not be scalable as the time for melting is a function of the heater voltage. With a heater voltage of 2.3 V, the PCM volume takes about 4.5 hours to melt completely. In contrast, with a 2.8 V heater voltage, the PCM melts in about 3 hours. Hence, a nondimensional quantity, referred to as 'reduced time', is formulated. Nondimensionalizing the time parameter allows us to train the ANN using one experimental dataset and predict for another case. This reduced time, τ, is obtained by taking the ratio of the elapsed time to the time when the target value (e.g., 85% melt-fraction) is achieved. It follows that the nondimensional form of the label is then the complementary value of τ (i.e., obtained by subtracting τ from unity and is denoted by τ').

Let t denote the time elapsed from the initiation of the melting process for which corresponding temperature measurements — [T_{30}, T_{60}, T_{85}, T_{90}, T_{95}, T_{99}, T'_{30}, T'_{60}, T'_{90}, T'_{99}, $T_{ambient}$] are captured by the DAQ. The variable t'_m is the time remaining to attain a specific melt fraction (m) at any time t. The total time taken by the PCM to reach the melt-fraction of m (expressed as a percentage) is denoted by t_m. For all t during any experiment performed in this study, the relationship between t'_m and t_m can be expressed as follows:

$$\boldsymbol{t'_m = t_m - t} \qquad (\mathbf{13})$$

The non-dimensional elapsed time corresponding to t is denoted by τ_m and is expressed as:

$$\boldsymbol{\tau_m = \frac{t}{t_m}} \qquad (\mathbf{14})$$

Finally, the label chosen as the output parameter of the ANN is denoted by τ'_m and can be expressed as:

$$\boldsymbol{\tau'_m = 1 - \tau_m} \quad (\mathbf{15})$$

Thus, we have a value of τ'_m corresponding to each transient temperature data point. Further, each temperature data point is composed of a set of 11 temperatures—[T_{30}, T_{60}, T_{85}, T_{90}, T_{95}, T_{99}, T'_{30}, T'_{60}, T'_{90}, T'_{99}, $T_{ambient}$]. Figure 9 depicts the plot of PCM temperatures as a function of nondimensional time (τ_{85}) and was obtained after implementing the aforementioned steps. In this study, four ANN system frameworks are explored. These frameworks differ from one another in terms of the inputs and the target melt-fractions. The topology (number of nodes, layers) of the neural network is the same in all the frameworks. Table 2 summarizes these frameworks.

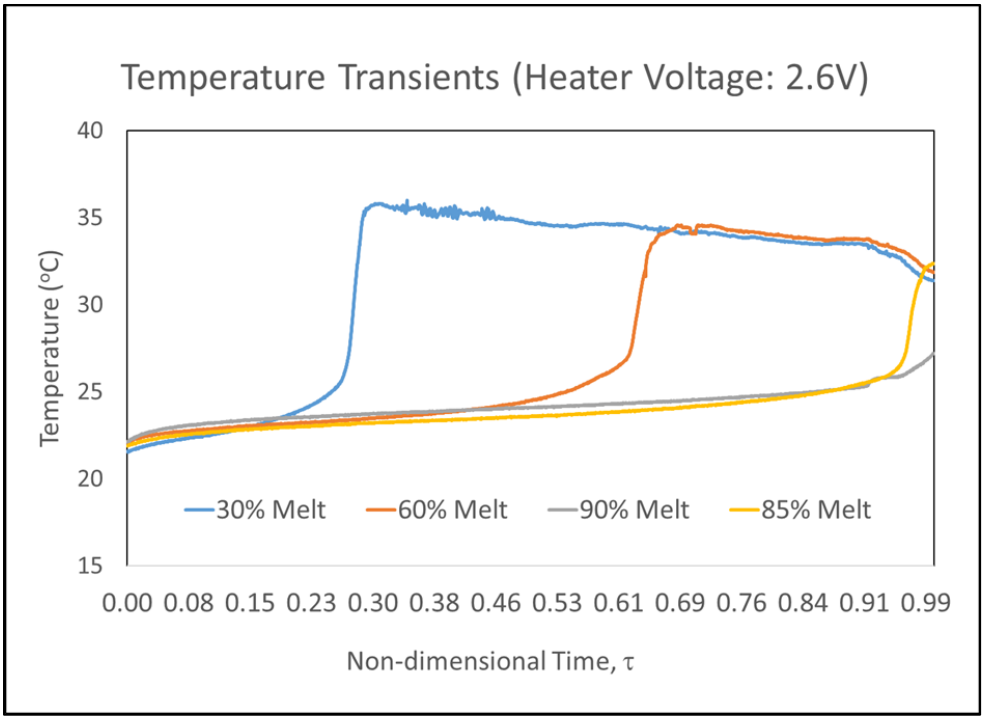

Figure 9. Temperature transients from the three thermocouples mounted within the experimental apparatus for a heater input voltage of 2.6 V, plotted as a function of the non-dimensional time (τ_{85}).

Table 2 Summary of datasets utilized for training and validating the ANN models

Serial No.	Preselected Melt-fraction (%)	ANN input (Temperatures in °C)	ANN output
1	90	T_{30}, T_{60}, T_{85}	τ'_{90}
2	90	T'_{30}, T'_{60}, T'_{90}	τ'_{90}
3	85	T_{30}, T_{60}, T_{90}	τ'_{85}
4	85	T'_{30}, T'_{60}, T'_{90}	τ'_{85}

The MLP model (i.e., the artificial neural network/ ANN model) is trained using τ'_m as the label and the three temperature inputs (recorded by the experiment for a particular power input). The training process is based on the well-known back-propagation algorithm which modifies the weights and biases of a node as it iterates through the dataset. The training process is stopped by using the 'early stopping' approach. In other words, when the MSE does not improve substantially upon further iterations, the training process is halted. The neural network in this study is composed of three hidden layers and each layer has 512 nodes. The Rectified Linear Unit (ReLU) activation function is used in the network nodes. The cost function for training purposes is the Mean Squared Error (MSE). The mean squared error is computed over the complete training dataset, i.e., over all the temperature measurements in the training dataset. In other words, the squared sum error (SSE) is computed for each point. At the end of each iteration in the backpropagation algorithm, the MSE is obtained by computing the average of the squared sum errors corresponding to every data point. ADAM optimizer is deployed as the gradient descent algorithm. The predictions are generated for all the six combinations of training/ prediction by utilizing the three datasets. A Multilayer Perceptron (MLP) Network is devised with input nodes. Figure 10 shows the topology of the neural network for the framework corresponding to serial no. 3 in Table 2, (i.e., the PCM temperatures, marked as: T_{30}, T_{60} and T_{90}; which constitute the three inputs and the output of the ANN – which is τ'_{85}).

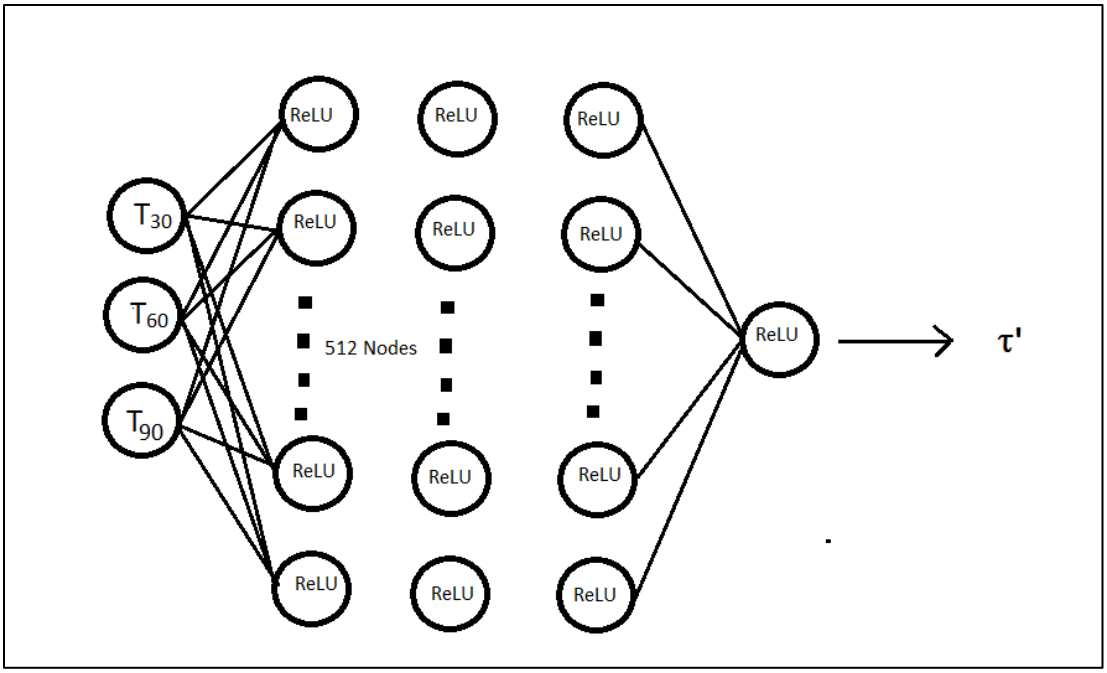

Figure 10. Topology of the MLP network predicting τ'_{85} (as a function of T_{30}, T_{60}, and T_{90}).

CHAPTER III

RESULTS AND DISCUSSION*

3.1 Introduction

This chapter consists of three sections:

1. Prediction of time to reach 90% melt-fraction using transient PCM temperature data (located at meniscus levels corresponding to 30%, 60%, and 85% melt-fraction) for training the ANN model.
2. Prediction of time to reach 90% melt-fraction from the transient surface-temperatures data (located at meniscus levels corresponding to 30%, 60%, and 90% melt-fraction) for training the ANN model.
3. Comparison of predicted values for the time to reach 85% melt-fraction by the ANN model using two different approaches: (a) transient PCM-temperature data; and (b) transient surface-temperature data. The temperature data are acquired from thermocouples located at meniscus levels corresponding to 30%, 60%, and 90% melt-fraction.

---

*Part of the data reported in this chapter is reprinted with permission from "Leveraging Machine Learning (Artificial Neural Networks) for Enhancing Performance and Reliability of Thermal Energy Storage Platforms Utilizing Phase Change Materials" by Aditya Chuttar, Ashok Thyagarajan, and Debjyoti Banerjee, 2021. *Journal of Energy Resources Technology,* 144(2): 022001, Copyright 2021 by ASME

Three datasets corresponding to a different voltage and power input condition for the heater are considered in this study: 2.3V, 2.6V, and 2.8V. The experiments performed for 2.3V input to the heater corresponds to a current of 0.47A and a power input of 1.08 W. When the heater input voltage is 2.6V, the heater draws a current 0.54A and a power input of 1.4W. For 2.8V input, the current and power inputs are 0.58A and 1.6W, respectively. It is to be noted that a total of 6 PCM melting experiments were performed—two for each heater power input (2.3 V, 2.6 V, 2.8 V). Experiments were conducted twice to ensure that they are repeatable. However, for a particular heater voltage, the output of *one* experiment is utilised for data processing and subsequently, training the neural network. For instance, from the two available datasets for 2.6 V (1.4 W) heater input, one is used for training the ANN model. All the results summarised in the sections that follow are computed from dataset constituting the experimental output from one experiment corresponding to each of the three heater input voltages.

The time taken to reach 100%, 90%, and 85% melt for the three datasets is depicted by means of a bar chart in Fig. 11. The difference between the time to reach a given melt-fraction among the data sets shows wide variability for the chosen power input conditions. For instance, the time to reach 100% melt for 2.3V set and 2.6V set is 15,658 s and 13,157 s, respectively (a difference of 2,500 s). Whereas time to reach 90% melt for 2.3 and 2.6V experiments is 13,670 s and 12,729 s respectively (a difference of 940 s). Similar trend can be observed between 2.3V and 2.8V sets as well. This trend can be attributed to increasing heat losses to the ambient from the lateral walls of the cylinder as the solid-liquid PCM interface moves upwards. The ambient temperature plays a key role in

determining the heat loss due to heat loss by free convection from warmer surface of the measuring cylinder (than the ambient). The average ambient temperatures during the experiments are listed in Table 3. The minimum and maximum ambient temperatures are also shown. All the temperatures are reported at 68% confidence level.

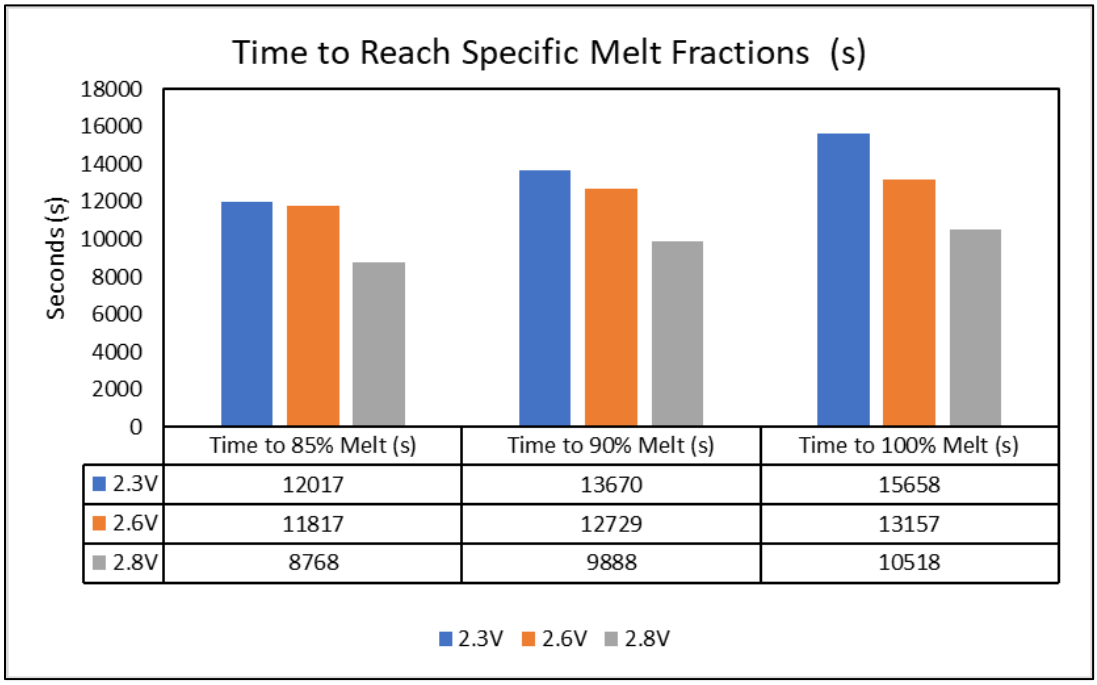

Figure 11. Time to reach specific melt-fraction as a function of heater voltage.

Table 3 Ambient temperatures during PCM melting experiments

Experiment Heater Voltage (V)	**Min. Ambient Temperature (º C)**	**Max. Ambient Temperature (º C)**	**Avg. Ambient Temperature (º C)**
2.3V	21.7± 0.09	22.9± 0.09	22.1± 0.1
2.6V	21.0 ± 0.08	22.6± 0.09	21.6 ± 0.1
2.8V	21.0 ± 0.08	21.8 ± 0.09	21.2 ± 0.1

The absolute value of the time required to completely melt the PCM for a given heater power is highly sensitive to minor variations in the ambient temperature. For the same heater voltage, the time to reach a 100% melt-fraction can thus vary for different instances of the experiment. The repeatability of the experiments can be established by plotting temperature transients recorded by a thermocouple, e.g., T_{30} against non-dimensional time (where the total time spans from 0 to 100% melt). As an example, Figs. 12-14 shows the repeatability of the 2.8V experiment . The initial temperature of the solid PCM at the beginning of the two instances of the 2.8V experiment are different (due to different ambient conditions) causing the deviations observed in Figs. 11-13. Between Experiment-1 and Experiment-2, the PCM temperatures are different at $\tau_{100} = 0$ (at the beginning of the experiment). The graphs showing the repeatability of 2.3V and 2.6V experiments have been included in Appendix C.

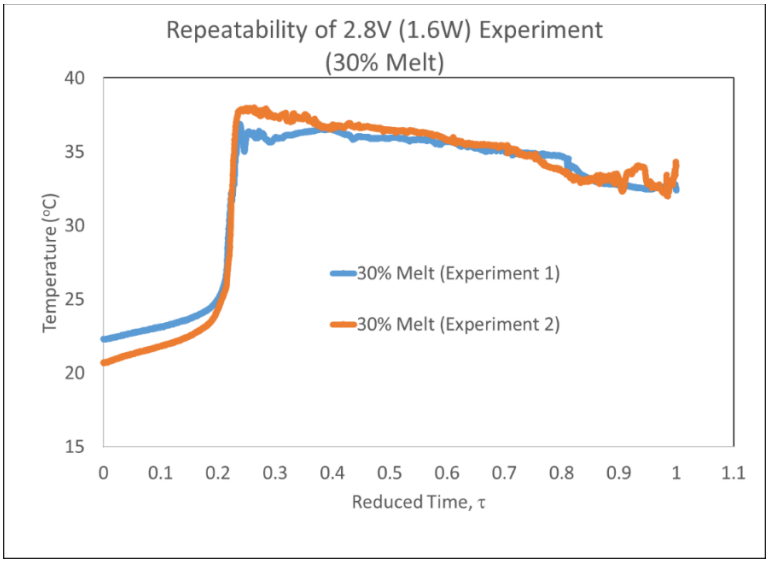

Figure 12. Comparison of temperature profiles in two different experiments for verifying the repeatability of the experiments: for the thermocouples mounted at the location corresponding to the height of the liquid meniscus for PCM melt-fraction of 30% and for heater input power of 1.6 W (2.8 V input).

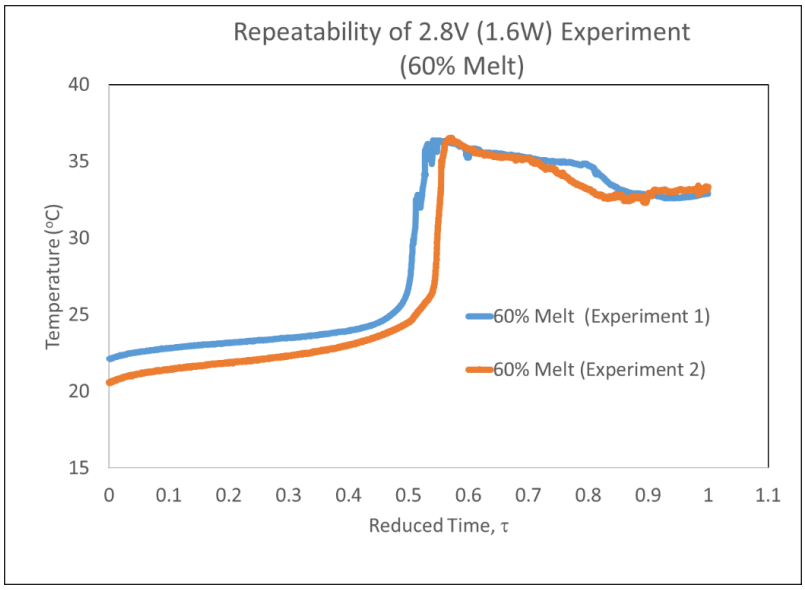

Figure 13. Comparison of temperature profiles in two different experiments for verifying the repeatability of the experiments: for the thermocouples mounted at the location corresponding to the height of the liquid meniscus for PCM melt-fraction of 60% and for heater input power of 1.6 W (2.8 V input).

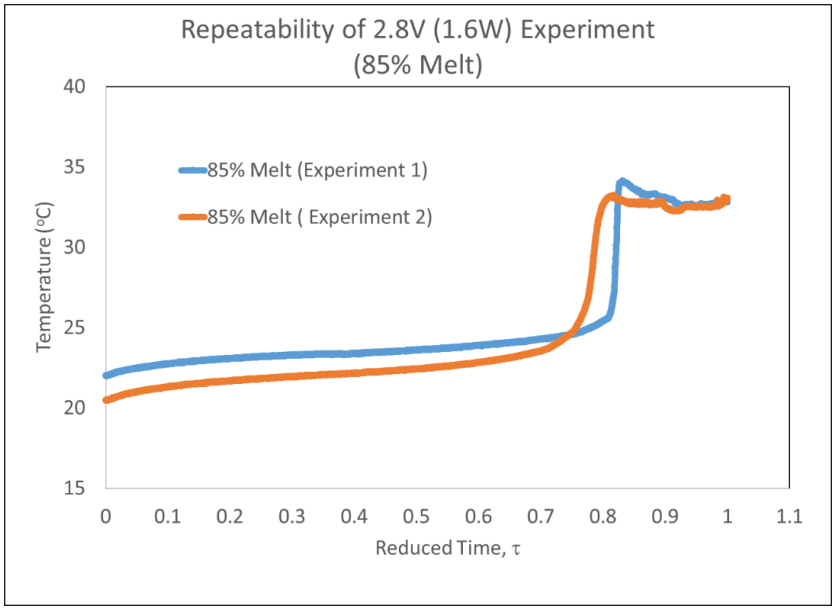

Figure 14. Comparison of temperature profiles in two different experiments for verifying the repeatability of the experiments: for the thermocouples mounted at the location corresponding to the height of the liquid meniscus for PCM melt-fraction of 85% and for heater input power of 1.6 W (2.8 V input).

3.2 Prediction of Time to Reach 90% Melt-Fraction (Using PCM Temperature Data at 30%, 60%, and 85% Melt-fractions)

This section presents the results of the ANN predictions. The τ'_{90} parameter is the output of the ANN. The input to the ANN is constituted of the PCM temperatures at 30%, 60%, and 85% melt-fraction levels. The three experimental data sets generated by varying the heater voltage (2.3 V, 2.6 V, and 2.8 V) are used in different sets of combinations for training the ANN and validating the efficacy of each prediction. For instance, an ANN trained on the 2.6 V data set is deployed to make predictions on the 2.3 V set and the 2.8 V set. For a graphical presentation, the predictions of the ANN are depicted on a scatter plot for any combination of the training and prediction datasets. The solid red line ($y = x$ curve) serves as a reference for deviations of the predictions from the actual ("true" experimental) values.

3.2.1 Training Set: 2.6 V, Prediction Set: 2.8V

Using 2.6 V data obtained from the experiments as the training data, the predictions for the 2.8 V dataset are shown in Fig. 15. The vertical dotted lines in Fig. 15 (and similar figures that follow) denote the points when the melt front hits the particular thermocouple, i.e., when the melt front reaches the specific melt-fraction (in this case, 30%, 60%, and 85%). The τ'_{90} value at that point is identified and a dotted line intersecting the x-axis at that point is plotted. On the non-dimensional scatter plot (e.g. Fig. 15), the green dotted line represents the point when the melt front reaches the respective thermocouple for the training set whereas the blue dotted line denotes the same for the

prediction set. Fig. 15 is dimensionalized by multiplying τ'_{90} values by the time taken to reach 90% melt corresponding to the prediction set. In this case (training Set: 2.6 V, prediction Set: 2.8V), the factor of multiplication is 9,888 s (the time taken by the PCM to reach 90% melt when the heater voltage is 2.8 V). Fig. 16 shows the resultant scatter plot.

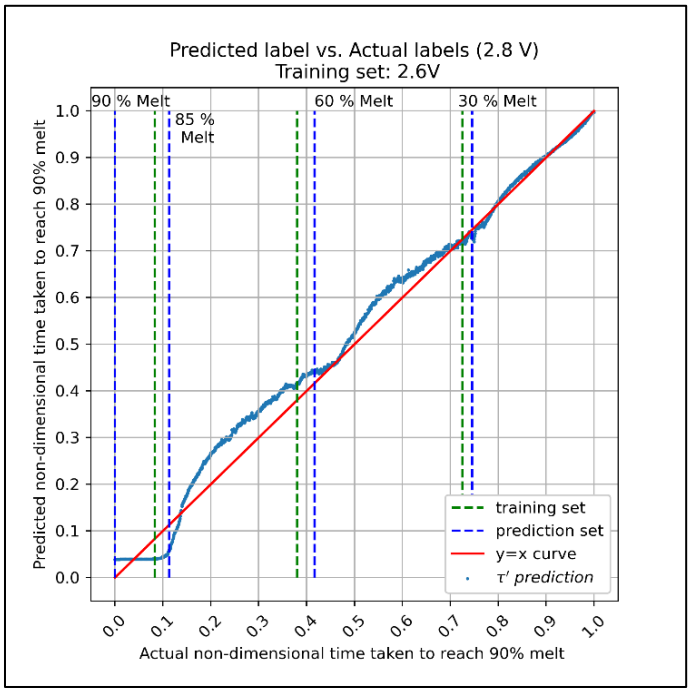

Figure 15. Scatter plot comparing the ANN predictions with experimental data (the actual values for τ') for test data set of 2.8 V (and training data set of 2.6 V).

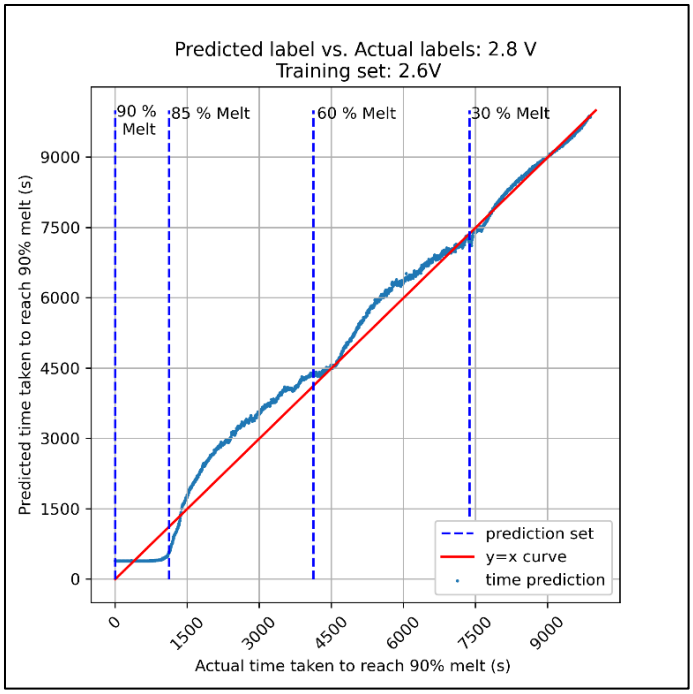

Figure 16. Scatter plot comparing the ANN predictions with experimental data for test data set of 2.8 V (and training data set of 2.6 V).

In order to ascertain the source of the deviations, an *error* term is formulated. as the difference between the predicted value and the actual value of time (in seconds). Fig. 17 depicts a line graph showing the variation of the error throughout the melting cycle. It is evident from the plot that the predictions from the ANN model (time to reach 90% melt-fraction at any instant) match the actual values with considerable accuracy throughout the cycle. In fact, for a training/prediction combination of 2.6 V/ 2.8 V, the average absolute error in the final 1800 s (0.5 hours) before reaching 90% melt-fraction is about 4 minutes (230 s) which is a minute fraction of the total cycle time. A low error is desired particularly at the final stages, i.e. when the PCM is about to reach a melt fraction of 90% so that the melting cycle can be halted in time in a real life application of this method.

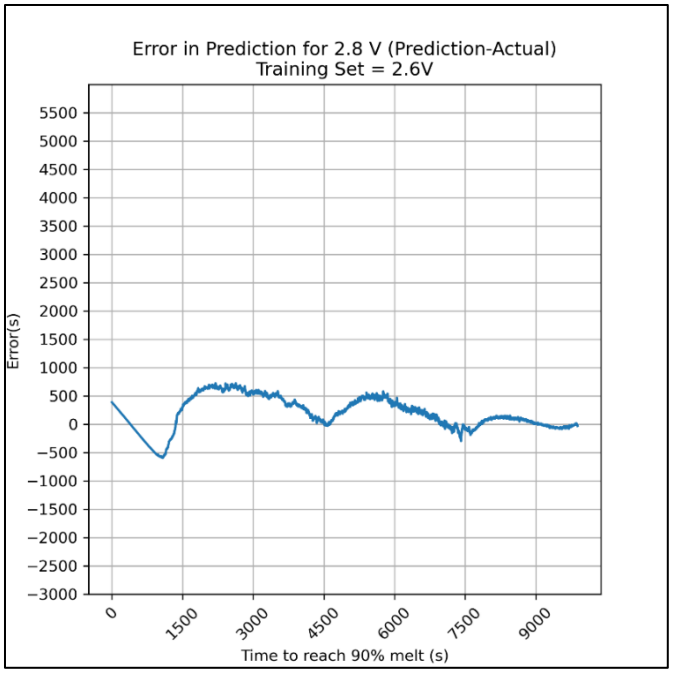

Figure 17 Error in predictions by the ANN model for 2.8 V dataset (training data set of 2.6 V)

3.2.2 Training Set: 2.8 V, Prediction Set: 2.6 V

The ANN is now trained using the 2.8 V data set and is deployed to obtain predictions for the 2.6 V dataset. The results are depicted in Figs. 18-19. In this case, the average error in predictions is computed to be 309 s during the final half an hour before the 90% melt-fraction is reached. Upon comparing Figs. 16 and 18, we see that the scatter plot has shifted below the y=x curve in the case of training with 2.8 V dataset and predicting for the 2.6 V dataset. In Fig. 18 (when the training and prediction sets were 2.6 V and 2.8 V, respectively), the scatter plot lies above the $y = x$ curve.

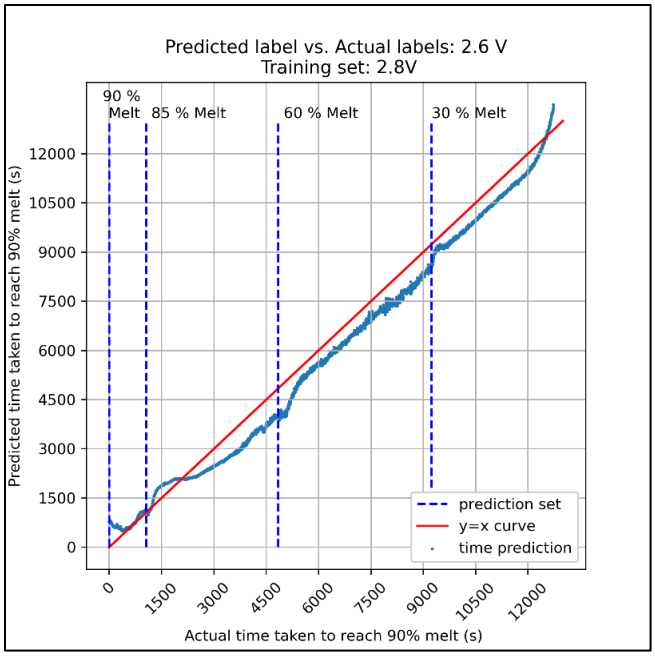

Figure 18. Scatter plot comparing the ANN predictions with experimental data (the actual values for τ') for test data set of 2.6 V (and training data set of 2.8 V).

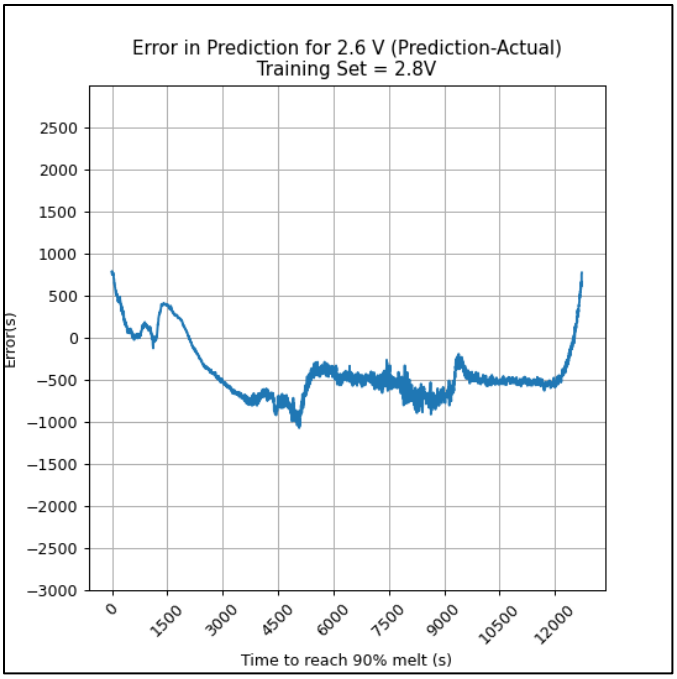

Figure 19. Error in predictions by the ANN model for 2.6 V dataset (training data set of 2.8 V).

In the two sets of predicted values considered so far (corresponding to the training data sets of 2.6 V and 2.8V), the scatter plots tend to flatten in the region between 85% and 90% melt-fraction (between the dotted lines at 85% and 90% melt-fraction in Fig. 16 and 18). It is to be noted that the thermocouple at 90% melt-fraction is outside this range (30–85%). Hence, the ANN is not able to discern the distinction between points when the melt-fraction is in excess of 85% —i.e., between melt-fraction values of say, 87% and 90%—as sharply. In other words, the temperatures recorded by the three thermocouples (at 30%, 60%, and 85% melt-fraction) at an instant when the melt-fraction is 87% are not too distinct from those at an instant when the melt-fraction is 90%. The reason behind this discrepancy is that all the three thermocouples are immersed in the liquid pool by this point in time during the execution of the experiments. This translates into similar predictions at time instants after the melt front has passed the thermocouple located at the 85% melt-fraction. As a result, we obtain a flattened scatter plot toward the end of the melt cycle.

3.2.3 Training Set:2.3 V; Prediction Set: 2.6 V

The ANN model trained using 2.3V dataset (for the transient PCM temperature data) is used for predicting the value of time remaining to reach 90% melt fraction (for the 2.6 V input condition). The resulting scatter plot is shown in Fig. 20 and Fig. 21. As discussed previously, the scatter plot tends to flatten towards the end (at melt faction greater than 85%). The average absolute error during the final half an hour is 374 s.

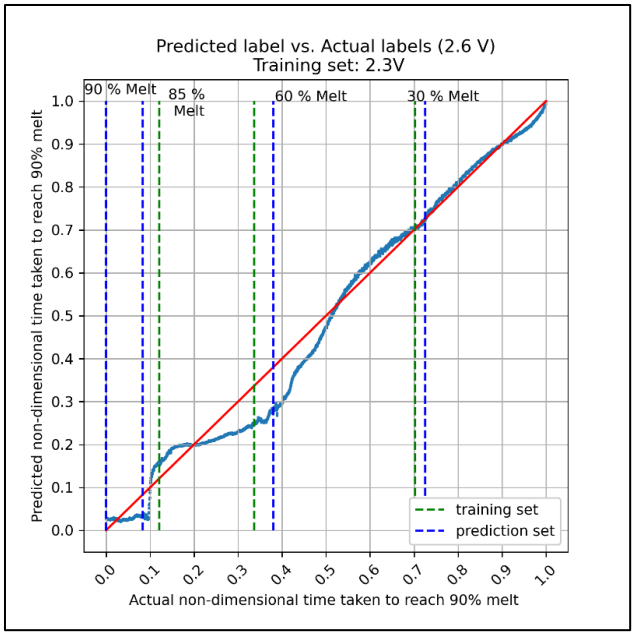

Figure 20. Scatter plot comparing the ANN predictions with experimental data (the actual values for τ') for test data set of 2.6 V (and training data set of 2.3 V).

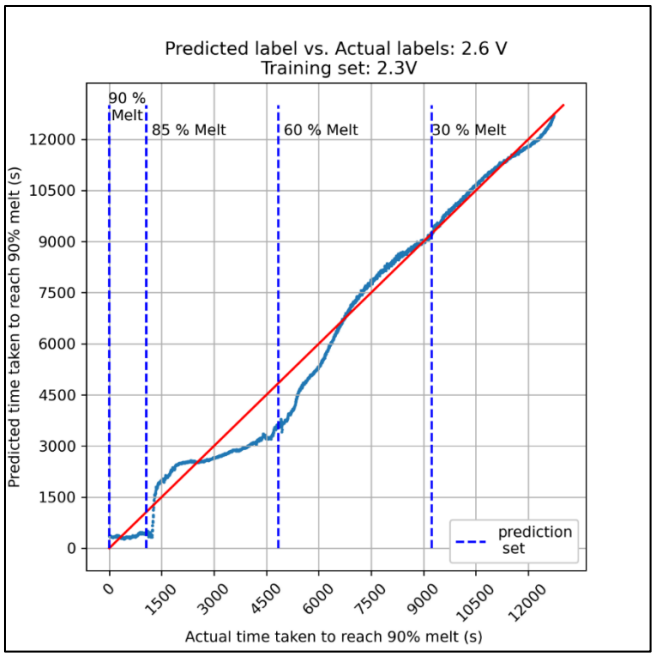

Figure 21. Scatter plot comparing the ANN predictions with experimental data for test data set of 2.6 V (and training data set of 2.3 V).

Considering the average absolute error in the last half an hour before 90% melt-fraction is achieved (as the metric quantifying the efficacy of the technique presented in this study), Table 4 summarizes this quantity for all the 6 training/prediction combinations. The errors are less than 5% for the predicted values of the time remaining to reach 90% melt-fraction. These errors are of the order of 10 minutes.

Table 4 Average absolute error in predictions during final 1800 s prior to attaining a melt-fraction fraction of 90%

Training / Prediction	2.3 V [1.08 W]	2.6 V [1.4 W]	2.7 V [1.6 W]
2.3 V [1.08 W]		670 s	680 s
2.6 V [1.4 W]	374 s		315 s
2.8 V [1.6 W]	215 s	230 s	

In this section, we demonstrated a representative procedure to achieve real time prediction of the time remaining to reach a preselected melt-fraction as a PCM melts in a LHTESS platform. The aim is to use this technique to provide real time predictions so that the melting cycle can be halted in time to have a residual mass of PCM in a solid state.

3.3 Prediction of Time to Reach 90% Melt-fraction using Cylinder Surface Temperatures at 30%, 60%, and 90% melt-fraction

The motivation to explore the efficacy of utilizing surface temperatures arises from the packaging aspects in passive thermal management of electronics. PCMs are considered to be attractive candidates for augmenting the efficacy of passive cooling platforms that

are deployed at the board/subcomponent level during transient operation of electronics devices. When deployed in a heat sink that leverages PCM based passive thermal management systems for cooling of electronic chips and packages, this maverick approach (using the second method) affords cheaper costs, better sustainability, higher reliability and resilience.

This section explores the effectiveness of utilizing the transient surface-temperature data for training the ANN model with the goal of predicting the values of the parameter: τ'_{90} (non-dimensional time to remaining to reach 90% melt-fraction). As in the previous section, scatter plots for different training/prediction combinations are utilized to ascertain the efficacy of this strategy. It can be noted that the labels (τ'_{90}) for training the ANN are generated from the thermocouple at 90% melt level inside the PCM mass. On the other hand, the input to the ANN model consists of the transient *surface-temperature* data recorded by the thermocouple located at the 90% melt-fraction level (along with that of the thermocouples located at melt-fractions corresponding to 30% and 60%). It may be noted that there is a phase lag between the temperature response for thermocouple pairs located at the same level, i.e., for PCM-temperature and surface-temperature for a given value of melt-fraction (e.g., 30%, 60% or 90%).

Fig. 22 shows the results for the 2.6 V/ 2.8 V training/ prediction combination. We see that the predictions are less smooth than those with PCM temperatures. The surface temperatures are subject to higher noise than PCM temperatures due to transient effects of ambient conditions. This feature is evident in Fig. 23 (which shows the results for a training/prediction combination of 2.3 V/ 2.8 V) as well. Table 5 summarizes the average

absolute errors in prediction in the final 1800 s (prior to attaining a melt-fraction of 90%) for all combinations of training and prediction datasets.. The graphs showing the remaining training/prediction combinations have been included in Appendix E.

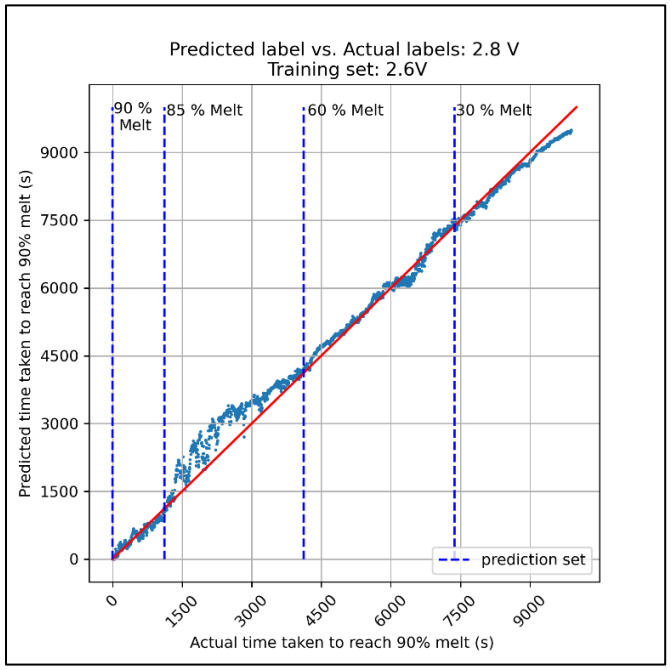

Figure 22. Scatter plot comparing the ANN predictions (using T'_{30}, T'_{60}, T'_{90}) with experimental data for test data set of 2.8 V (and training data set of 2.6 V).

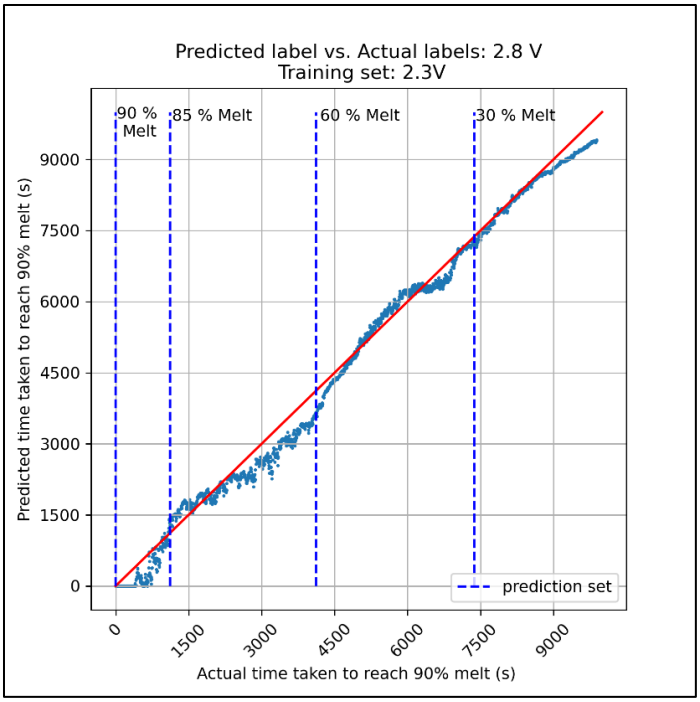

Figure 23. Scatter plot comparing the ANN predictions (using T'_{30}, T'_{60}, T'_{90}) with experimental data for test data set of 2.8 V (and training data set of 2.3 V).

Table 5. Average absolute error in predictions (from T'_{30}, T'_{60}, T'_{90}) during final 1800 s prior to attaining a melt-fraction of 90%.

Training / Prediction	2.3 V [1.08 W]	2.6 V [1.4 W]	2.8 V [1.6 W]
2.3 V [1.08 W]		240 s	204 s
2.6 V [1.4 W]	368 s		102 s
2.8 V [1.6 W]	239 s	190 s	

3.4 Performance Comparison of ANN trained on Surface Temperatures with an ANN trained on PCM Temperatures

The profile of transient surface-temperature data recorded in these experiments were similar to that of the temperature transients recorded within the mass of PCM. The ANN model is trained using the transient PCM-temperature data recorded in the experiments: and are denoted as T_{30}, T_{60}, and T_{90} (as the inputs). Another ANN model is trained using the transient surface-temperature data recorded in the same experiments: and are denoted as T'_{30}, T'_{60}, and T'_{90} (as the inputs) instead of the PCM temperatures. The topology of the neural networks and the τ' labels are the same as before.

3.4.1 Training Set: 2.6 V; Prediction Set: 2.8 V

Using the 2.6V dataset for training and deploying the ANN model (trained using transient PCM-temperature data) to obtain the predictions on the 2.8V input condition then yields the scatter plot in Fig. 24. However, when we use transient surface-temperature data to train the ANN model, the scatter plot is not as smooth. This is evident in Fig. 25. The surface thermocouples are exposed to higher levels of noise from the ambient environment (as compared to that of the thermocouples immersed in the mass of PCM). As a result, the profile of the transient surface-temperature data is not as smooth (as compared to that of the transient PCM-temperature data). Hence, the fluctuations in the predicted values are observed to be higher for the ANN models trained using the transient surface-temperature data. Despite this impediment, the average error in the last 1800 s is 502 s (~6% of the total cycle time).

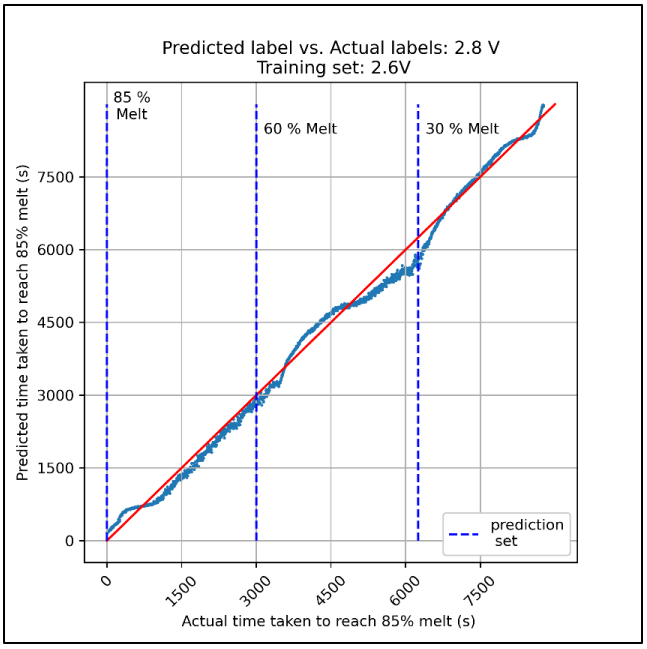

Figure 24. Scatter plot comparing the ANN predictions (using T_{30}, T_{60}, T_{90}) with experimental data for test data set of 2.8 V (and training data set of 2.6 V).

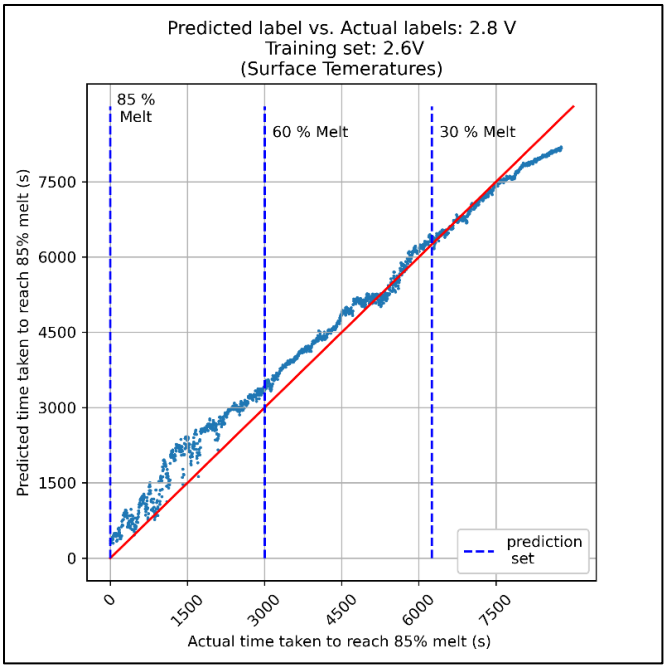

Figure 25. Scatter plot comparing the ANN predictions (using T'_{30}, T'_{60}, T'_{90}) with experimental data for test data set of 2.8 V (and training data set of 2.6 V).

3.4.2 Training Set: 2.3 V; Prediction Set: 2.8 V

A significant difference is observed between the performances of the ANN trained on transient PCM temperature data versus that of the ANN trained on transient surface temperature data (for the particular case of 2.3 V/ 2.8 V training/ prediction sets). The ANN model is trained on the 2.3 V set and deployed to predict on the 2.8 V dataset. The results for the predictions from the ANN model are plotted in Fig. 26. At approximately 3000 s prior to reaching 85% melt-fraction, the prediction error is observed to peak to a value of -1000 s. However, the average absolute error in the last 1800 s (before reaching 85% melt fraction) is 331 s, which corresponds to a minute fraction (~4%) of the total time to reach 85% melt-fraction. In this specific case, the deviations are substantially minimized when surface temperatures are deployed to train the network, as evident in Fig. 27. Scatter plots for other combinations of training and prediction datasets are included in Appendix F.

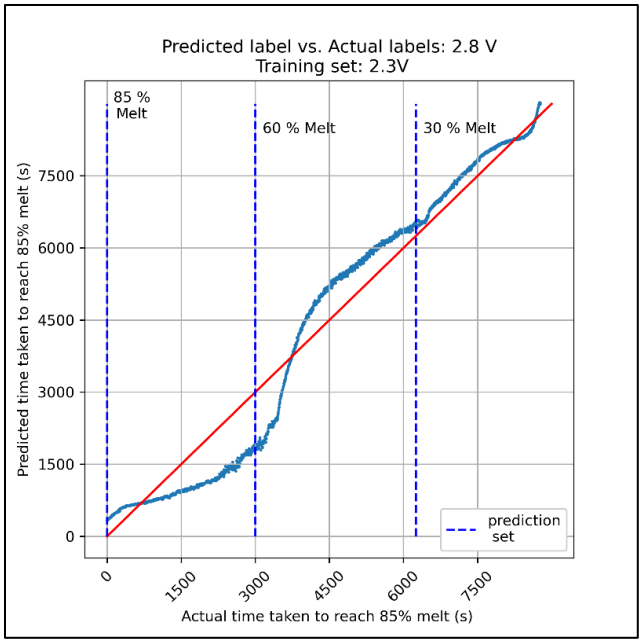

Figure 26. Scatter plot comparing the ANN predictions (using T_{30}, T_{60}, T_{90}) with experimental data for test data set of 2.8 V (and training data set of 2.3 V).

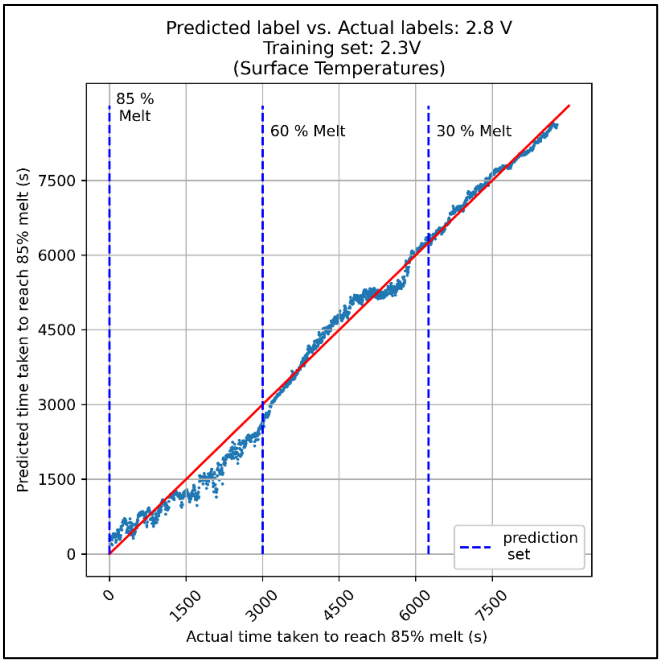

Figure 27. Scatter plot comparing the ANN predictions (using T'_{30}, T'_{60}, T'_{90}) with experimental data for test data set of 2.8 V (and training data set of 2.3 V).

At lower melt-fractions, the prediction errors are lower for ANN model trained using transient surface-temperature data than that of the ANN model trained using transient PCM temperature data (for target melt fraction of 85%). Line graphs are utilized to compare the error in prediction for the two input categories — transient surface-temperature data and transient PCM-temperature data. For instance, in Fig. 28 (training set: 2.3 V, prediction set: 2.6 V), for abscissa values in the range of 6,000 s to 10,000 s; lower values of absolute error are obtained for the predictions from the ANN model trained using transient surface-temperature data, compared to that of the ANN model trained using PCM temperature data. This trend is again evident in Fig. 29 (training set: 2.8 V, prediction set: 2.6 V) for abscissa values ranging between 6,500 s and 9,000 s.

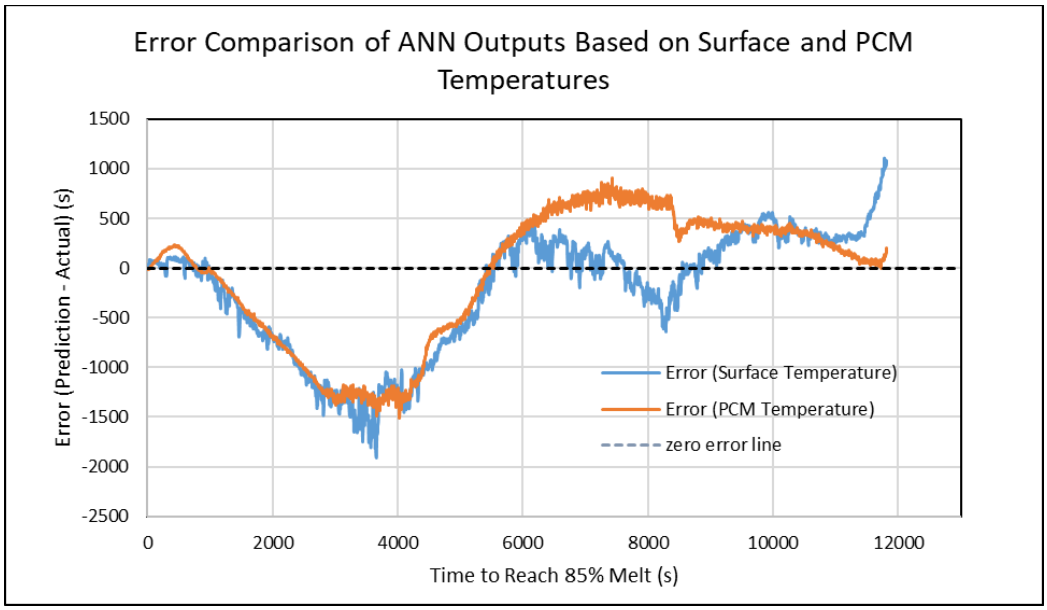

Figure 28 Comparison of error in predictions from the ANN model trained using transient surface-temperature data and transient PCM-temperature data (for test data set of 2.6V and training data set of 2.3V).

For yet another case (training set: 2.6 V, prediction set: 2.3 V), it can be seen from Fig. 30 that the predictions from the ANN model (that was trained using transient surface-temperature data) yields lower magnitudes of the absolute error than that of the ANN model trained using the PCM temperature data for abscissa values ranging from 7,000 s to 12,000 s. Similar trends (lower error in the initial stages of the cycle) are evident in the rest of training/ prediction combinations (Figs. 31-32).

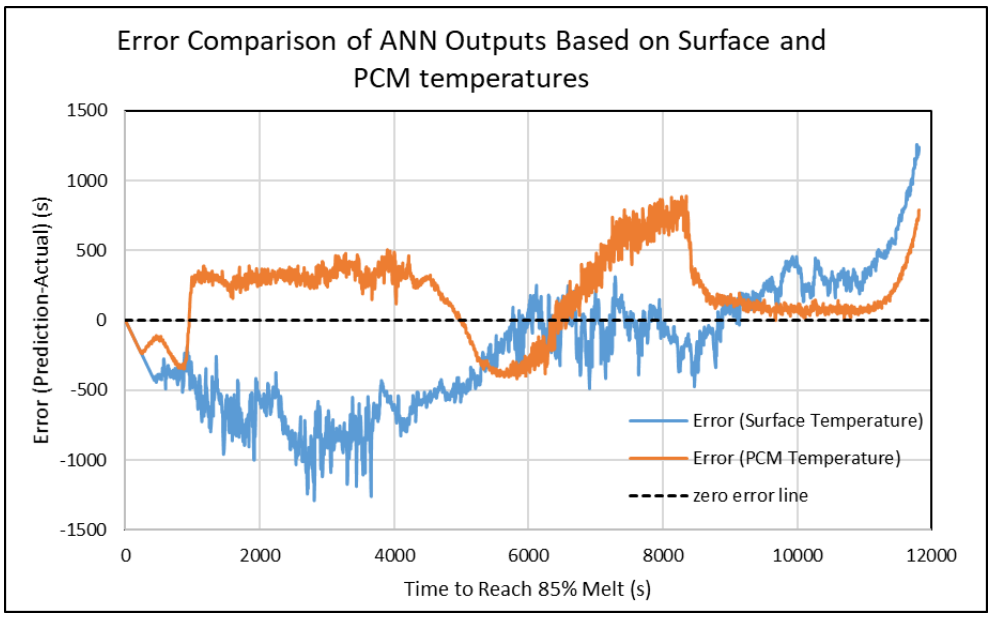

Figure 29. Comparison of error in predictions from the ANN model trained using transient surface-temperature data and transient PCM-temperature data (for test data set of 2.6V and training data set of 2.8V).

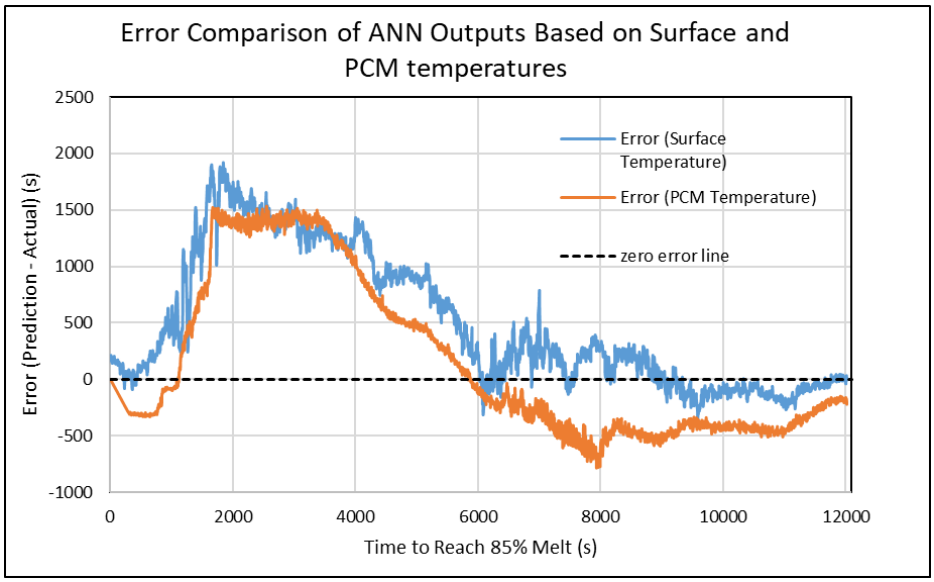

Figure 30. Comparison of error in predictions from the ANN model trained using transient surface-temperature data and transient PCM-temperature data (for test data set of 2.3V and training data set of 2.6V).

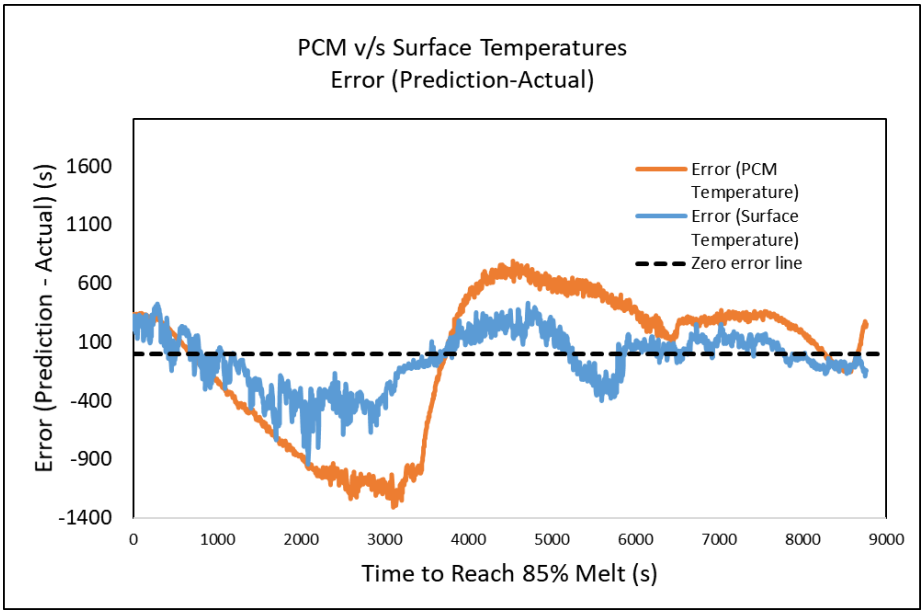

Figure 31. **Comparison of error in predictions from the ANN model trained using transient surface-temperature data and transient PCM-temperature data (for test data set of 2.8 V and training data set of 2.3V).**

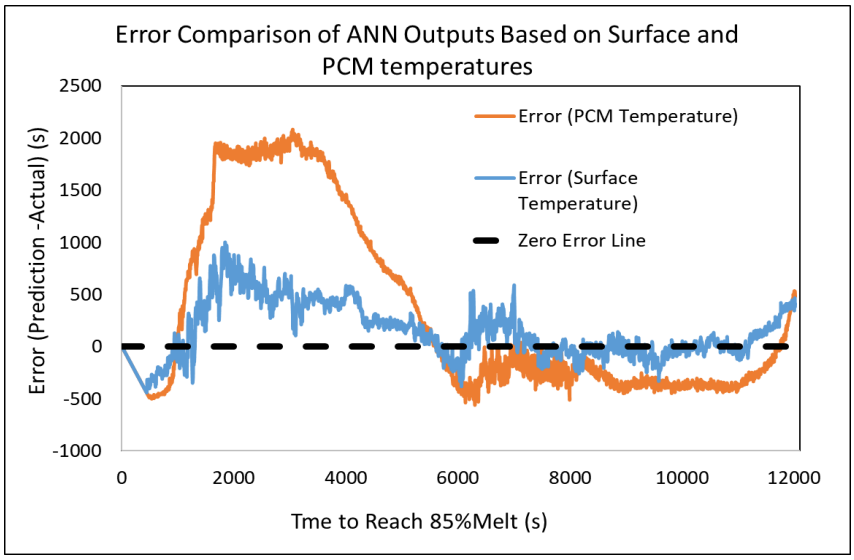

Figure 32. Comparison of error in predictions from the ANN model trained using transient surface-temperature data and transient PCM-temperature data (for test data set of 2.3 V and training data set of 2.8 V).

Table 6 summarizes the average absolute errors in prediction in the final 1800 s (prior to attaining a melt-fraction of 85%) for all combinations of training and prediction datasets. %. Comparison of the tabulated errors (between Table 3 and Table 4), shows that the transient surface-temperature data do not conclusively provide a better strategy for training the ANN models (instead of leveraging the transient PCM-temperature data), specifically for improving the accuracy of the predictions during the final stages of melt-cycle and close to the target values of the melt-fraction. Despite being higher the magnitude of the errors is still less than 600 s (10 minutes), when the real-time forecasting is performed 1800 s (30 minutes) prior to reaching the target melt-fraction of 85% Green colored cells depict the input (transient surface-temperature data or transient PCM-temperature data) providing for a lower magnitude of error. Whereas, red cells denote a higher magnitude of error. Comparison of the tabulated errors, shows that the transient

surface-temperature data do not conclusively provide a better strategy for training the ANN models (instead of leveraging the transient PCM-temperature data), specifically for improving the accuracy of the predictions during the final stages of melt-cycle and close to the target values of the melt-fraction. However, the errors are still appreciably low. From a functional standpoint, we can feed surface temperatures to an ANN to predict the time to reach a predefined melt-fraction. It may be noted that underprediction of the time is desirable (it is more reliable) – since over-prediction of the time can cause complete melting of the PCM in the TES – which is a catastrophic failure (since the PCM would then need to be supercooled to achieve nucleation and freezing). For electronics with intermittent operating cycles (i.e., fluctuating duty cycles), this method can be used to leverage the benefits accrued for deploying salt hydrates as PCMs in TES platforms (higher reliability and energy storage capacities with augmented power ratings) while also obviating supercooling.

Table 6 Average absolute error in the final 1800 s (prior to attaining a melt-fraction of 85%) for different training/prediction data-set combinations using transient PCM temperature data or transient surface-temperature data

	ANN Inputs – PCM Temperatures				**ANN Inputs – Surface Temperatures**		
Prediction / Training	**2.3 V**	**2.6 V**	**2.8 V**		**2.3 V**	**2.6 V**	**2.8 V**
2.3 V		190 s	331 s	**2.3 V**		202 s	206 s
2.6 V	423 s		167 s	**2.6 V**	589 s		502 s
2.8 V	654 s	233 s		**2.8 V**	280 s	448 s	

Also, it may be noted that for ANN model predictions using transient PCM-temperature data, the error in the predictions is lower when the input power (or input voltage) for the training data is closer to the input voltage of the prediction set. In other words, when 2.6 V data is used for training, the error in the predictions is lower for 2.8 V input conditions than that of the 2.3 V input conditions. Similarly, when the 2.8 V data is used for training, the error in the predictions is lower for 2.6 V input conditions than that of the 2.3 V input conditions.

In contrast, it may be noted that for ANN model predictions using transient surface-temperature data, the error in the predictions is lower when the input power (or input voltage) for the training data is starkly different compared to the input voltage of the prediction set. In other words, when 2.8 V data is used for training, the error in the predictions is lower for 2.3 V input conditions than that of the 2.6 V input conditions. Similarly, when the 2.3 V data is used for training, the error in the predictions is lower for 2.8 V input conditions than that of the 2.6 V input conditions. This contrast in the prediction capabilities of the ANN model can be attributed to the nature of the training data set itself. On closer observation, it may be noticed that the transient surface-temperature data has more acute levels of fluctuations (owing to exposure to free convection to the ambient air) than that of the transient PCM temperature data (owing to the high thermal energy storage capacity locally within the PCM)—that tends to damp out any acute temperature fluctuations due to their higher thermal-inertia/ thermal-inductance and thermal-capacitance.

Also, it is worth noting that for ANN model predictions using transient surface-temperature data, the error in the predictions is lower when the input power (or input voltage) for the training data is 2.3 V. The error in the predictions is highest when the input power (or input voltage) for the training data is 2.6 V. Whereas, the error in the predictions is moderately high when the input power (or input voltage) for the training data is 2.8 V. This anomalous trend can be explained by exploring the nuances of the experimental observations. During the melting cycle, especially at higher power input conditions (2.6 V and 2.8 V experiments) – it was observed that the rate of propagation of the melt front was fast enough that it partially lifted the solid mass of PCM above it by a minute amount. This was akin to a hydraulic ram actuation caused by the volumetric expansion due to solid-to-liquid phase change as the liquid PCM —which has lower density than that of the solid phase (and the solid mass of PCM above the melted liquid-phase) —acts like a hermetically sealed piston preventing the liquid PCM for leaking up. At one point, when sufficient amount of PCM has melted, the plastic tube embedded in the solid mass of PCM (which causes an opposing reaction force) restores of the solid mass of PCM back towards the original position. This caused a ripple effect in the temperature transients that were recorded by both the thermocouples embedded in the PCM and by the thermocouples mounted on the surface of the measuring cylinder (this occurred typically towards the end of the melt cycle and at high values of melt fraction, when the melt fraction exceeded ~80%). The temperatures dip slightly. As a result, the training data set for these cases cause distortions in the parameters defining each neuron in the ANN model (i.e., the weight and the bias). Consequently, the predictions from these

ANN models display high magnitudes of error and are also less reliable (i.e., often cause over-predictions). However, at lower power input conditions (2.3 V experiments) – the melt front propagated very slowly (since the power input was barely in excess of the heat loss from the measuring cylinder by free convection). As a result, the solid mass of PCM was virtually undisturbed in these experiments. As a result, there is less distortion in the parameters defining individual neurons. Consequently, the predictions from the ANN model trained using transient surface temperature data from the 2.3 V experiments have better fidelity and the magnitude of the error is lower. Further, the predictions are more reliable (i.e., the results tend to underpredict the time required to reach the target value of 85% melt fraction) for major portion of the melt cycles. The plots of the experimental data for the different heater power inputs are provided in the Appendix H. In addition to the above discussed aspects, the predictions on uncalibrated temperature data are presented in Appendix J. Further, results in Appendix K deal with two aspects: (1) the effect of utilizing data with different degrees of noise for training the ANN, and (2) the effect of utilizing a consolidated data set (consisting of data from experiments with different heater power inputs).

CHAPTER IV

CONCLUSION AND RECOMMENDATIONS

4.1 Summary of Results

In this study, a representative procedure for achieving real-time predictions of the time remaining to reach a chosen melt-fraction is demonstrated. The core of this procedure is an artificial neural network (ANN) which is used for predicting the values of a non-dimensional parameter, τ'. This parameter is a non-dimensional equivalent of the time remaining in the PCM melting process to reach a chosen value (target value) of the melt fraction (i.e., such that the PCM attains a chosen melt-fraction). This study proves the feasibility for obtaining real-time predictions using MLP/ ANN models for improving the reliability and efficacy of TES platforms that leverage PCMs. This approach therefore enables the successful deployment of 'Cold Finger Technique' (CFT) to obviate supercooling. Thus, the storage capacity of the TES is maximized while also enhancing the reliability and resilience of the cooling strategy. This is achieved by deploying the MLP/ ANN models for real-time prediction of the time remaining to attain a target (predefined) melt-fraction during the melting-cycle. The target value of melt-fraction chosen in this study is 85% (or 90%). Experiments were performed using digital data acquisition apparatus (including flow visualization by a digital-camera, I.R. thermography measurements for verification of temperature uniformity in different segments of the experimental apparatus and measurement of temperature transients using thermocouples that were mounted strategically at specific locations corresponding to the location of the

liquid meniscus of the PCM for chosen values of melt-fractions). The experiments were performed for power input values of 1.08 W, 1.4 W and 1.6 W. Data sets obtained for a chosen power input condition was used for predicting (and validating) the values for another set of power input conditions. Two different approaches were explored for training the ANN models: (1) by using transient PCM temperature data; and (2) by using transient surface-temperature data.

The central idea of this study was to cross-test the ANN performance for different sets of training and validation data. Three different cases were studied to explore the efficacy of the method.

Case 1:

Initially the ANN model is trained to predict the value of time remaining to reach 90% melt-fraction (τ'_{90}). The ANN model is trained using transient PCM-temperature data obtained from thermocouples located at elevations corresponding to meniscus locations for melt-fraction values of 30%, 60%, and 85%. The predictions are achieved with an uncertainty as low as ± 5 minutes (± 10 minutes for two of the six combinations) in the final half an hour before 90% melt-fraction is achieved.

Case 2:

Similarly, the ANN model is trained using transient surface-temperature data obtained from thermocouples located at elevations corresponding to meniscus locations for melt-fraction values of 30%, 60%, and 90% (denoted as T'_{30}, T'_{60}, and T'_{90}, respectively). The ANN model is trained to predict the value of time remaining to reach 90% melt-fraction (τ'_{90}). The error from the ANN model predictions is lower for the case

involving training data sets that are based on the transient surface-temperature data (as compared to that of the ANN model predictions involving training data sets that are based on the transient PCM-temperature data). The lower error is chiefly due to one of the inputs, T'_{90}, being on the same level as the melt front when the PCM is at the target melt-fraction of 90%.

Case 3:

The ANN model is trained to predict the value of time remaining to reach 85% melt-fraction (τ'_{85}). The ANN model is trained using two different strategies: (a) transient PCM-temperature data; and (b) transient surface-temperature data. The ANN model is trained using transient PCM-temperature data obtained from thermocouples located at elevations corresponding to meniscus locations for melt-fraction values of 30%, 60%, and 90% (denoted as T_{30}, T_{60}, and T_{90}, respectively). Also, in a separate study, the ANN model is trained using transient surface-temperature data obtained from thermocouples located at elevations corresponding to meniscus locations for melt-fraction values of 30%, 60%, and 90% (denoted as T'_{30}, T'_{60}, and T'_{90}, respectively). Comparison of the errors in the predictions obtained from the ANN model for the two different strategies reveals that the latter strategy (i.e., leveraging transient surface-temperature data for training the ANN model) can indeed be utilized to improve the reliability of deploying CFT for a PCM based TES platform for providing supplemental cooling (especially, for thermal management in electronics cooling applications). On a granular level, the transient surface-temperature data suffer from higher levels of noise (i.e., larger levels of temperature fluctuations),

which in turn cause higher levels of fluctuations in the predicted values obtained from the ANN model.

4.2 Conclusion

In this study, the feasibility of a novel forecasting tool (based on ANN model) has been demonstrated for the purpose of improving the efficacy and reliability of CFT. This innovative machine learning technique can enhance the resilience of a dry-cooled powerplant. Data analytics and digitalisation are the innovations of the fourth industrial revolution. These innovations can aid in further development of resilient infrastructure as well as robust manufacturing processes. The relationship between sustainability and resilience is also apparent from this work. If power production is to remain sustainable in the near future, resilient designs are the way forward. The target applications of this technique include supplemental cooling platforms that can be deployed in a variety of applications that require PCM based TES devices (e.g., for reducing water usage in power plants, thermal management for electronics cooling applications, building thermal management, etc.)

For ANN models trained using transient PCM-temperature data, lower magnitudes of error in the predicted values were obtained when the input power of the training data set was similar to that of the predicted data set. For example, lower magnitudes of error were obtained when the training data set from the 2.6 V experiments were utilized for predicting the temporal values for the 2.8 V experiments. Similarly, lower magnitudes in error were obtained when the training data set from the 2.8 V experiments were utilized for predicting the temporal values for the 2.6 V experiments. In contrast, the magnitudes

of error were higher (and the values were over-predicted, i.e., the predictions were unreliable for major proportion of the melt cycle) for the 2.3 V experiments when either the data set from 2.6 V or from 2.8 V were utilized for training the ANN model. In general, the accuracy of predictions afforded by ANN models that were trained using transient surface-temperature data was higher in the initial stages of the cycle (however, higher levels of error are observed for these cases in the final stages of the melting cycle).

An anomalous decrease in temperature trends was observed for the temperature transients recorded at higher power input conditions (both for surface temperature and PCM temperature data). This was due to the volumetric expansion of the trapped liquid phase (upon melting from the solid phase) which caused the solid mass of PCM above to be displaced up (followed subsequently by a downward motion of the solid PCM caused by the restoring force of the plastic tube adhering to the solid mass of PCM at the top) – resulting in a sharp decrease in the temperature values recorded by thermocouples that were already submerged in the liquid PCM (and for the surface thermocouples that were mounted at similar heights from the base of the measuring cylinder). Consequently, the parameters for each neuron (e.g., weight, bias, etc.) in the ANN model were likely to be distorted – thus causing higher magnitude of errors in the predicted values and the predictions were unreliable (i.e., due to overpredictions) for major proportion of the melt cycle.

Following conclusions were derived from this study and are summarized below:

- The ANN technique developed in this study yields more accurate results, particularly in the final stages of the melting cycle, especially if the target melt-fraction is within

the range of melt-fractions used in the training data set for the corresponding temperature-transients. This strategy can obviate the insensitivity of the predicted values of the time remaining to attain the target value of melt-fraction that accrued from the ANN model predictions in the final stages of the melting cycle.

- When PCM temperature transients are used for training the ANN model, the errors in predictions are minimized if the heater input voltages (or input power values) are in similar ranges for both the training data-set and the prediction data-set.
- The error in predictions from the ANN model (trained on transient surface-temperature data) is lower as compared to that of the transient PCM-temperature data sets, especially during the initial stages of the melting cycle (generally, when melt-fractions are less than 60%).
- ANN models trained using transient surface-temperature data corresponding to lower power input conditions yield lower magnitudes of error (since anomalous temperature transients were minimized at lower power input conditions due to the gradual progression of the PCM upwards into the mass of solid PCM). The predictions were also found to be reliable for major proportion of the melt cycle (i.e., the values were underpredicted).
- This method does not demand additional equipment or additives (such as nucleating agents and gelling agents, thus avoiding additional costs and operational burdens). Since additives degrade over time – this adds to the uncertainty for long-term operation and can compromise the reliability.

- A strength of this method is that it is independent of the absolute values of the temperatures. This implies that even if a thermocouple is wrongly calibrated (or if the thermocouple calibration is compromised), the predictions from the ANN model would still be fairly accurate (e.g., for the time remaining to attain a target value of melt-fraction).

Motivated by the potential application of inorganic PCMs in TES (that can be deployed for enhancing the reliability and resilience of thermal management devices), especially in electronics chip cooling platforms, in this study, the efficacy of deploying deep learning is explored for enhancing the energy storage capacity for CFT (without compromising the power rating) by forecasting the time required to reach a target melt-fraction. In these applications, the direct measurement of PCM temperature is often not possible due to packaging related issues. Measurement of surface-temperature transients are preferable for electronics packages (especially for those that are filled with PCMs) due to their simplicity, low cost, better reliability, as well as ease of manufacturing and fabrication. This strategy can yield lower failure rates while also providing ease of access for maintenance and repair operations. Forecasting strategies based on transient surface-temperature data also enable retrofitting of existing thermal-management platforms in electronics devices thus rendering additional capabilities for real-time predictions using ANN models (e.g., the time remaining for reaching a target melt-fraction of PCMs that are filled inside the electronics package). These capabilities do not typically accrue from strategies involving measurement of temperature transients from sensors that are immersed within the volume of PCM, i.e., from temperature sensors mounted inside the

electronics package (instead of the surface-mounted temperature sensors). Hence, this study demonstrates the efficacy of ANN models for electronics chip cooling applications and can be used in conjunction with PCM filled heat sinks to improve their reliability for thermal management applications (e.g., in data centers) while also impacting the sustainability of these data-centers by reducing the usage of water (e.g., reducing the demand for chilled water and, in-turn, the evaporative losses from the cooling towers) as well as the net power consumption by the data centers. Secondary benefits that accrue from such endeavors – include augmented cooling capabilities and enhanced performance of the thermal management platforms, better durability and increased longevity of the computing platforms; since - more effective deployment of the thermal management platforms that leverage such real-time predictions capabilities from the ANN models result in better temperature uniformity (i.e., mitigating the hot-spots in the packages of the electronics chips and within the chips themselves).

4.3 Recommendations

Based on the findings of this study, following recommendations are provided to improve the robustness and scalability and further prove the efficacy of the tool developed in this study.

- Experimental validation of the numerical predictions from the ANN model can be explored for a TES platform that leverages salt hydrates as PCMs (such as Glauber's salt).

- Training the neural network with a consolidated data set consisting of multiple duty cycles can be explored (for the purpose of further minimizing the errors in the predicted values).
- The neural network topology can be optimized. Parameters like number of hidden layers, number of nodes in a hidden layer can be optimized to prevent overfitting or underfitting of the training set.
- To establish the robustness of this algorithm, uncertainties in temperature measurement can be incorporated in the ANN training process and quantifying the resultant uncertainty in the time.
- Infrared images captured in the experiments can be used to train an artificial neural network or a separate class of machine learning technique to develop an advanced monitoring tool.
- Implementing these experimental studies and ANN model development on actual (e.g., “commercially off-the shelf” or “COTS”) electronics chips that leverage PCM filled heat sinks.
- The results from this study can be complemented by exploring alternate experimental platforms (e.g., different aspect ratios of the measuring cylinder and for different types of PCMs, inclination angle of the measuring cylinder containing different types of PCMs, location of heater, types of heaters, location of individual sensors, different ranges of power inputs, etc.).

REFERENCES

[1] B. Xu, P. Li, and C. Chan, "Application of phase change materials for thermal energy storage in concentrated solar thermal power plants: A review to recent developments," *Applied Energy*, vol. 160, pp. 286-307, 2015/12/15/ 2015, doi: https://doi.org/10.1016/j.apenergy.2015.09.016

[2] J. Jeon, J.-H. Lee, J. Seo, S.-G. Jeong, and S. Kim, "Application of PCM thermal energy storage system to reduce building energy consumption," *Journal of Thermal Analysis and Calorimetry*, vol. 111, no. 1, pp. 279-288, 2013/01/01 2013, doi: 10.1007/s10973-012-2291-9.

[3] Department of Energy, “ARPA-E Energy”, [Online]. Available: https://arpa-e.energy.gov/sites/default/files/documents/files/ARID_ProgramOverview.pdf [Accessed: 09.13.2021]

[4] C. A. Dieter *et al.*, "Estimated use of water in the United States in 2015," in "Circular," Reston, VA, Report 1441, 2018. [Online]. Available: http://pubs.er.usgs.gov/publication/cir1441

[5] E. Williams and J. Simmons, “Water in the Energy Industry: An Introduction”, BP, 2013.

[6] IEA (2020), “Introduction to the water-energy nexus” [Online]. IEA, Paris. Available: https://www.iea.org/articles/introduction-to-the-water-energy-nexus [Accessed: 09.20.2021]

[7] K. Birkinshaw, M. Marwan and R. L. Therkelsen, "Comparsion of Alternate Cooling Technologies for California Power Plants Economic, Environmental and Other Tradeoffs," California Energy Commission, 2002

[8] M. M. El-Halwagi, D. Sengupta, E. N. Pistikopoulos, J. Sammons, F. Eljack, and M.-K. Kazi, "Disaster-Resilient Design of Manufacturing Facilities Through Process Integration: Principal Strategies, Perspectives, and Research Challenges,", *Frontiers in Sustainability*, Original Research vol. 1, no. 8, 2020-November-16 2020, doi: 10.3389/frsus.2020.595961

[9] W. Q. Meeker and L.A. Escobar, "Reliability: The Other Dimension of Quality," *Quality Technology & Quantitative Management*, vol. 1, no. 1, pp. 1-25, 2004, doi: 10.1080/16843703.2004.11673062

[10] M. Pedram and S. Nazarian, "Thermal Modeling, Analysis, and Management in VLSI Circuits: Principles and Methods," *Proceedings of the IEEE*, vol. 94, no. 8, pp. 1487-1501, 2006, doi: 10.1109/JPROC.2006.879797.

[11] J. R. Black, "Electromigration—A brief survey and some recent results," *IEEE Transactions on Electron Devices*, vol. 16, no. 4, pp. 338-347, 1969, doi: 10.1109/T-ED.1969.16754.

[12] G. E. Moore, "Cramming More Components Onto Integrated Circuits," *Proceedings of the IEEE*, vol. 86, no. 1, pp. 82-85, 1998, doi: 10.1109/JPROC.1998.658762.

[13] M. Waldrop, "The chips are down for Moore's law," *Nature News*, vol. 530, p. 144, 02/01 2016, doi: 10.1038/530144a.

[14] S. M. S. Murshed and C. Nieto de Castro, "A critical review of traditional and emerging techniques and fluids for electronics cooling," *Renewable and Sustainable Energy Reviews,* vol. 78, pp. 821-833, 10/01 2017, doi: 10.1016/j.rser.2017.04.112.

[15] Y. Maydanik, S. Vershinin, M. Korukov, and J. Ochterbeck, "Miniature loop heat pipes-a promising means for cooling electronics," *IEEE Transactions on Components and Packaging Technologies*, vol. 28, pp. 290-296, 2005.

[16] X. Wei and Y. Joshi, "Stacked Microchannel Heat Sinks for Liquid Cooling of Microelectronic Components," *Journal of Electronic Packaging,* vol. 126, no. 1, pp. 60-66, 2004, doi: 10.1115/1.1647124.

[17] S. V. Garimella, V. Singhal, and L. Dong, "On-Chip Thermal Management With Microchannel Heat Sinks and Integrated Micropumps," *Proceedings of the IEEE,* vol. 94, no. 8, pp. 1534-1548, 2006, doi: 10.1109/JPROC.2006.879801.

[18] M. Jaworski and R. Domański, "A novel design of heat sink with PCM for electronics cooling," in *10th International Conference on Thermal Energy Storage, Stockton*, 2006, vol. 31.

[19] F. L. Tan and C. P. Tso, "Cooling of mobile electronic devices using phase change materials," *Applied Thermal Engineering,* vol. 24, no. 2, pp. 159-169, 2004/02/01/ 2004, doi: https://doi.org/10.1016/j.applthermaleng.2003.09.005.

[20] R. Kandasamy, X.-Q. Wang, and A. S. Mujumdar, "Application of phase change materials in thermal management of electronics," *Applied Thermal Engineering,* vol. 27, no. 17, pp. 2822-2832, 2007/12/01/ 2007, doi: https://doi.org/10.1016/j.applthermaleng.2006.12.013.

[21] R. Kandasamy, X.-Q. Wang, and A. S. Mujumdar, "Transient cooling of electronics using phase change material (PCM)-based heat sinks," Applied Thermal Engineering, vol. 28, no. 8, pp. 1047-1057, 2008/06/01/ 2008, doi: https://doi.org/10.1016/j.applthermaleng.2007.06.010

[22] R. Baby and C. Balaji, "Thermal management of electronics using phase change material based pin fin heat sinks," *Journal of Physics: Conference Series*, vol. 395, p. 012134, 2012/11/26 2012, doi: 10.1088/1742-6596/395/1/012134.

[23] Z. Ling *et al.*, "Review on thermal management systems using phase change materials for electronic components, Li-ion batteries and photovoltaic modules," *Renewable and Sustainable Energy Reviews*, vol. 31, pp. 427-438, 2014/03/01/ 2014, doi: https://doi.org/10.1016/j.rser.2013.12.017.

[24] J. Hirschey, K. R. Gluesenkamp, A. Mallow, and S. Graham, "Review of Inorganic Salt Hydrates with Phase Change Temperature in Range of 5 to 60°C and Material Cost Comparison with Common Waxes," 2018.

[25] S. Byung Chul, K. Sang Done, and P. Won-Hoon, "Phase separation and supercooling of a latent heat-storage material," *Energy*, vol. 14, no. 12, pp. 921-930, 1989/12/01/ 1989, doi: https://doi.org/10.1016/0360-5442(89)90047-9.

[26] P. Hu, D.-J. Lu, X.-Y. Fan, X. Zhou, and Z.-S. Chen, "Phase change performance of sodium acetate trihydrate with AlN nanoparticles and CMC," *Solar Energy Materials and Solar Cells*, vol. 95, no. 9, pp. 2645-2649, 2011/09/01/ 2011, doi: https://doi.org/10.1016/j.solmat.2011.05.025.

[27] B. M. L. Garay Ramirez, C. Glorieux, E. San Martin Martinez, and J. J. A. Flores Cuautle, "Tuning of thermal properties of sodium acetate trihydrate by blending

with polymer and silver nanoparticles," *Applied Thermal Engineering,* vol. 62, no. 2, pp. 838-844, 2014/01/25/ 2014, doi: https://doi.org/10.1016/j.applthermaleng.2013.09.049.

[28] P. J. Shamberger and M. J. O'Malley, "Heterogeneous nucleation of thermal storage material LiNO3·3H2O from stable lattice-matched nucleation catalysts," *Acta Materialia,* vol. 84, pp. 265-274, 2015/02/01/ 2015, doi: https://doi.org/10.1016/j.actamat.2014.10.051.

[29] N. Kumar, D. Banerjee, and R. Chavez, "Exploring additives for improving the reliability of zinc nitrate hexahydrate as a phase change material (PCM)," *Journal of Energy Storage*, vol. 20, pp. 153-162, 2018/12/01/ 2018, doi: https://doi.org/10.1016/j.est.2018.09.005.

[30] N. Kumar, J. Hirschey, T. J. LaClair, K. R. Gluesenkamp, and S. Graham, "Review of stability and thermal conductivity enhancements for salt hydrates," *Journal of Energy Storage,* vol. 24, p. 100794, 2019/08/01/ 2019, doi: https://doi.org/10.1016/j.est.2019.100794.

[31] N. Kumar and D. Banerjee, "A Comprehensive Review of Salt Hydrates as Phase Change Materials (PCMs)," *International Journal of Transport Phenomena,* Article vol. 15, no. 1, pp. 65-89, 2018. [Online]. Available: https://proxy.library.tamu.edu/login?url=https://search.ebscohost.com/login.aspx?direct=true&db=asn&AN=131055909&site=eds-live.

[32] N. Kumar, R. V. Ness, R. Chavez, Jr., D. Banerjee, A. Muley, and M. Stoia, "Experimental Analysis of Salt Hydrate Latent Heat Thermal Energy Storage System With Porous Aluminum Fabric and Salt Hydrate as Phase Change Material

With Enhanced Stability and Supercooling," *Journal of Energy Resources Technology*, vol. 143, no. 4, 2020, doi: 10.1115/1.4048122.

[33] S. S. Haykin, "Neural networks and learning machines/Simon Haykin," ed: New York: Prentice Hall, 2009.

[34] S. Haykin, "Neural networks: a comprehensive foundation. 1999," *Mc Millan, New Jersey*, pp. 1-24, 2010

[35] N. Zhao, X. Wen, J. Yang, S. Li, and Z. Wang, "Modeling and prediction of viscosity of water-based nanofluids by radial basis function neural networks," *Powder Technology*, vol. 281, pp. 173-183, 2015/09/01/ 2015, doi: https://doi.org/10.1016/j.powtec.2015.04.058.

[36] D. Broomhead and D. Lowe, "Radial basis functions, multi-variable functional interpolation and adaptive networks," *Royal Signals and Radar Establishment Malvern (United Kingdom)*, vol. RSRE-MEMO-4148, 03/28 1988.

[37] Energy Information Administration, “Annual Electric Generator Report (Form EIA-860)”, 2017 early release data. Available: https://www.eia.gov/electricity/data/eia860/

[38] S. Gharbi, S. Harmand, and S. B. Jabrallah, "Experimental comparison between different configurations of PCM based heat sinks for cooling electronic components," *Applied Thermal Engineering*, vol. 87, pp. 454-462, 2015/08/05/ 2015, doi: https://doi.org/10.1016/j.applthermaleng.2015.05.024.

[39] PureTemp, *PureTemp29 Technical Data Sheet*, https://puretemp.com/wp-content/uploads/2021/06/PureTemp29TechnicalDataSheet.pdf

APPENDIX A

THERMOCOUPLE CALIBRATION CURVES

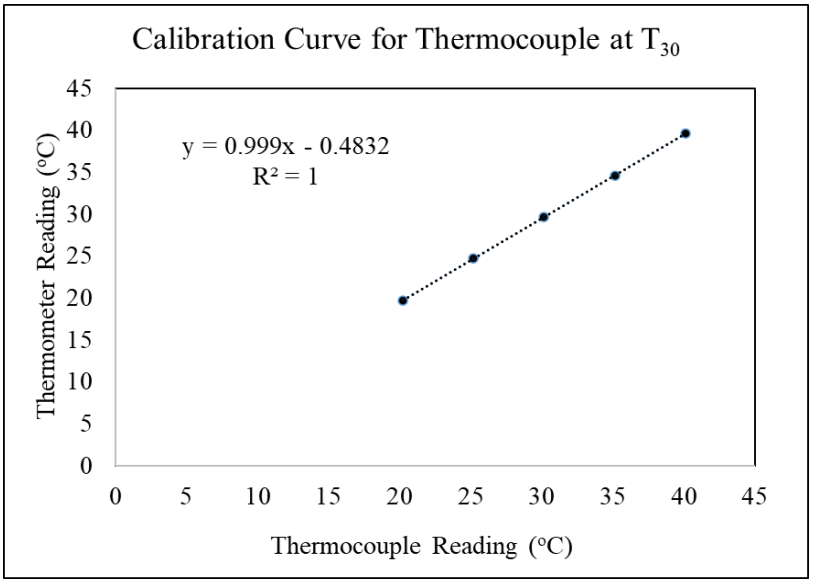

Figure 33**. Calibration curve for thermocouple measuring** T_{30}**.**

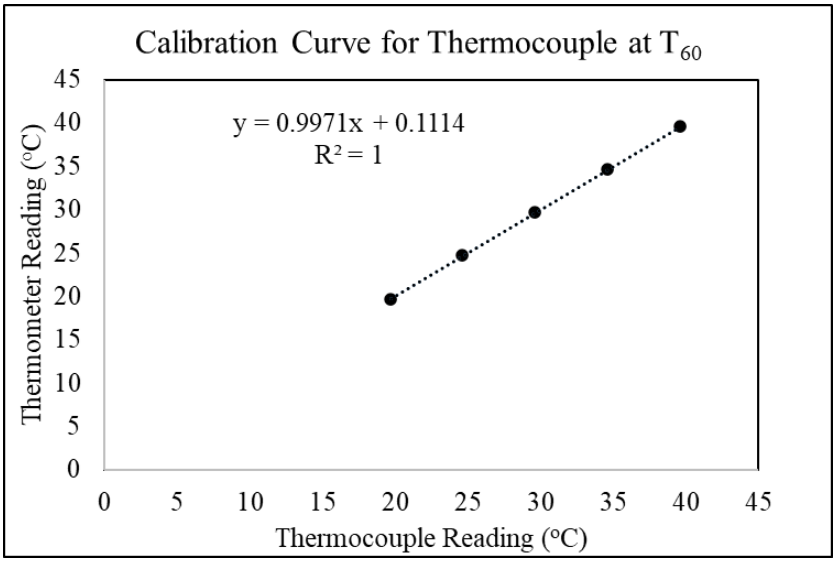

Figure 34. Calibration **curve for thermocouple measuring** T_{60}**.**

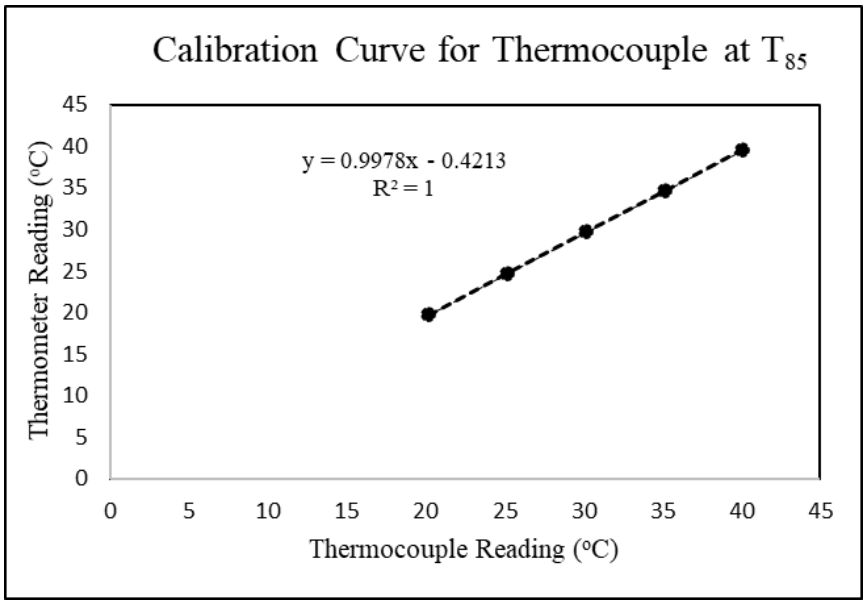

Figure 35. Calibration **curve for thermocouple measuring** T_{85}**.**

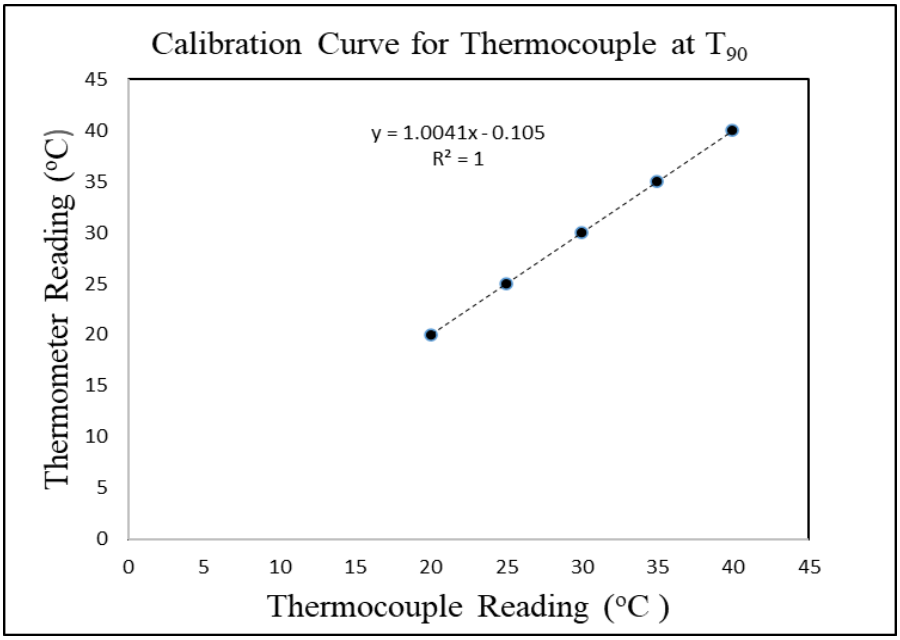

Figure 36. Calibration **curve for thermocouple measuring** T_{90}**.**

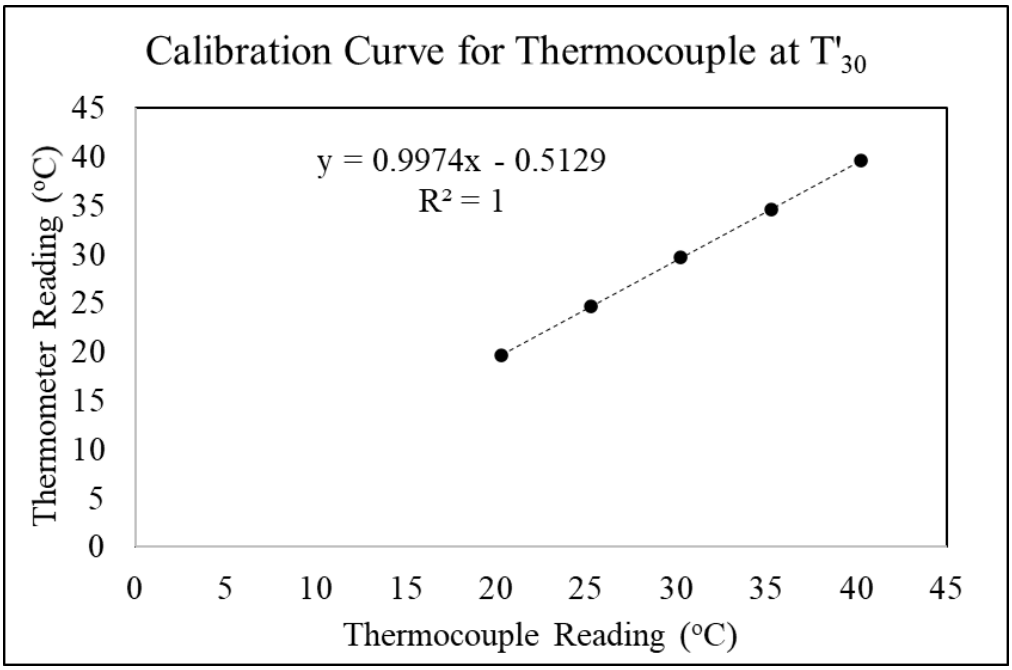

Figure 37. Calibration curve for thermocouple measuring T'30**.**

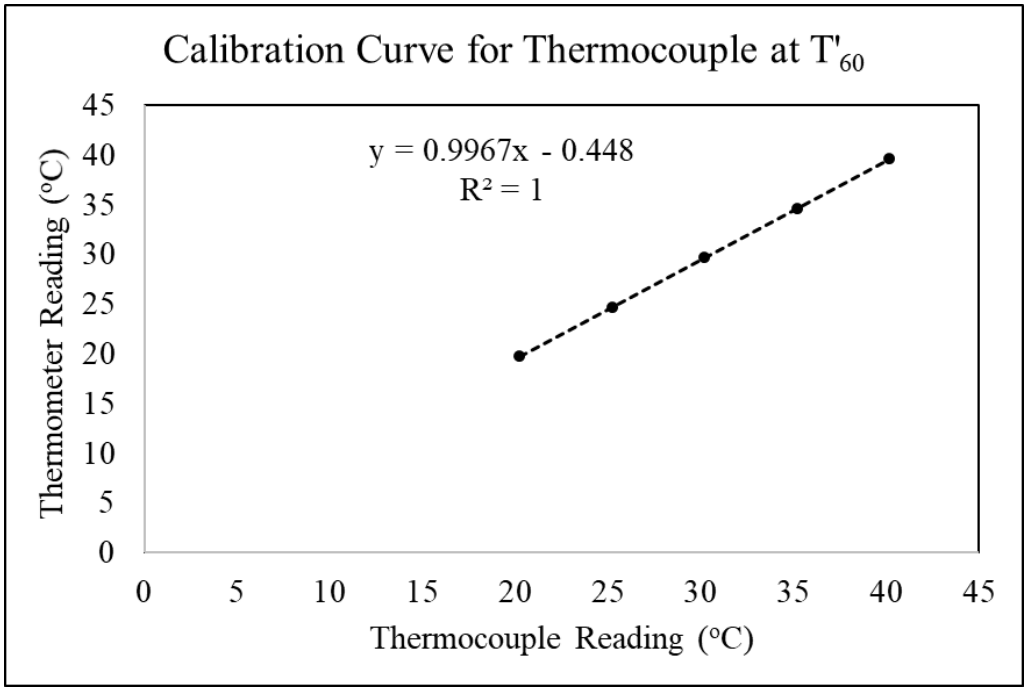

Figure 38. Calibration curve for thermocouple measuring *T'60***.**

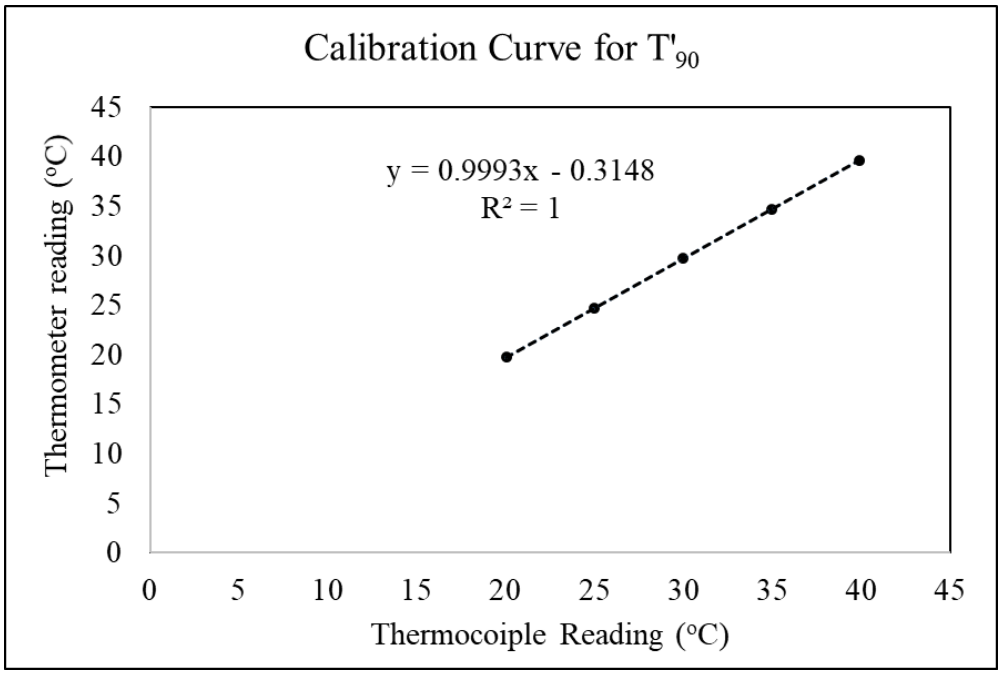

Figure 39. Calibration curve for thermocouple measuring *T'90*.

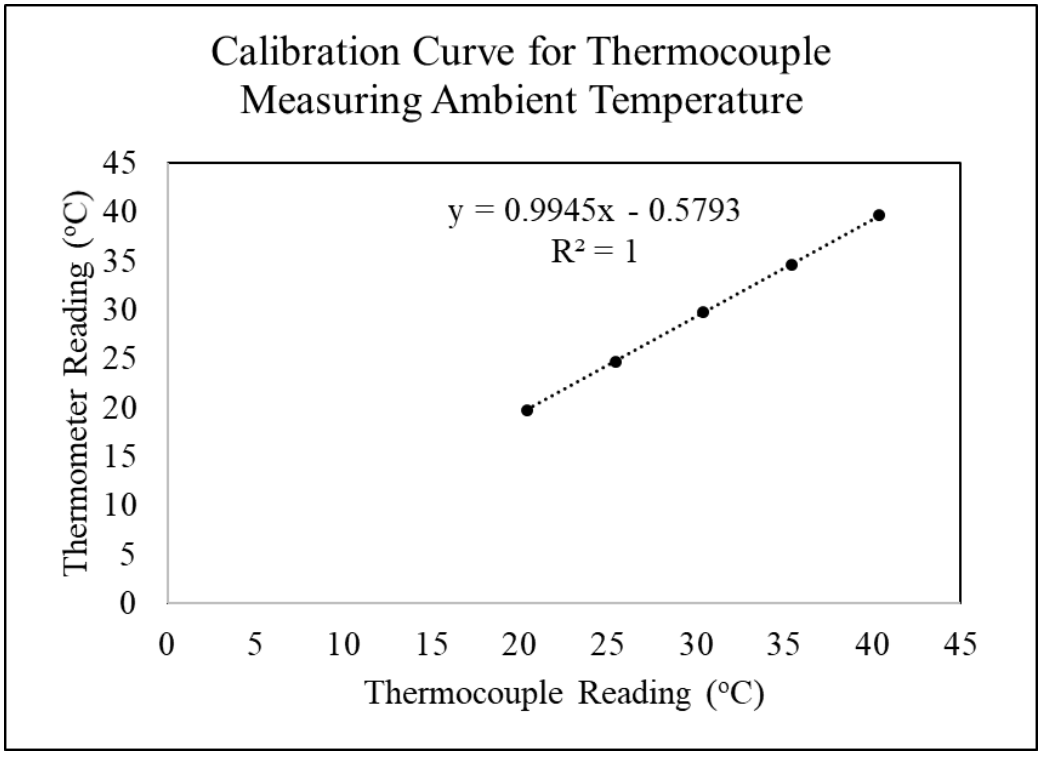

Figure 40. Calibration curve for thermocouple measuring the ambient temperature.

APPENDIX B

COMPUTING TOTAL MEASUREMENT UNCERTAINTY OF TEMPERATURE DATA

Table 7 Measurement uncertainties for different thermocouples

Thermocouple	u_{DAQ} (%)	u_t (%)	u_s (%)	u_{total} (%)
T_{30}	0.0011	0.36	0.053	0.36
T_{60}	0.0011	0.36	0.072	0.37
T_{85}	0.0011	0.36	0.406	0.54
T_{90}	0.0011	0.36	0.071	0.37
T'_{30}	0.0011	0.36	0.268	0.45
T'_{60}	0.0011	0.36	0.067	0.36
T'_{90}	0.0011	0.36	0.074	0.37
T_{amb}	0.0011	0.36	0.702	0.79

B.1 Sample Uncertainty Calculation for the Thermocouple located at a Height Corresponding to 30% melt-fraction within the PCM (T_{30})

For the thermocouple located at a height corresponding to 30% melt-fraction within the PCM, the following steps are followed to compute the total uncertainty. The steady state temperature data is collected for a duration of ~2 minutes (at a rate of 0.25 Hz) at water bath temperatures—20 °C, 25 °C, 30 °C, 35 °C, and 40 °C. A sample step by step calculation is shown here as an example (for the calibration performed with the water bath temperature set a fixed value of 20 °C).

1. Computation of u_{DAQ} – uncertainty due to DAQ precision

The expression for computing u_{DAQ} (in percentage) is:

$$\boldsymbol{u_{DAQ}}\,(\%) = \frac{\frac{\left(\boldsymbol{T_{cal.h} - T_{cal,l}}\right)}{\boldsymbol{2^{N_{bit}} - 1}}}{\boldsymbol{T_{DAQ}}} * \boldsymbol{100} \qquad (B.1)$$

where, $T_{cal,h}$ = Upper limit of the temperature range (used for calibration) = 40 °C

$T_{cal,l}$ = Lower limit of the temperature range (used for calibration) = 20 °C

T_{DAQ} = Mean Temperature measured by the DAQ (mean of the values recorded in 2 minutes).

N_{bit} = DAQ precision, which is equal to 16 in this work.

Substituting $T_{cal,h}$ = 40 °C, $T_{cal,l}$ = 20 °C, T_{DAQ} = 20.233 °C and N_{bit} = 16, in Equation (B.1):

$$\boldsymbol{u_{DAQ}}\,(\%) = \frac{\frac{(40 - 20)}{2^{16} - 1}}{20.233} * 100 = 0.0015\ \%$$

2. Computing u_t – uncertainty due to the precision of the NIST calibrated thermometer

The formula for computing u_t (as a percentage value) is:

$$\boldsymbol{u_t}\,(\%) = \frac{\boldsymbol{L.C.}}{\boldsymbol{T_{therm}}} * \boldsymbol{100} \qquad (B.2)$$

where, T_{therm} = temperature of the water bath as read by the thermometer

L.C. = Least count of the thermometer

Substituting T_{therm} = 19.7 °C (which is the actual value of the water bath temperature, i.e., for the target value of the water bath temperature – which was set for 20 °C), L.C = 0.1°C in Equation (B.2),

$$\boldsymbol{u_t}\,(\%) = \frac{0.1}{19.7} * 100 = 0.507\ \%$$

3. Computing u_s – statistical uncertainty considering the temporal fluctuations in the values of the measured data.

The formula for computing u_s (as a percentage value) is:

$$\boldsymbol{u_s}(\%) = \frac{\boldsymbol{\sigma_s}}{\boldsymbol{T_{DAQ}}} * \mathbf{100} \qquad (B.3)$$

where, σ_s= standard deviation of the steady state temperature data measured at a bath temperature of 20 °C,

T_{DAQ} = Mean Temperature measured by the DAQ, i.e., one of the thermocouples that were immersed in the water bath (mean of the values recorded for a total duration of 2 minutes at a sampling rate of 0.25 Hz).

Substituting σ_s = 0.0148, and T_{DAQ} = 20.233 in (B.3),

$$\boldsymbol{u_s}(\%) = \frac{0.0148}{20.233} * 100 = 0.0732\ \%$$

4. Computing u_{total} – total uncertainty (%)

The formula for computing us (as a percentage value) is:

$$\boldsymbol{u_{total}}(\%) = \sqrt{\boldsymbol{u_{DAQ}^2 + u_t^2 + u_s^2}} \qquad (B.4)$$

Substituting u_{DAQ} = 0.0015 %, u_t = 0.50 %, and u_s = 0.073 %, in (B.4)

$$\boldsymbol{u_{total}}(\%) = \sqrt{0.0015^2 + 0.50^2 + 0.073^2} \ = 0.51\ \%$$

Using a procedure similar to the sample uncertainty calculations at 20 °C shown above, steps 1 to 4 were repeated for obtaining the respective measurement uncertainty values corresponding to 25 °C, 30 °C, 35 °C, and 40 °C. The resulting uncertainties are summarised in the following table. The average uncertainty is obtained by considering the mean of the total uncertainty for all five temperatures:

Table 8 Summary of uncertainties in temperature measurement for T_{30} corresponding steady state temperatures—20 ºC, 25 ºC, 30 ºC, 35 ºC, 40 ºC

Water Bath Temperature (ºC)	u_{DAQ} **(%)**	u_t **(%)**	u_s **(%)**	u_{total} **(%)**
20	0.0015	0.5076	0.0732	0.5128
25	0.0012	0.4048	0.0589	0.4091
30	0.0010	0.3367	0.0411	0.3392
35	0.0008	0.2890	0.0538	0.2940
40	0.0007	0.2525	0.0385	0.2554
Average:	0.0011	0.3581	0.0531	**0.3621**

Hence, the average value of the total measurement uncertainty for the thermocouple located at a height corresponding to 30% melt-fraction (within the PCM) is 0.36% which makes the first entry in the column corresponding to u_{total} (%) in table 7.

B.2 Uncertainty in ambient temperature during a PCM melting experiment

The ambient temperature varies during the duration of the experiment. Hence, while reporting the *average* ambient temperature during a particular experiment, an additional source of statistical uncertainty (due to the temporal fluctuations in the measured values during the course of the experiment) needs to be taken into account.

$$\boldsymbol{u_{amb}}(\%) = \frac{\boldsymbol{\sigma_{amb}}}{\boldsymbol{T_{amb,DAQ}}} * \mathbf{100} \qquad (B.5)$$

where, σ_{amb} = standard deviation in the measured ambient temperature data during the course of a PCM melting experiment

$T_{amb,DAQ}$ = Mean Temperature measured by the DAQ, i.e., one of the thermocouples that were recording the ambient temperature (the mean of the values recorded for a total duration of the PCM melting experiment at a sampling rate of 0.20 Hz).

As an example, for the 2.6 V heater input experiment $T_{amb,DAQ}$ = 22.26 ºC, σ_{amb} = 0.24 ºC

$$\boldsymbol{u_{amb}}(\%) = \frac{0.24}{22.26} * 100 \ = 1.09\ \%$$

Therefore, while reporting the average temperature during the 2.6 V heater input experiment, in addition to an uncertainty of 0.79% (from table 7), an uncertainty of 1.09 % is taken into account. The total uncertainty is given by Equation B.6.

$$\boldsymbol{u_{total,amb}}(\%) = \sqrt{\boldsymbol{u_{DAQ}^2 + u_t^2 + u_s^2 + u_{amb}^2}} \qquad (B.6)$$

Substituting the values,

$$\boldsymbol{u_{total,amb}}(\%) = \sqrt{0.79^2 + 1.09^2} \quad = 1.34\ \%$$

Using the calibration constants from Fig. 40, the corrected value of temperature is computed corresponding to a thermocouple reading of $T_{amb,DAQ}$ = 22.26 ºC.

$$0.9945 \times (22.26) - 0.5793 = 21.6\,^{o}C$$

Therefore, the ambient temperature during the 2.6 V heater input experiment is 21.6 ±0.1 ºC.

APPENDIX C

REPEATABILITY OF PCM MELTING EXPERIMENTS

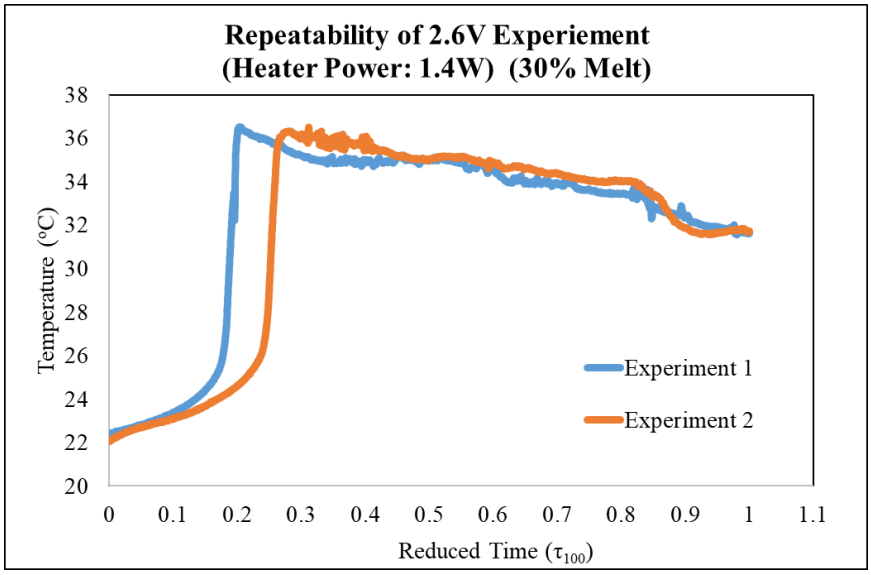

Figure 41. Temperature profile comparison for T_{30} for two experiments with a heater voltage of 2.6 V.

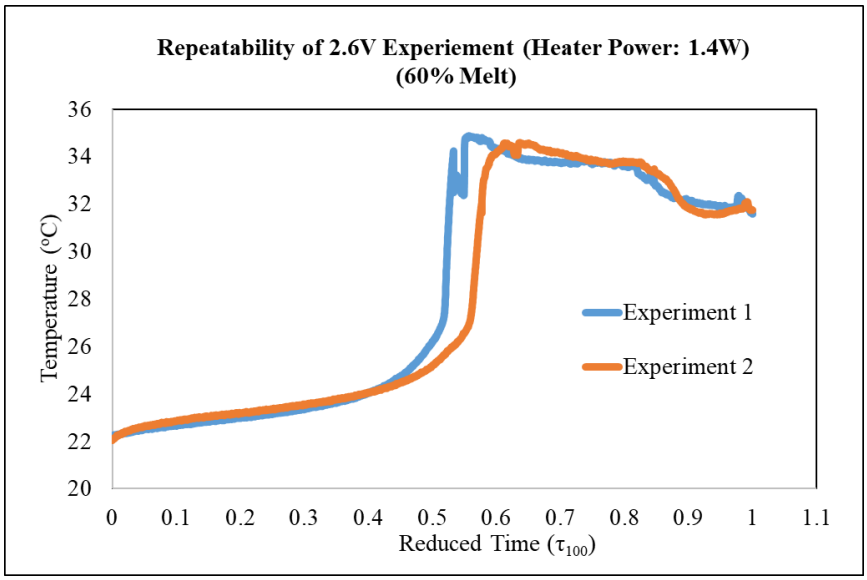

Figure 42. Temperature profile comparison for T_{60} for two experiments with a heater voltage of 2.6 V.

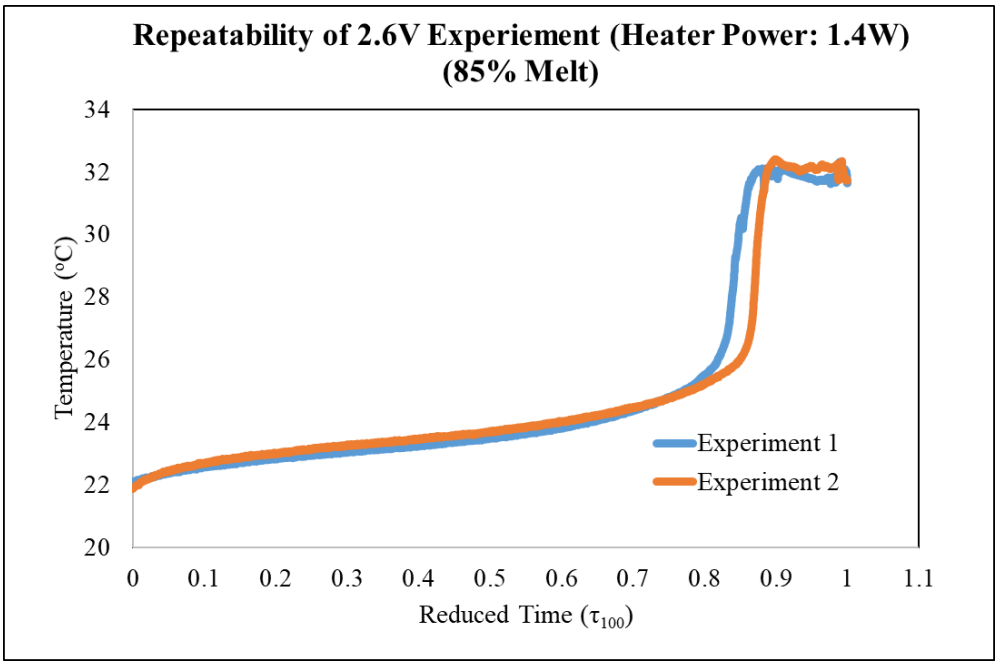

Figure 43. Temperature profile comparison for T_{85} for two experiments with a heater voltage of 2.6 V.

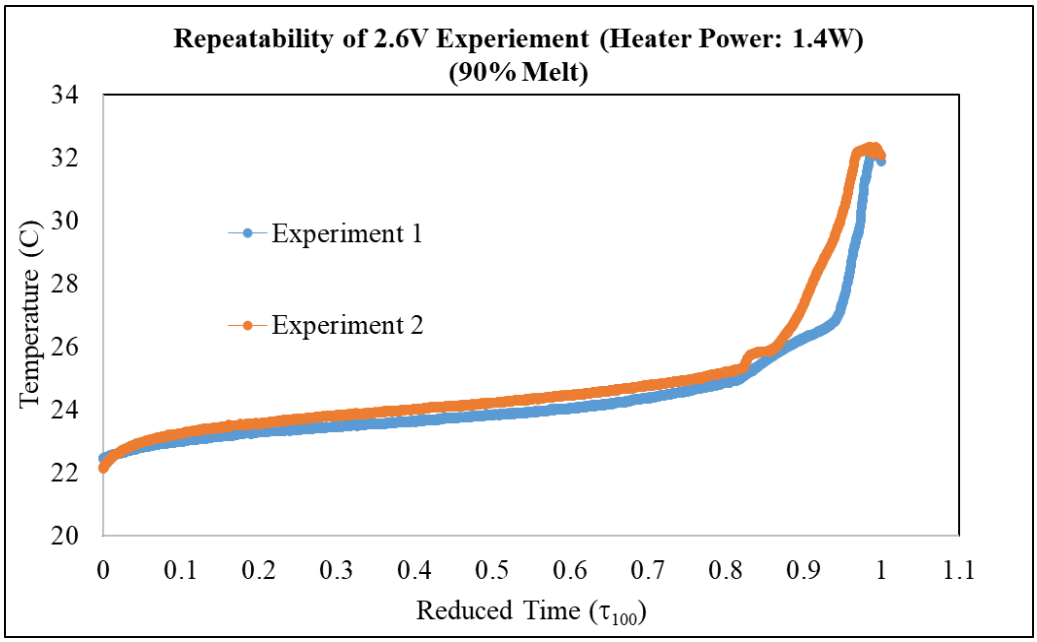

Figure 44. Temperature profile comparison for T_{90} for two experiments with a heater voltage of 2.6 V.

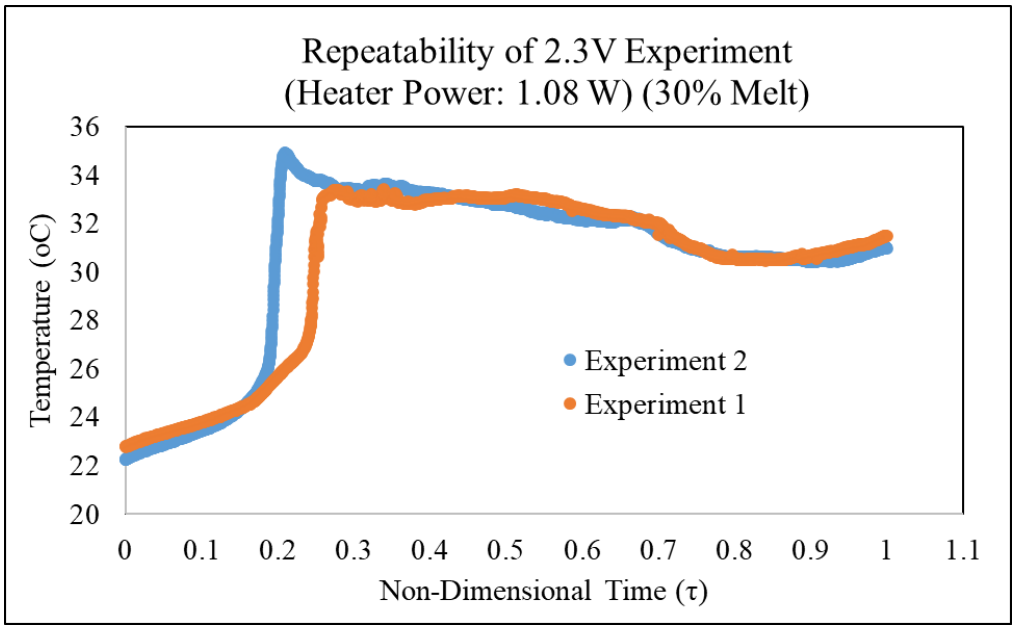

Figure 45. Temperature profile comparison for T_{30} for two experiments with a heater voltage of 2.3 V.

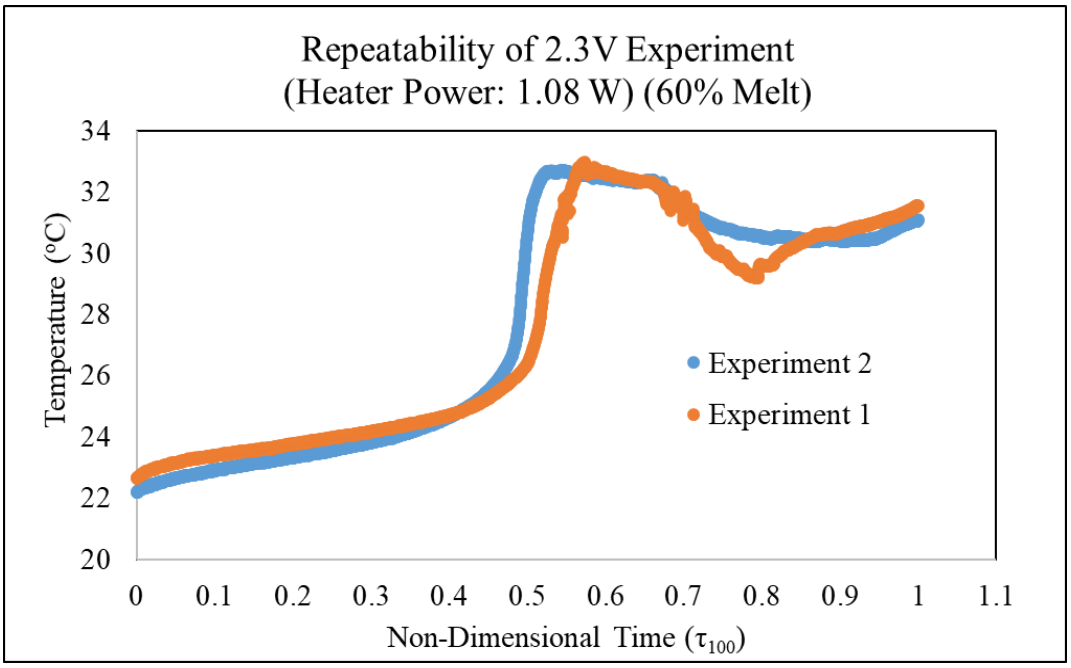

Figure 46. Temperature profile comparison for T_{60} for two experiments with a heater voltage of 2.3 V.

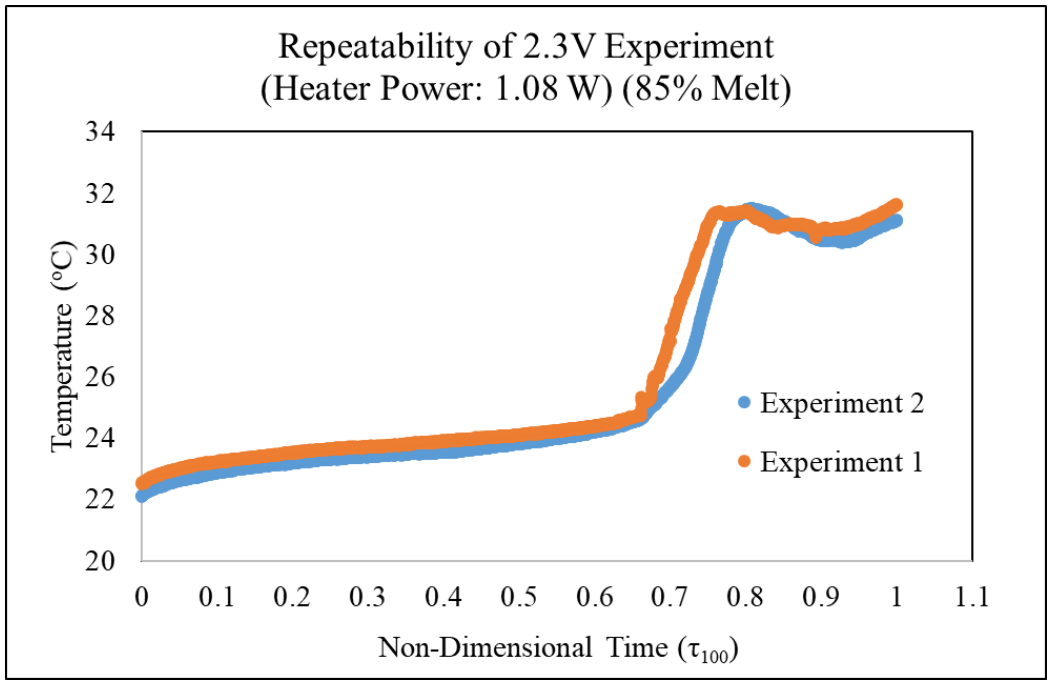

Figure 47. Temperature profile comparison for T_{85} for two experiments with a heater voltage of 2.3 V.

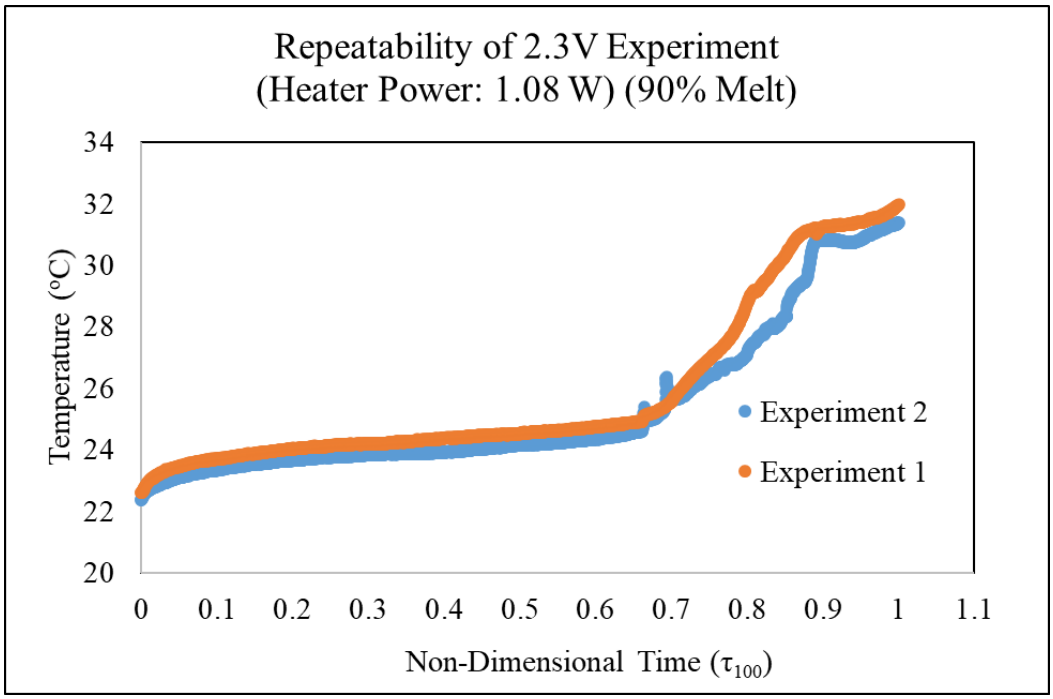

Figure 48. Temperature profile comparison for T_{90} for two experiments with a heater voltage of 2.3 V.

APPENDIX D

SCATTER PLOTS: PREDICTING TIME TO REACH 90% MELT FROM T_{30}, T_{60}, T_{85}

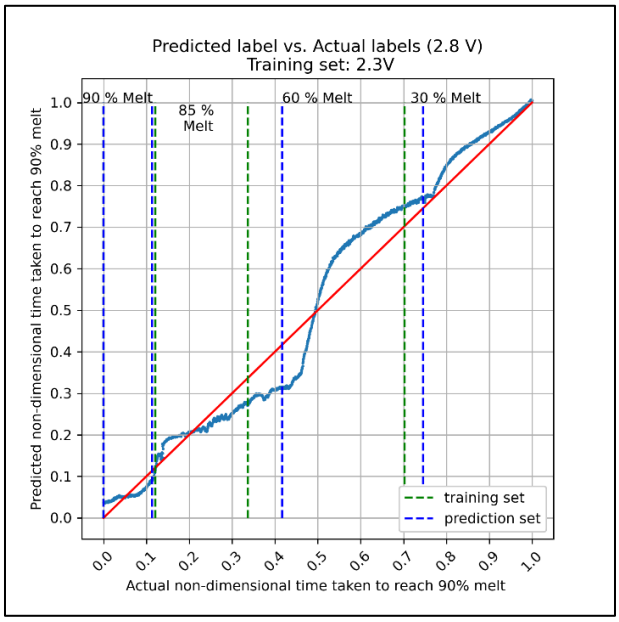

Figure 49. Scatter plot comparing the ANN predictions with experimental data (the actual values for τ') for test data set of 2.8 V (and training data set of 2.3 V.

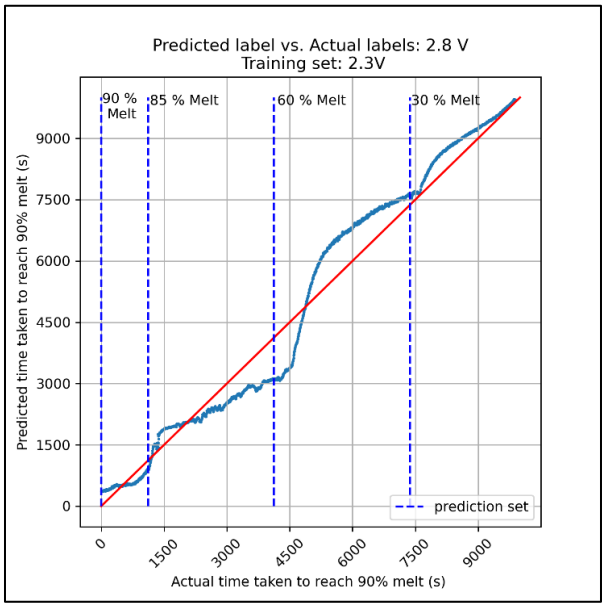

Figure 50. Scatter plot comparing the ANN predictions with experimental data for test data set of 2.8 V (and training data set of 2.3 V).

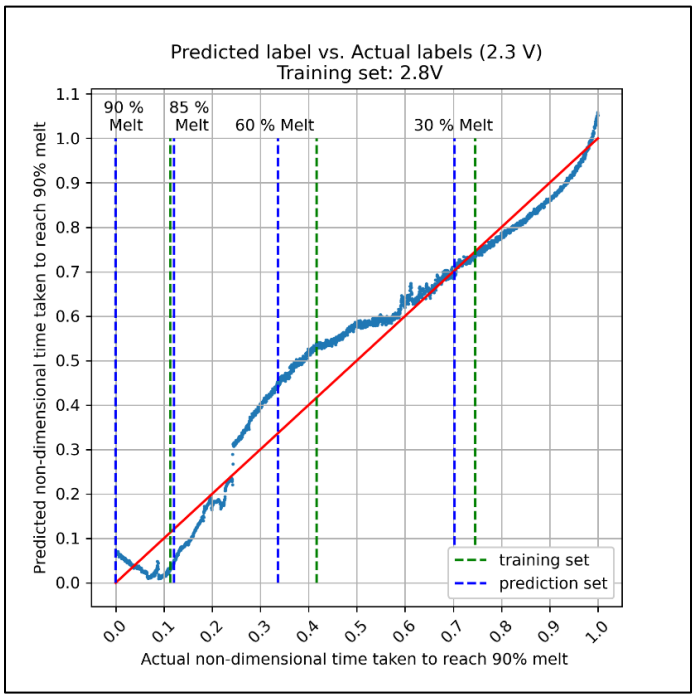

Figure 51. Scatter plot comparing the ANN predictions with experimental data (the actual values for τ') for test data set of 2.3 V (and training data set of 2.8 V).

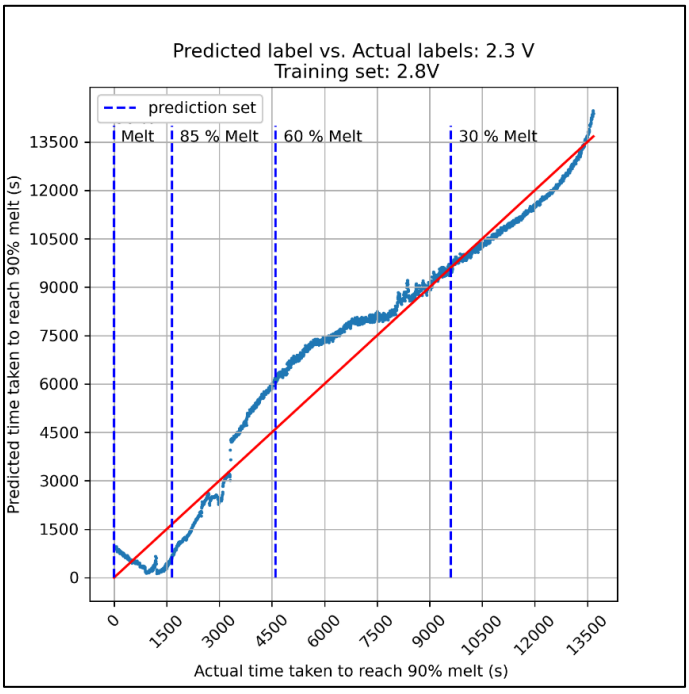

Figure 52. Scatter plot comparing the ANN predictions with experimental data for test data set of 2.3 V (and training data set of 2.8 V).

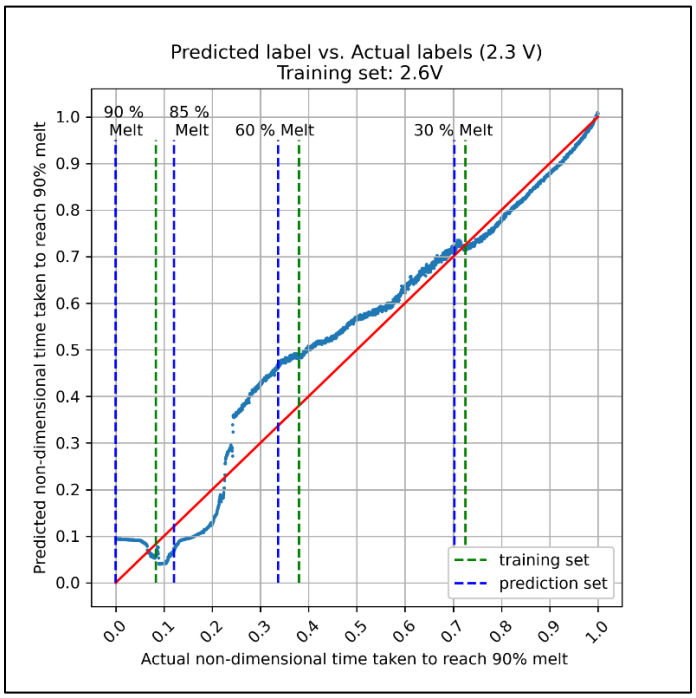

Figure 53. Scatter plot comparing the ANN predictions with experimental data (the actual values for τ') for test data set of 2.3 V (and training data set of 2.6 V).

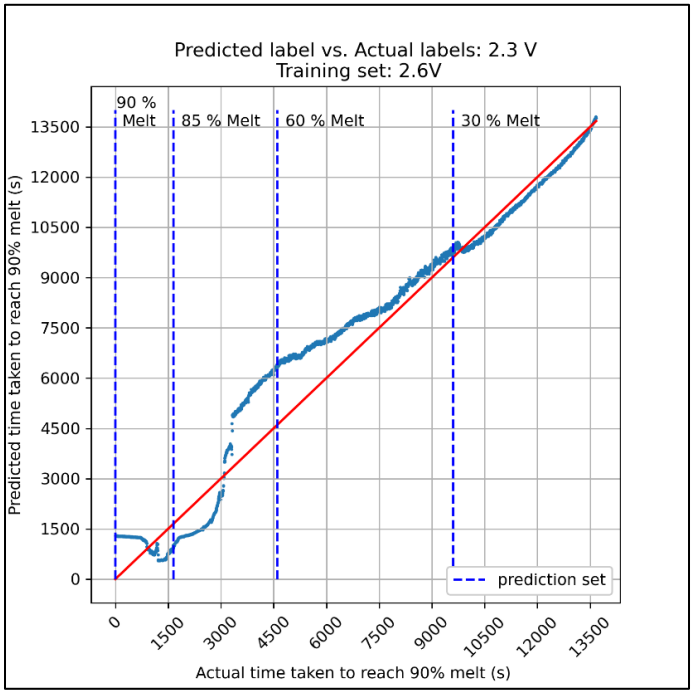

Figure 54. Scatter plot comparing the ANN predictions with experimental data for test data set of 2.3 V (and training data set of 2.6 V).

APPENDIX E

PREDICTING TIME TO REACH 90% MELT FROM T'_{30}, T'_{60}, T'_{90}

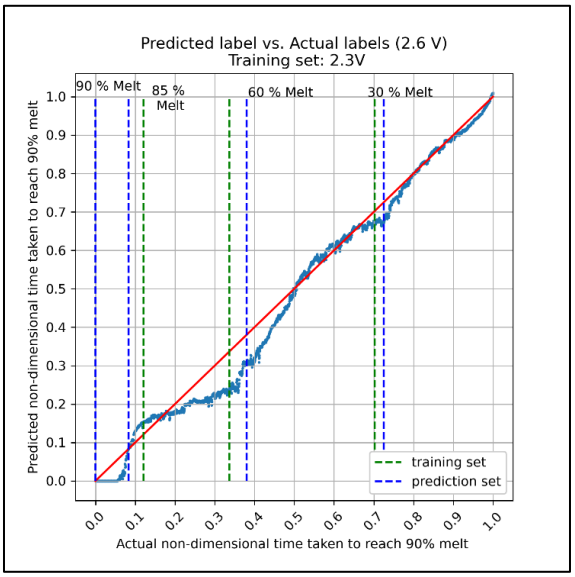

Figure 55. Scatter plot comparing the ANN predictions (from T'_{30}, T'_{60}, T'_{90}) with experimental data (the actual values for τ') for test data set of 2.6 V (and training data set of 2.3 V).

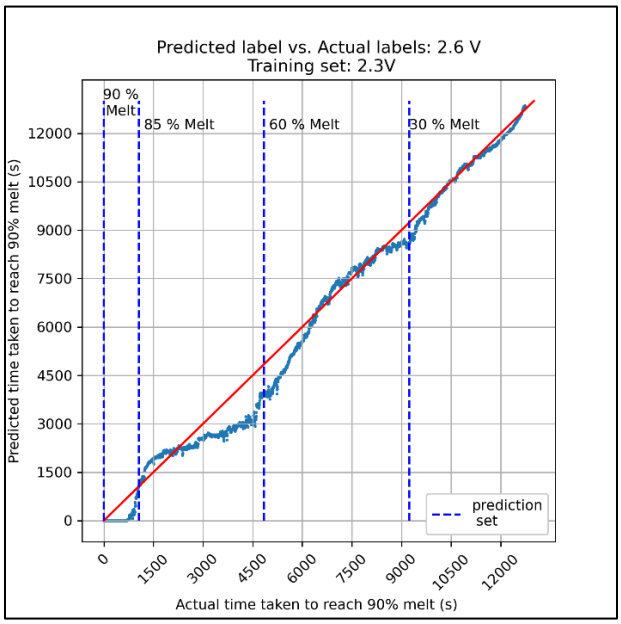

Figure 56. Scatter plot comparing the ANN predictions (from T'_{30}, T'_{60}, T'_{90}) with experimental data for test data set of 2.6 V (and training data set of 2.3 V).

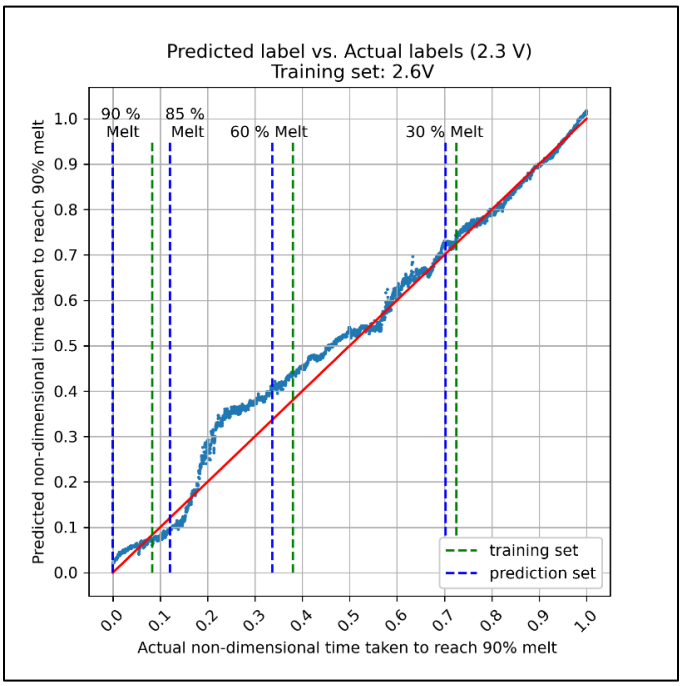

Figure 57. Scatter plot comparing the ANN predictions (from T'_{30}, T'_{60}, T'_{90}) with experimental data (the actual values for τ') for test data set of 2.3 V (and training data set of 2.6 V).

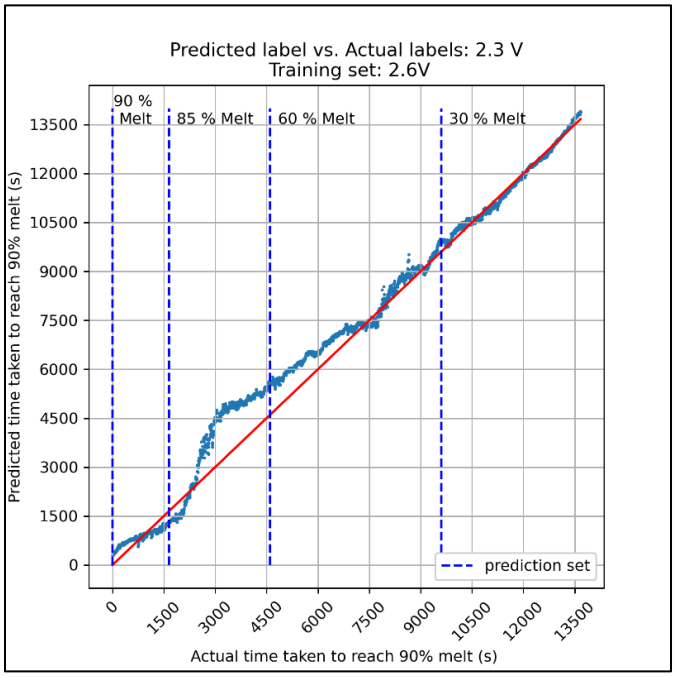

Figure 58. Scatter plot comparing the ANN predictions (from T'_{30}, T'_{60}, T'_{90}) with experimental data for test data set of 2.3 V (and training data set of 2.6 V).

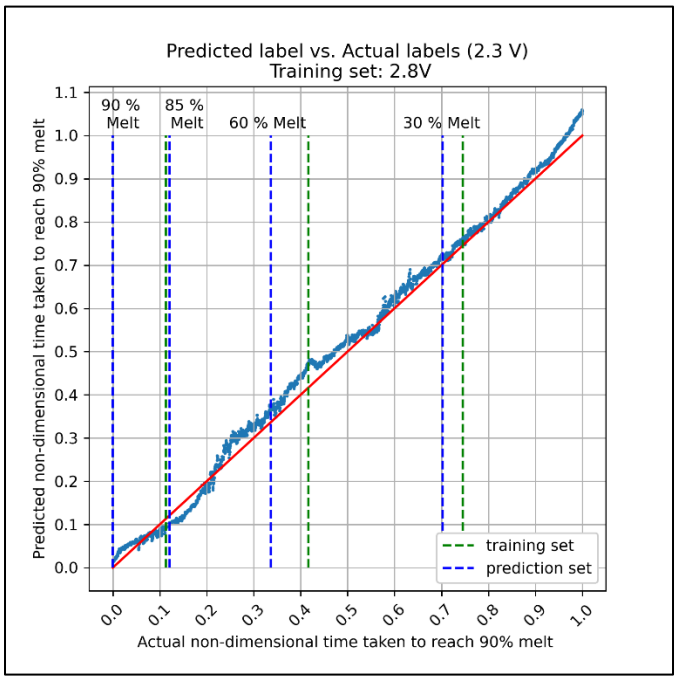

Figure 59. Scatter plot comparing the ANN predictions (from T'_{30}, T'_{60}, T'_{90}) with experimental data (the actual values for τ') for test data set of 2.3 V (and training data set of 2.8 V).

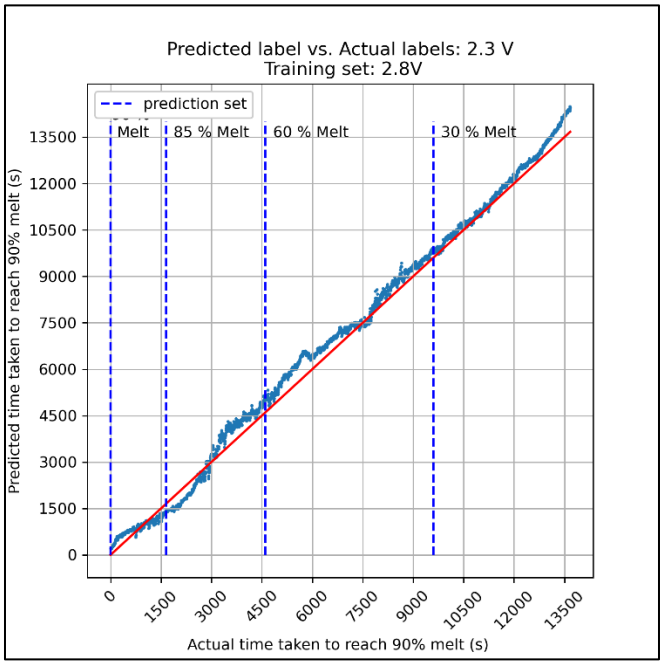

Figure 60 Scatter plot comparing the ANN predictions (from T'_{30}, T'_{60}, T'_{90}) with experimental data for test data set of 2.3 V (and training data set of 2.8 V)

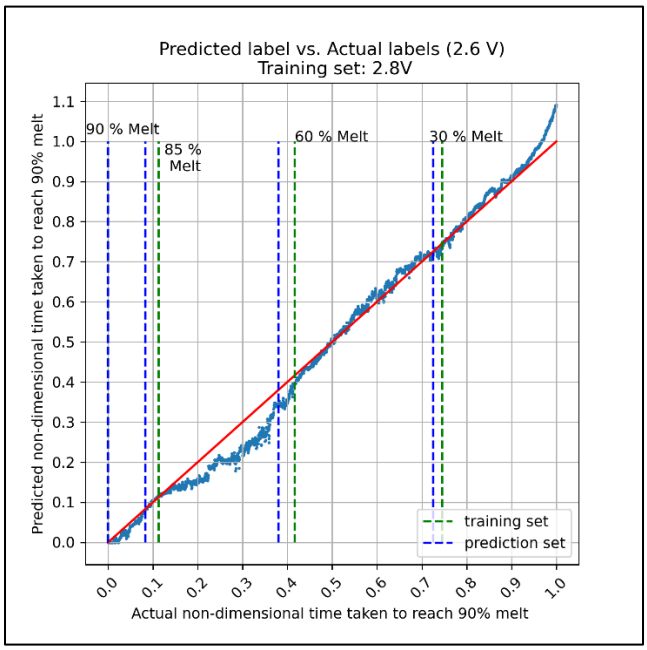

Figure 61 Scatter plot comparing the ANN predictions (from T'_{30}, T'_{60}, T'_{90}) with experimental data (the actual values for τ') for test data set of 2.6 V (and training data set of 2.8 V)

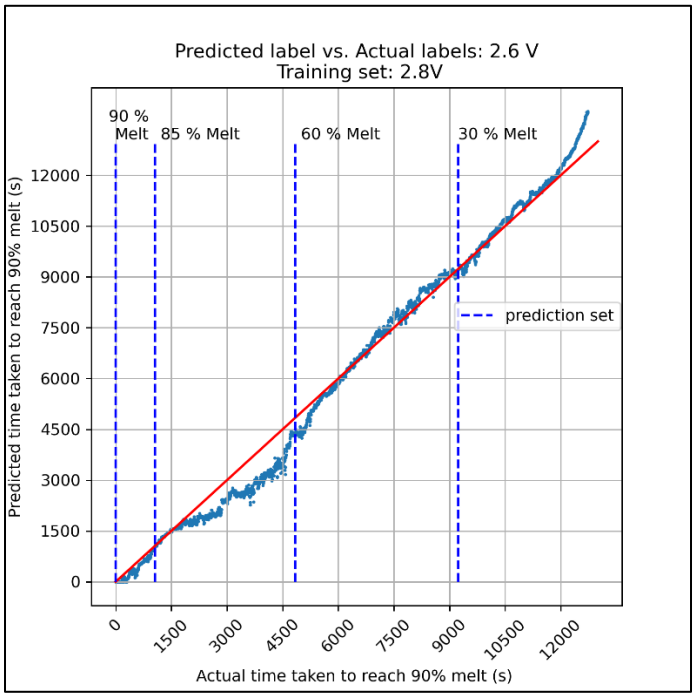

Figure 62 Scatter plot comparing the ANN predictions (from T'_{30}, T'_{60}, T'_{90}) with experimental data for test data set of 2.6 V (and training data set of 2.8 V)

APPENDIX F

SURFACE V/S PCM TEMPERATURES: PREDICTING TIME TO REACH 85% MELT FROM [T'_{30}, T'_{60}, T'_{90}] AND [T_{30}, T_{60}, T_{90}]

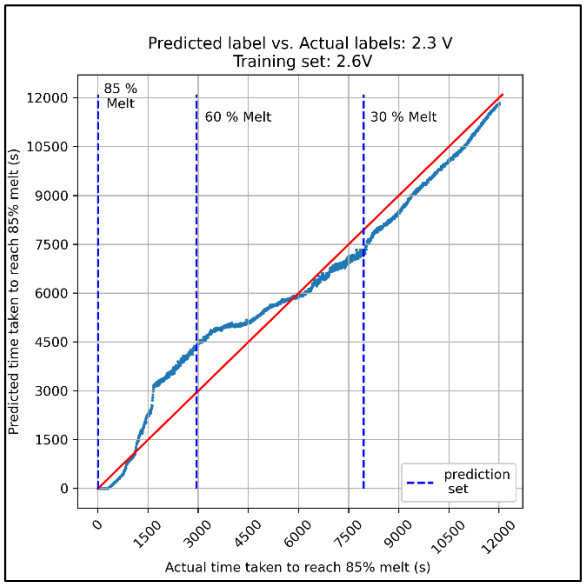

Figure 63. Scatter plot comparing the ANN predictions for time to reach 85% melt-fraction (from T'_{30}, T'_{60}, T'_{90}) for test data set of 2.3 V (training data set of 2.6 V)

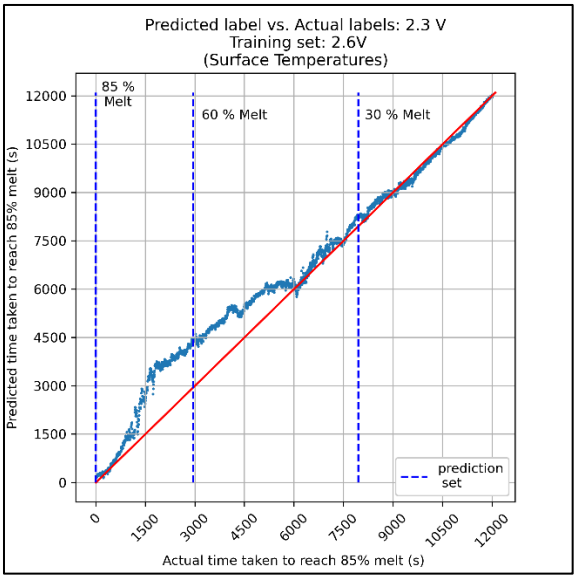

Figure 64. Scatter plot comparing the ANN predictions for time to reach 85% melt-fraction (from T'_{30}, T'_{60}, T'_{90}) for test data set of 2.3 V (training data set: 2.6 V).

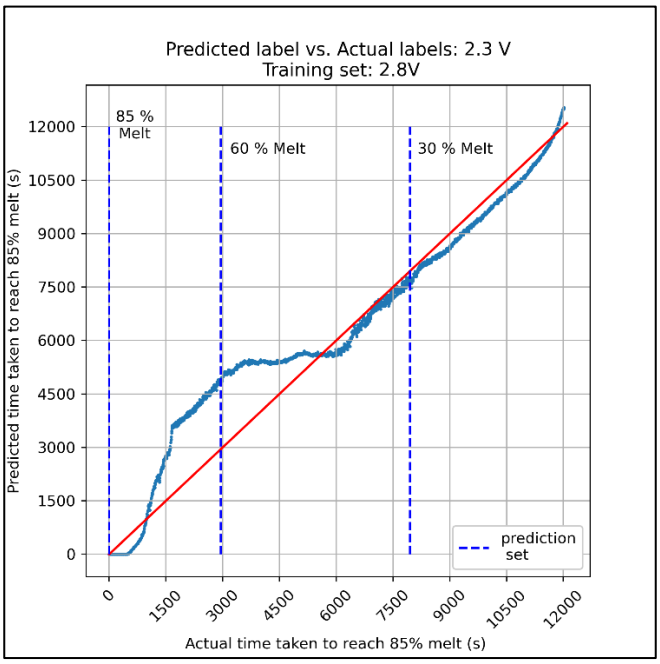

Figure 65 Scatter plot comparing the ANN predictions for time to reach 85% melt-fraction (from T'_{30}, T'_{60}, T'_{90}) for test data set of 2.3 V (training data set: 2.8 V).

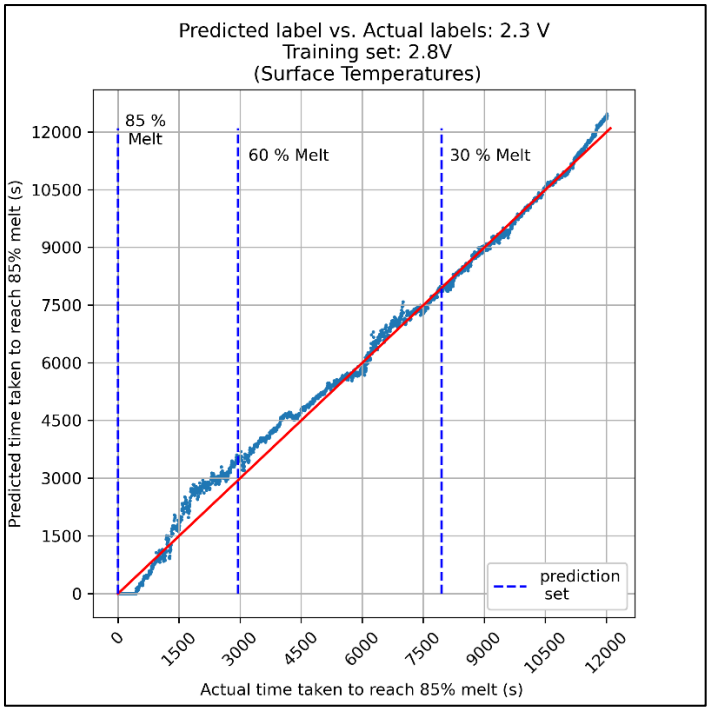

Figure 66 Scatter plot comparing the ANN predictions for time to reach 85% melt-fraction (from T'_{30}, T'_{60}, T'_{90}) for test data set of 2.3 V (training data set: 2.8 V).

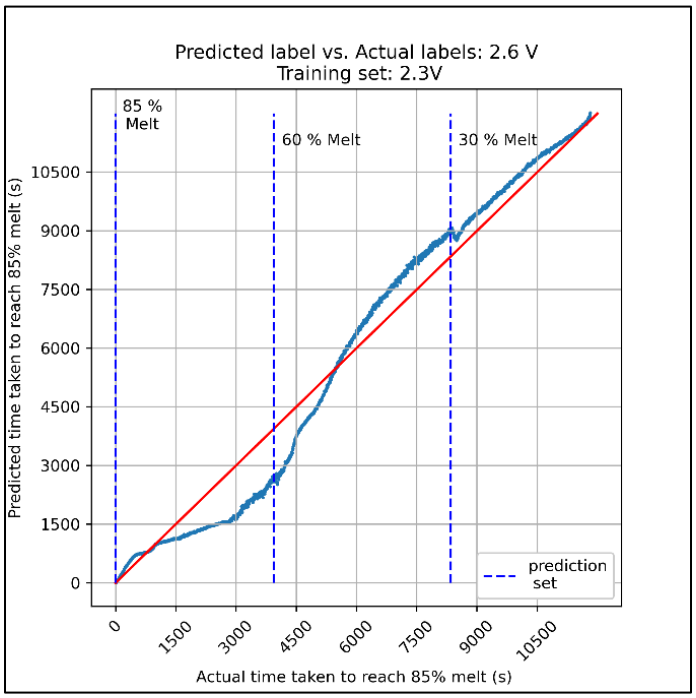

Figure 67. Scatter plot comparing the ANN predictions for time to reach 85% melt-fraction (from T'_{30}, T'_{60}, T'_{90}) for test data set of 2.6 V (training data set of 2.3 V).

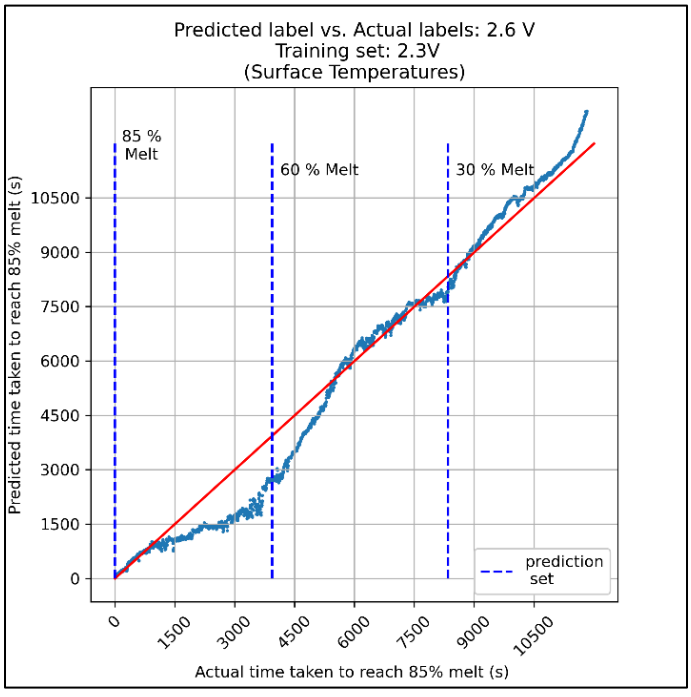

Figure 68. Scatter plot comparing the ANN predictions for time to reach 85% melt-fraction (from T'_{30}, T'_{60}, T'_{90}) for test data set of 2.6 V (training data set: 2.3 V).

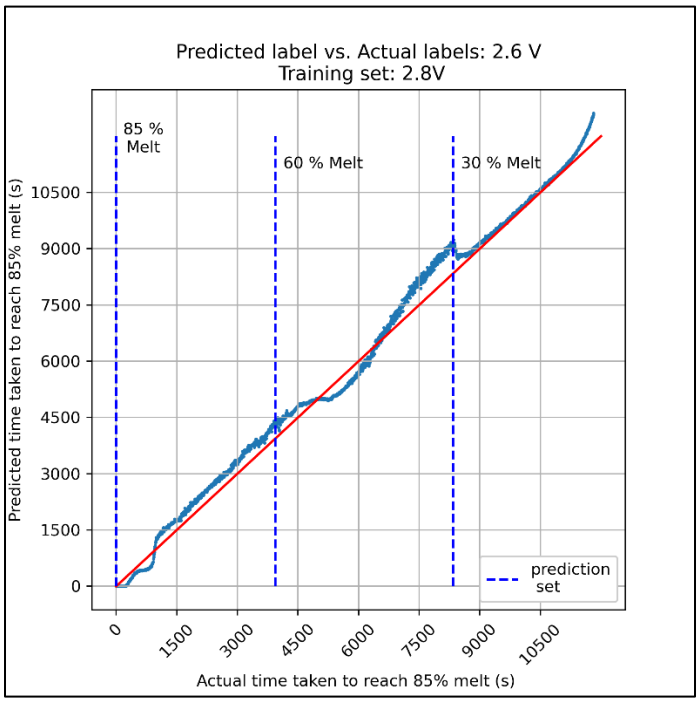

Figure 69. Scatter plot comparing the ANN predictions for time to reach 85% melt-fraction (from T'_{30}, T'_{60}, T'_{90}) for test data set of 2.6 V (training data set of 2.8 V).

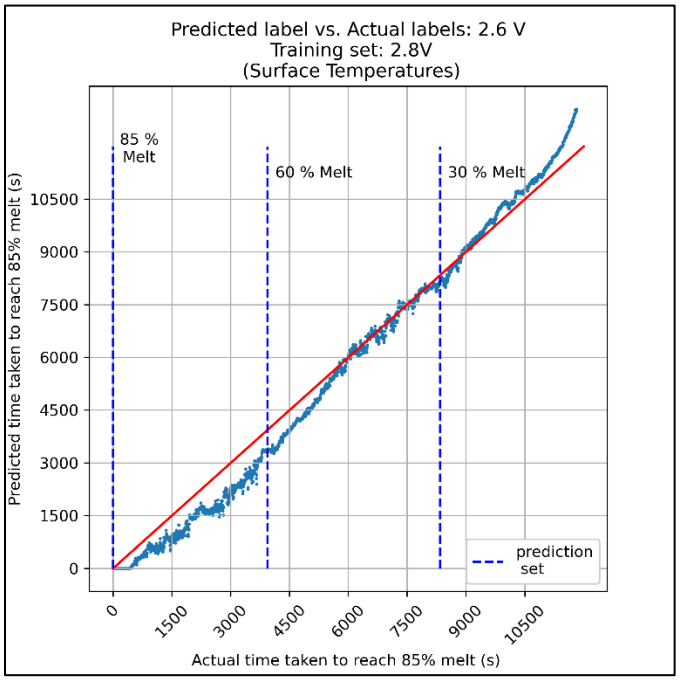

Figure 70. Scatter plot comparing the ANN predictions for time to reach 85% melt-fraction (from T'_{30}, T'_{60}, T'_{90}) for test data set of 2.6 V (training data set: 2.8 V).

APPENDIX G

INFRA-RED IMAGES CAPTURED DURING EXPERIMENTS

I.R. Images captured for 2.6 V (1.4 W input power) experiments at specified times

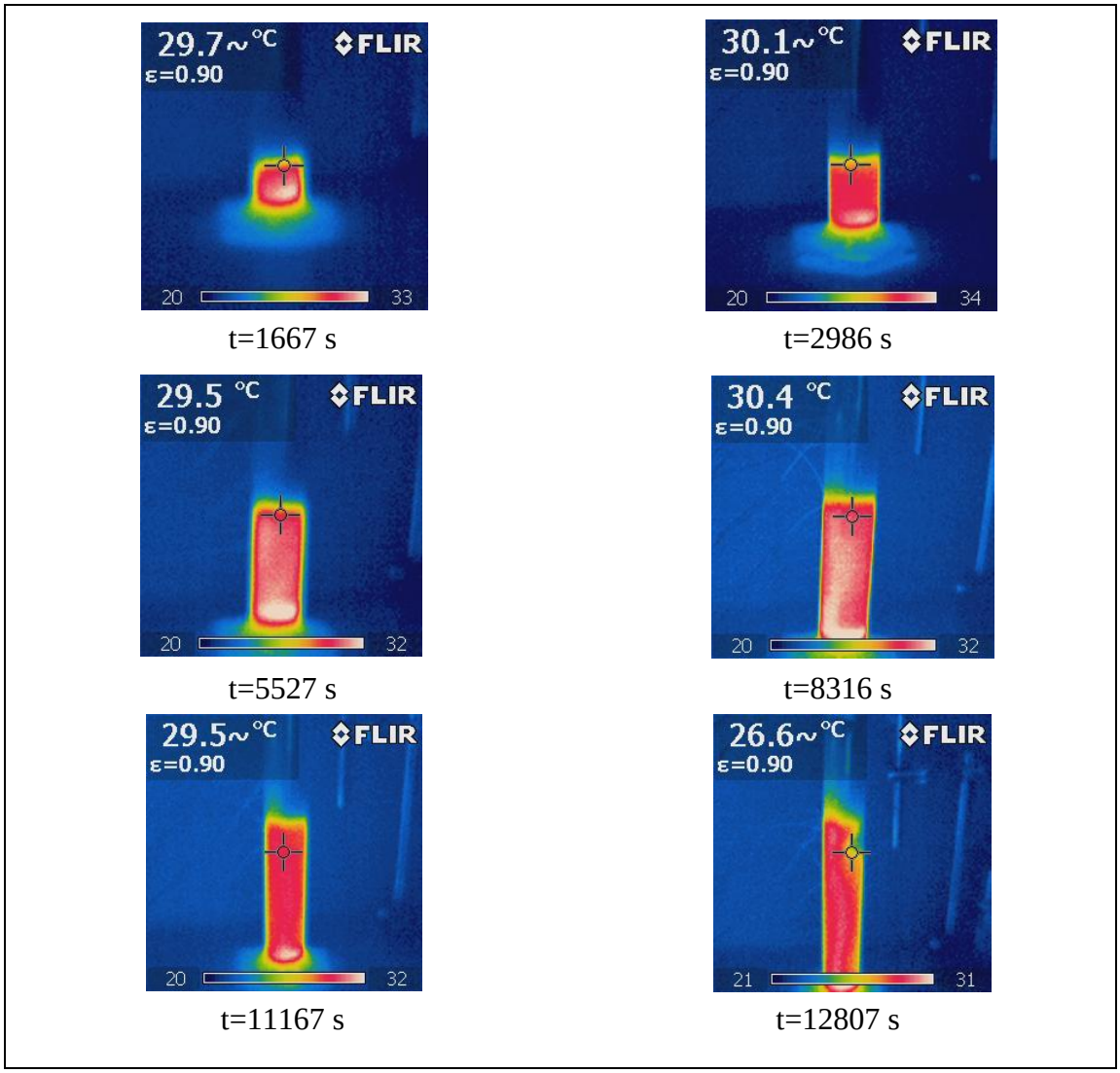

Figure 71. I.R. Images captured during 2.6V (1.4 W) experiment.

I.R. Images captured for 2.3 V (1.08 W input power) experiment at specified times

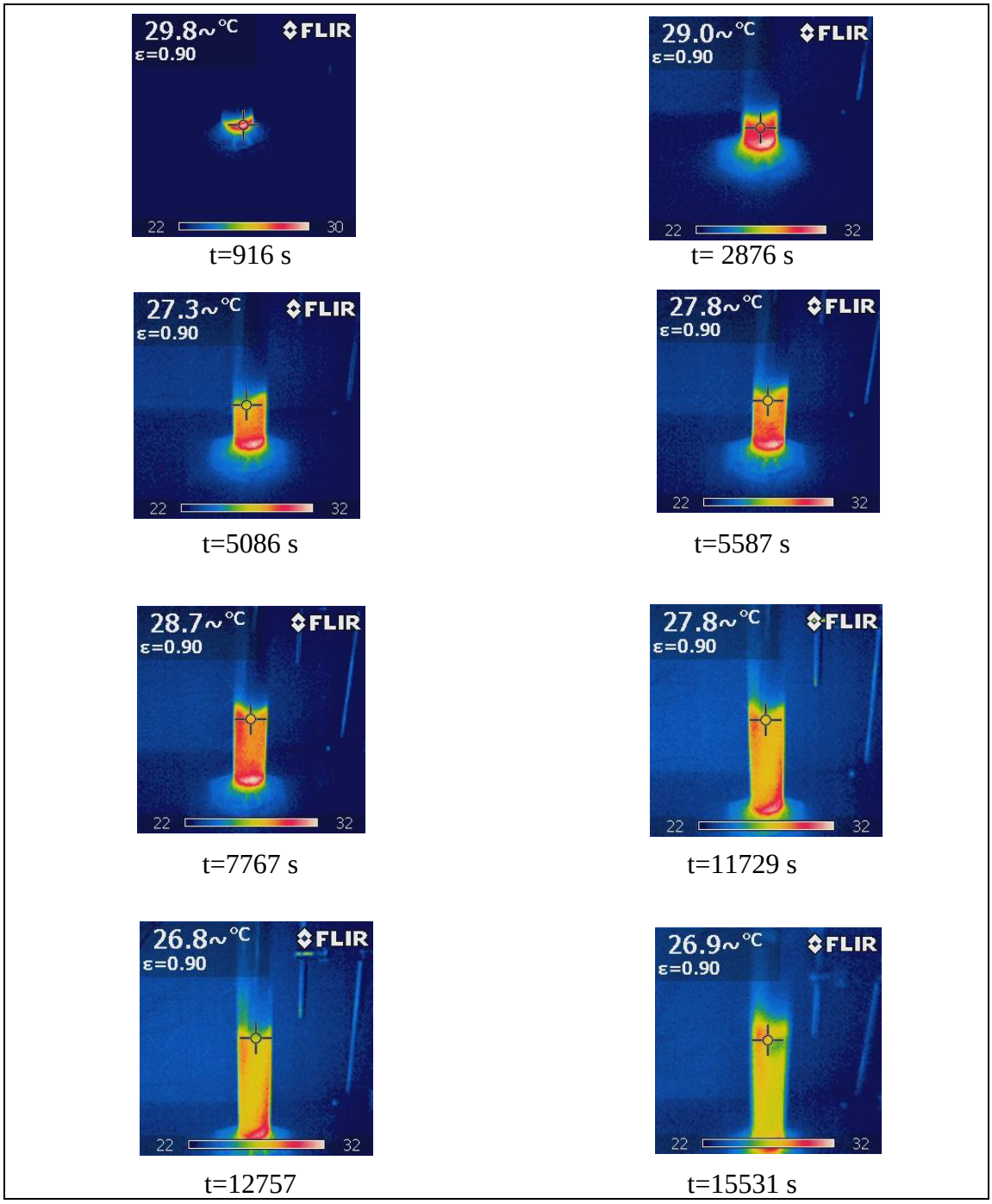

Figure 72. IR Images captured during 2.3V (1.08 W) experiments.

I.R. Images captured for 2.8 V (1.6 W input power) experiments at specified times

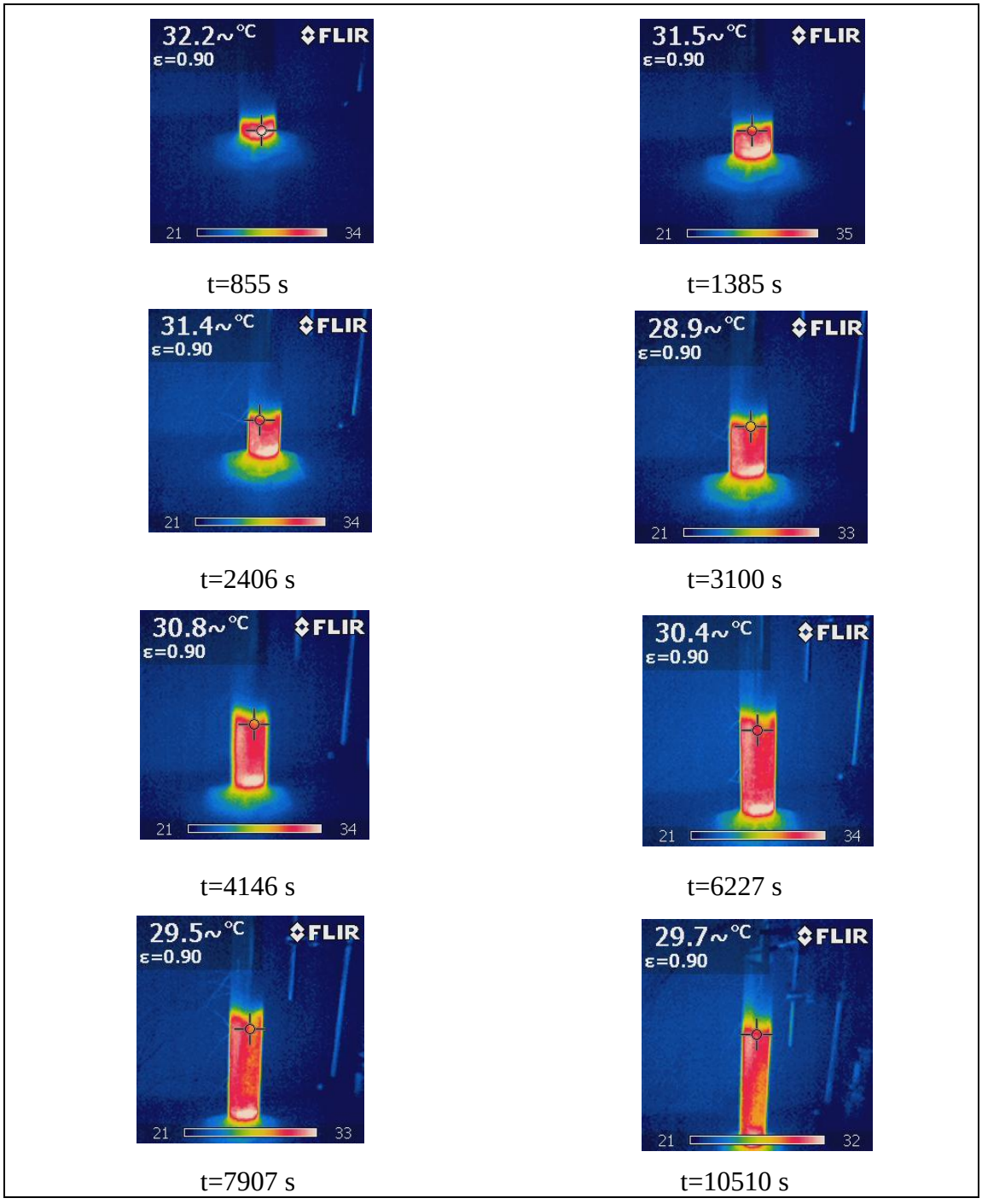

Figure 73. IR Images captured during 2.8V (1.6 W) heater input experiment

APPENDIX H

TEMPERATURE TRANSIENTS FOR DIFFERENT HEATER INPUT VOLTAGES

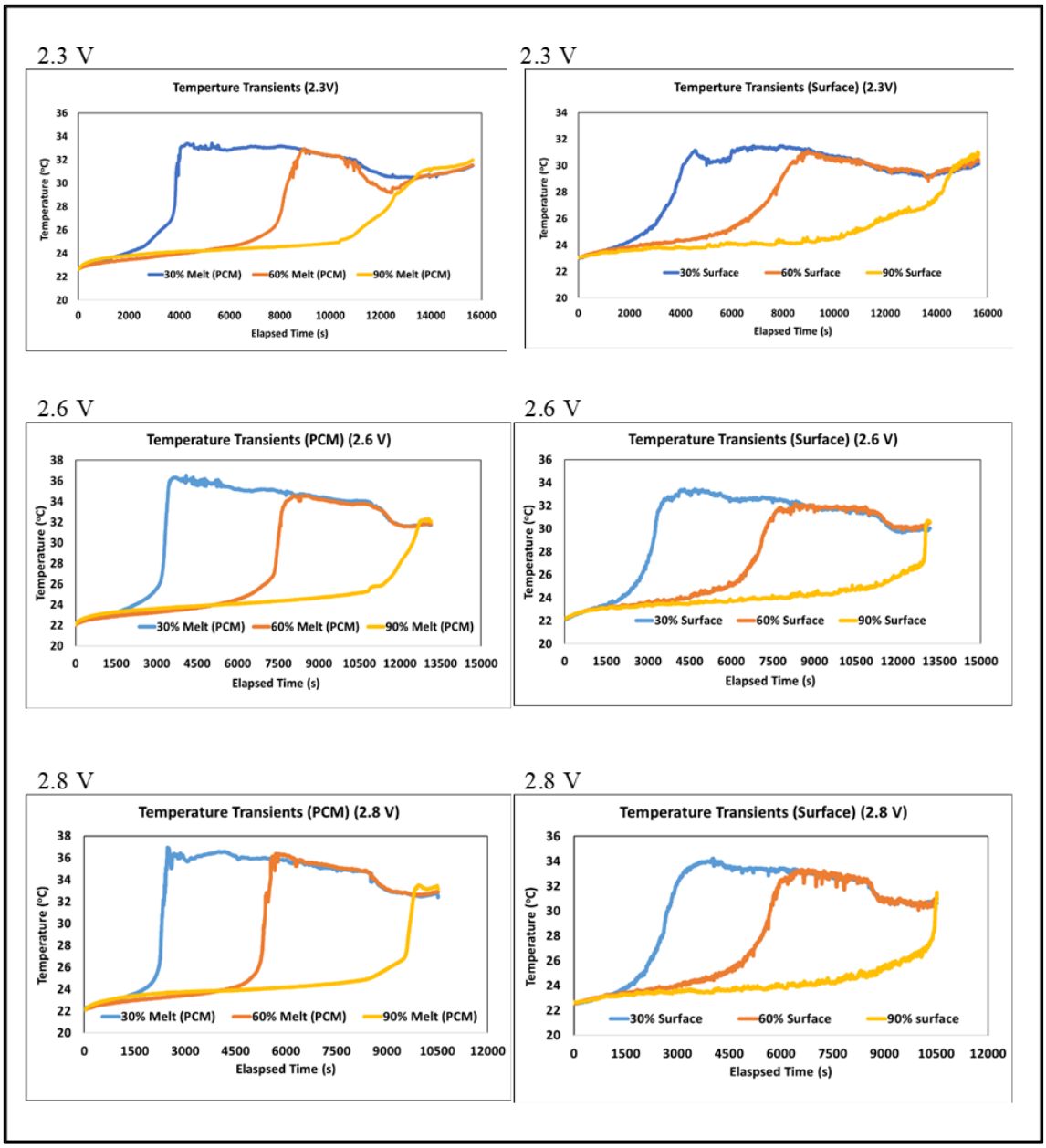

Figure 74. Plots of transient PCM-temperature data and transient surface-temperature data for different heater input voltage (and power input) conditions recorded in the experiments.

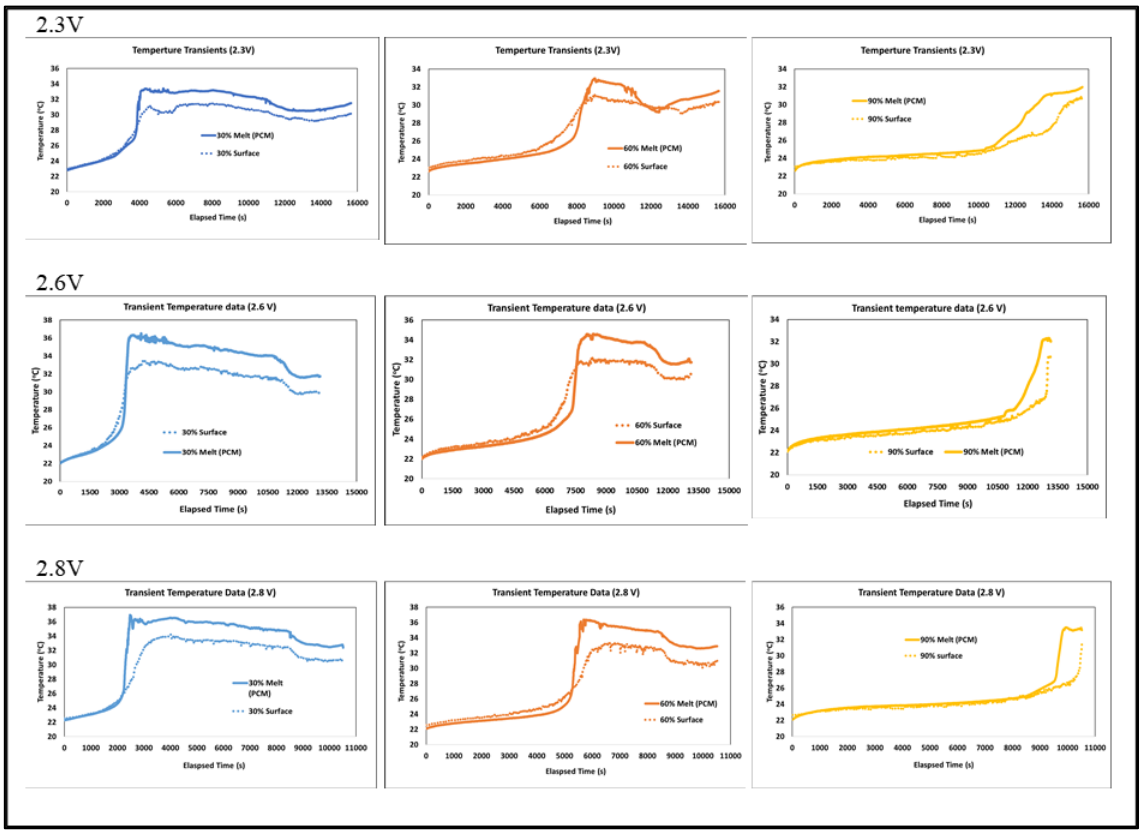

Figure 75. Comparison of the transient PCM-temperature data and transient surface-temperature data for different heater input voltage (power input) conditions recorded in the experiments.

APPENDIX I

ARTICLES PUBLISHED/ UNDER REVIEW

The author declares that the following articles are a result of the research conducted as a part of this this work.

- Chuttar, A., and Banerjee, D., “Machine Learning (ML) Based Thermal Management for Cooling of Electronics Chips by Utilizing Thermal Energy Storage (TES) in Packaging That Leverages Phase Change Materials (PCM).” *Electronics*. 2021; 10(22):2785. https://doi.org/10.3390/electronics10222785.
- Chuttar, A., Thyagarajan, A., and Banerjee, D. (May 31, 2021). "Leveraging Machine Learning (Artificial Neural Networks) for Enhancing Performance and Reliability of Thermal Energy Storage Platforms Utilizing Phase Change Materials." ASME. *J. Energy Resour. Technol*. February 2022; 144(2): 022001. https://doi.org/10.1115/1.4051048
- A. Chuttar, N. Shettigar, A. Thyagrajan and D. Banerjee, "Deep Learning to Enhance Transient Thermal Performance and Real-Time Control of an Energy Storage (TES) Platform," *2021 20th IEEE Intersociety Conference on Thermal and Thermomechanical Phenomena in Electronic Systems (ITherm)*, 2021, pp. 1036-1044, doi: 10.1109/ITherm51669.2021.9503247. *(Results in Appendix J)*
- G. Ren, A. Chuttar, and D. Banerjee, “Exploring Efficacy of Machine Learning/ ML (Artificial Neural Networks/ ANN) for Enhancing Reliability of Thermal Energy Storage (TES) Platforms Utilizing Phase Change Materials (PCM)” (2021) (Under Review) *(Results in Appendix K)*

APPENDIX J

RESULTS FROM A PUBLISHED WORK*

A. Chuttar, N. Shettigar, A. Thyagrajan and D. Banerjee, "Deep Learning to Enhance Transient Thermal Performance and Real-Time Control of an Energy Storage (TES) Platform," ***2021 20th IEEE Intersociety Conference on Thermal and Thermomechanical Phenomena in Electronic Systems (iTherm)*****, 2021, pp. 1036-1044, doi: 10.1109/ITherm51669.2021.9503247.**

Experimental Apparatus and Procedure

PCM Melting Experiments

In order to implement an ANN based algorithm for the prediction of time to reach a predefined melt fraction (e.g., a melt fraction of 90%), PCM melting experiments were conducted in this study. The data obtained from these experiments is used for training a neural network. PCM is melted in a graduated cylinder of volume 50 ml and a least count of 1 ml. The experimental apparatus is composed of three parts: (1) The heater assembly, (2) thermocouples mounted on a 3D printed plastic jig (for measuring temperature transients at specific vertical heights along the axis of the cylinder within the mass of PCM), and (3) a data acquisition apparatus (consisting of a digital image acquisition apparatus at specific intervals in time and a digital data acquisition apparatus for recording the temperatures from the thermocouples at specific intervals in time).

The heater assembly consists of a Nichrome wire (coil) connected to a DC power supply. The coil is placed at the bottom of the cylinder. Insulated wires were used to connect the ends of the coil to the terminals of the DC power supply. Four T-type thermocouples were used to capture the temperature transients. The thermocouples were calibrated for the temperature range 20^{o} C to 40^{o} C. The errors in the measured temperatures were found to be less than 1%. The raw data are modified using the calibration constants prior to training the neural network. Three of the thermocouples are placed at specific locations within the cylinder corresponding to 40%, 65%, and 90% melt fraction. The fourth thermocouple records the ambient air temperature. Thermocouple data is recorded using LabView software with the help of a digital data acquisition apparatus (NI 9211 thermocouple input module, National Instruments Inc.). Fig. 1 shows an image of the experimental apparatus while Fig. 2 schematically depicts the components involved.

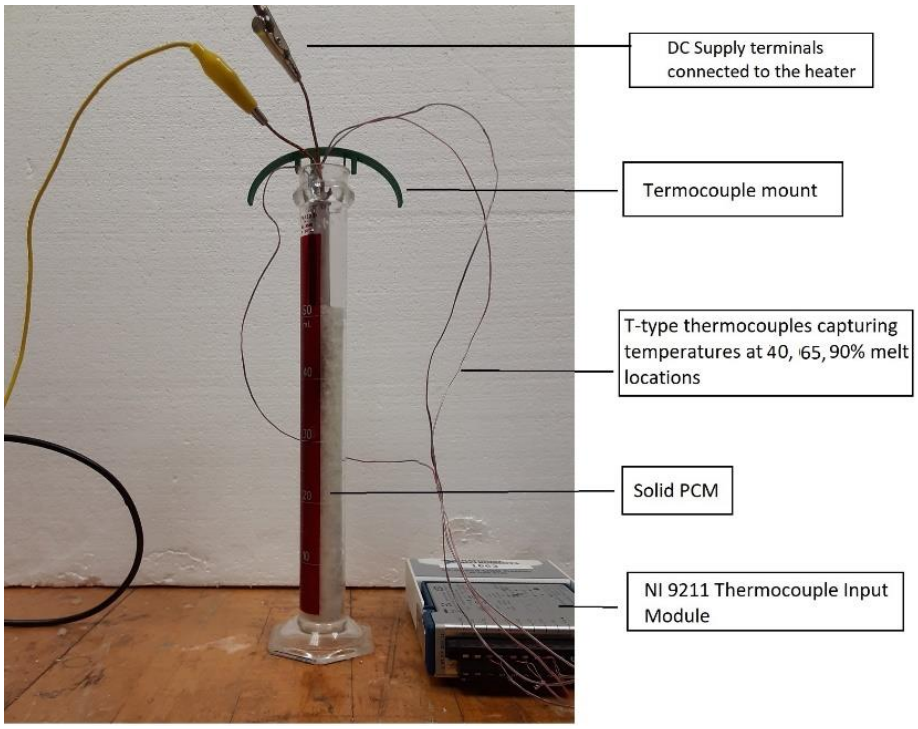

Fig. 1 Image of the experimental apparatus used in the study

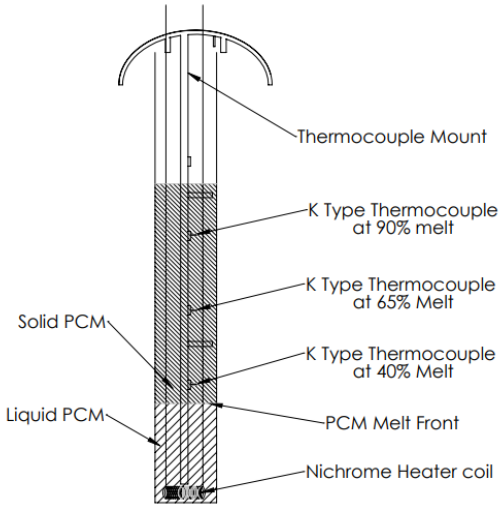

Fig. 2 Schematic of the experimental apparatus used in the study

A 3-D printed plastic jig is used to mount the thermocouple junctions at the desired specific locations in the cylinder and the cylinder is then filled with the desired mass of PCM. A digital camera is used to track the melting process throughout the duration of the experiment. Infrared images are captured intermittently to provide a visual representation of the temperature distribution in the PCM mass. Sample IR images are shown in Fig. 3.

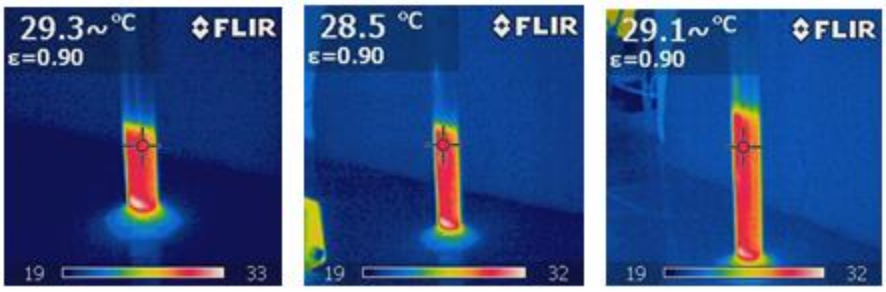

Fig. 3 IR Images of a PCM undergoing melting in a graduated cylinder

The PCM used was PureTemp29 with a melting point of 29^{o} C. Experimental datasets are generated using this apparatus by varying the voltage supplied to the heater. Datasets for heater voltages of 2.3V, 2.6V and 2.8V are considered in this study. The output of the experiment for heater voltage input of 2.3V is shown in Fig. 5. The

temperature transients for each thermocouple are represented in a line graph. T_1, T_2 and T_3, denote the temperatures recorded by thermocouples mounted at 40%, 65%, 90% melt locations, respectively. The temperature at a point increases gradually upon powering the heater. However, a progressive rise in temperature is observed when the melt front reaches a particular thermocouple. The temperature eventually reaches a constant value after the melt front has passed through this location. The slight drop in temperature from the peak to the end of the cycle can be attributed to heat losses through the glass cylinder. These losses increase as the experiment progresses since the surface area of the glass in contact melted PCM increases with time. The ambient temperature is also shown in this plot. The abscissa (x-axis) denotes the elapsed time.

Data Preparation and ANN Training

To reiterate, the aim is to predict the time remaining to attain an 90% melt fraction at any moment during the melting process. In Deep Learning terms, the time to reach 90% melt, is the label for our purpose. This label is obtained by subtracting the time recorded by the data acquisition from the time when the preselected melt of 90% is attained (i.e., 90% melt is achieved when the melt front hits the third thermocouple). This occurs when the temperature profile of T_3 flattens after a sharp increase. The time stamp on this point serves our purpose for generating the labels. A Multilayer Perceptron (MLP) Network is devised with three input nodes. The topology of the network is depicted in Fig. 4.

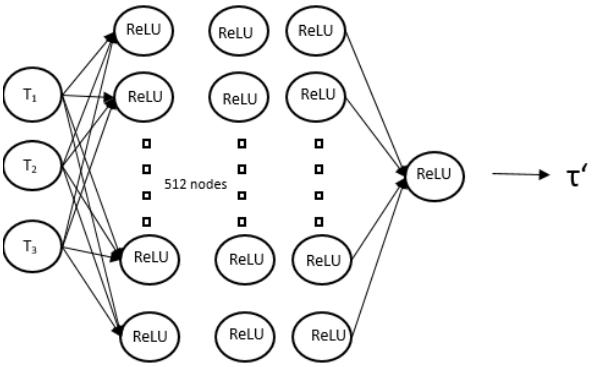

Fig. 4 Topology of the MLP network

T_1, T_2 and T_3, constitute the three inputs for the MLP network. Instead of using an absolute value of time, a nondimensional quantity, referred to as reduced time, is formulated. Nondimensionalizing time allows us to train the ANN using one experimental dataset and predict for another one. This reduced time, τ, is obtained by taking the ratio of the elapsed time to the time when a 90% melt is achieved. It follows that the nondimensional form of the label is unity minus τ and is denoted by τ'. Fig. 6 depicts the plot of temperature as a function of nondimensional time (τ) and was obtained after the implementing following the steps (summarized in this paragraph).

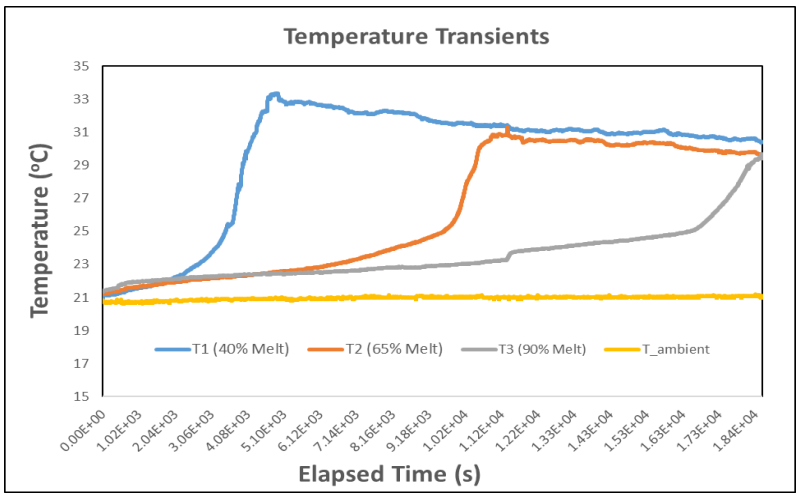

Fig. 5 Temperature Transients recorded from the three thermocouples mounted within the graduated cylinder for a heater voltage of 2.3 V.

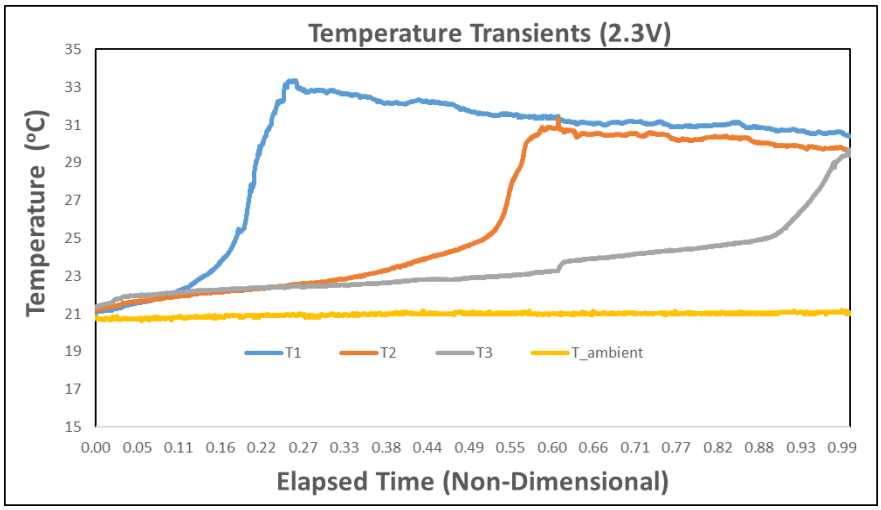

Fig. 6 Temperature Transients from the three thermocouples mounted within the graduated cylinder for a heater voltage of 2.3 V, plotted against the non-dimensional time (τ)

The three inputs are: T_1, T_2, and T_3. The output of the ANN is τ'. Using this output as the label and the three temperature inputs, a neural network is trained. The training process is based on the well-known backpropagation algorithm which modifies the weights and biases of a node as it iterates through the dataset [12]. ADAM optimizer is used in the ANN for this study [13]. The salient parameters of the optimizer are tabulated in Table 1. The neural network is composed of three hidden layers and each layer has 512 nodes each. The Rectified Linear Unit (ReLU) activation function is used for the nodes. The cost function for the training purpose is the Mean Squared Error (MSE). The predictions are generated for all the six combinations of training/prediction with the three datasets.

Table 1 Hyperparameters of the ADAM Optimizer

Parameter	Value
α (learning rate)	0.001
β_1	0.9
β_2	0.999
ε	10^{-7}

To test the robustness of the technique implemented in this study, this method was used to predict the time to attain 80% melt fraction. This target melt fraction cannot be deterministically evaluated as there is no thermocouple at that location. The time point at which 80% melt fraction is reached is determined from the location of the meniscus that are recorded in the digital images. If the meniscus level of the liquid PCM in the cylinder at 100% melt is 50 ml, the volume marking corresponding to 40 ml marks the 80% melt (this is after accounting for the volume occupied by the heater and the mount). Hence, when the PCM melt front is at 40 ml level, the PCM is said to have a melt fraction of 80%. The time interval between the images and the serial numbers of the sequence of the images are used to obtain the time corresponding to each image. The corresponding point in the temperature profile is thus identified. The procedure summarised in the previous paragraph is followed to obtain predictions for the time needed to reach 80% melt fraction. Two sets of experiments were performed for the heater voltage setting of 2.6 V (in order to verify the repeatability of the experiments). The repeatability of the experiments is evident from Fig. 7 and Fig. 8.

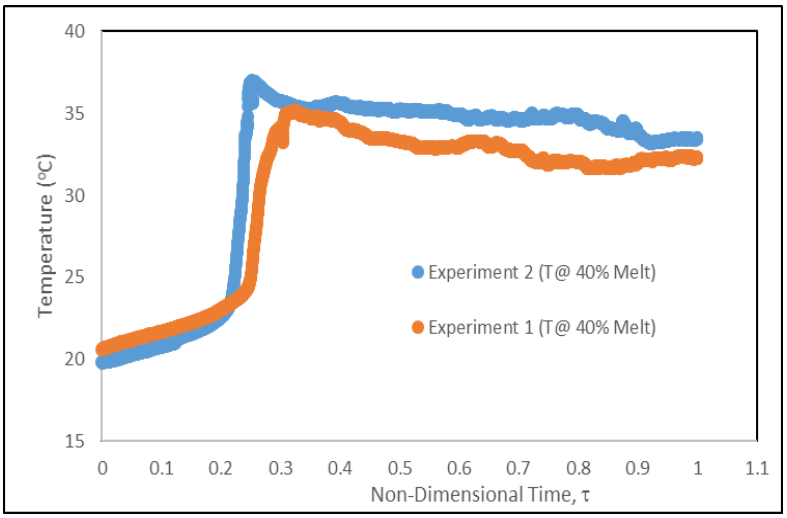

Fig. 7 Temperature profile comparison of two experiments for the 40% melt point with a heater voltage of 2.6V

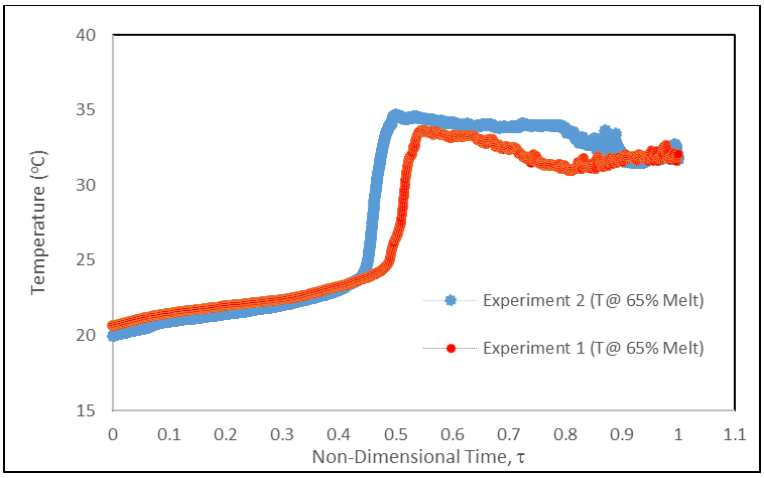

Fig. 8 Temperature profile comparison of two experiments for the 65% melt point with a heater voltage of 2.6V

The durations of the melting cycle for the two experiments differ by ~1800s (for a total nominal value of ~16,000 seconds (showing the experiments are repeatable to within ~90%). The slight variability within the two experiments is due to small variations in the ambient temperature conditions between the two sets of experiments. However, a temperature profile plotted against the non-dimensional time provides more succinct

evidence of the repeatability of the experiments implemented in this study. The plots obtained by using non-dimensional time show that instant when the melt front reaches each of these thermocouples is highly repeatable (i.e., when normalized for the total duration of each experiment). This is shown in Fig. 7 and 8. In addition, the experiments were repeated (Fig. 7 and Fig. 8) using both K-type thermocouples (Experiment 1) and T-type thermocouples (Experiment 2). The results show that the instant at which the melt front reaches a particular value of melt fraction (as recorded by either of these thermocouples) is highly repeatable (especially, when plotted as a function of the non-dimensional time).

Results and Discussion

Time Taken by PCM to Reach 90% Melt

The time duration to reach a percentage melt of 90% is depicted in Fig. 9 for the three sets under consideration. The number of points available for training an ANN are: 4640 (for 2.3 V experiments), 3025 (for 2.6 V experiments), and 2240 (for 2.8 V experiments). Subsequently, the time to reach a 90% melt for a dataset is predicted by using a neural network that was trained by using each of the other two datasets separately. For instance, a neural network trained on the 2.6 V data is deployed to make predictions on both 2.3V and 2.8V datasets. The predictions are depicted on a scatter plot. The solid red line (which is the y = x curve) is meant to serve as a reference for the deviations from the ideal. Both dimensional and non-dimensional plots are shown. The error is quantified by the difference between the predictions and actual values of time to reach 90% melt.

With the 2.6V data as the training set, the predictions on the 2.8V set are shown in Fig. 10 and Fig. 11. The error in predictions is plotted in Fig. 12.

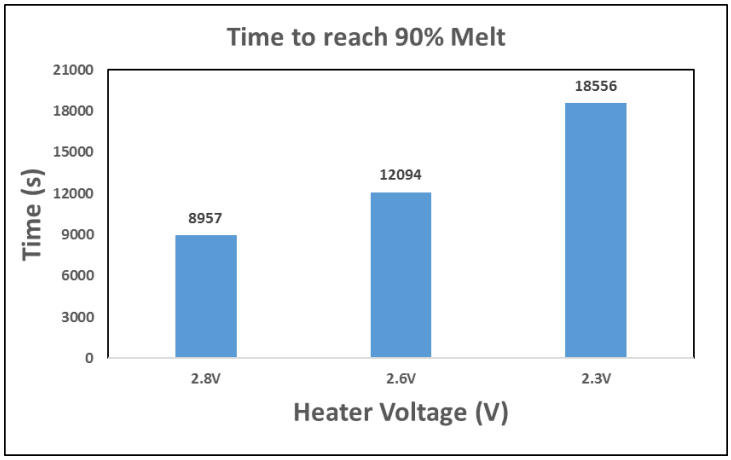

Fig. 9 Bar chart showing the time taken to attain an 90% melt for heater voltages 2.3V, 2.6V, and 2.8V

Figure 10 depicts the τ' predictions of the neural network which are shown in a dimensional form in Fig. 11. It can be appreciated that the neural network is able to predict the remaining time with considerable accuracy throughout melting cycle. The vertical dotted lines mark the time when the melt front reaches the thermocouples at 40, 65, and 90% melt respectively. The error in predictions, which is the difference between the predicted time and the actual time is plotted in Fig. 12. It is observed here that the error lower in the initial and final stages of the melt cycle. In fact, the average absolute error in the last half an hour of attaining 90% melt is 160 seconds. This means that we can predict the time remaining to reach the target melt apriori with an error of ~3 minutes. It is crucial that the error is low towards the end of the cycle in order to stop the heating cycle in time to implement the cold finger technique. The average error during last half an hour can thus be taken as a metric demonstrating the efficacy of this method.

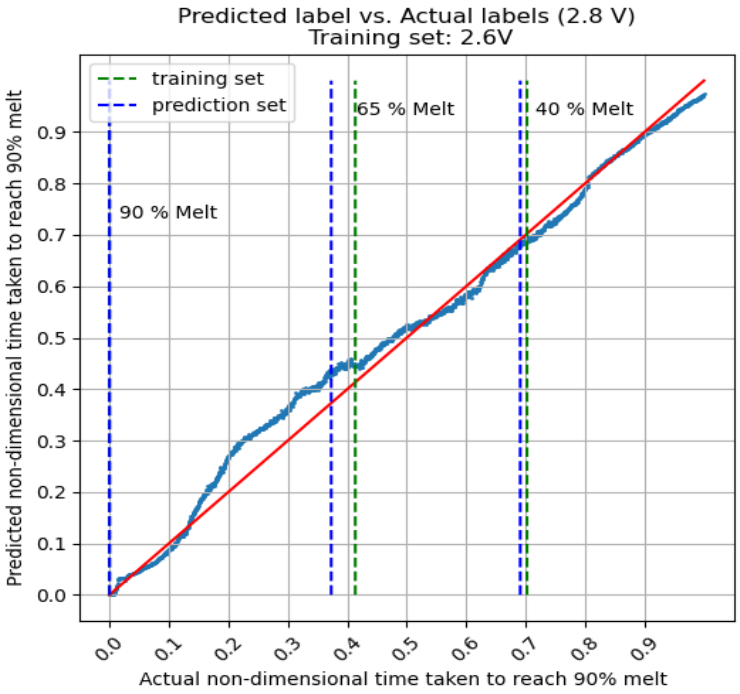

Fig. 10 Scatter plot of the ANN predictions as a function of the actual values for 2.8V data (Training set: 2.6 V).

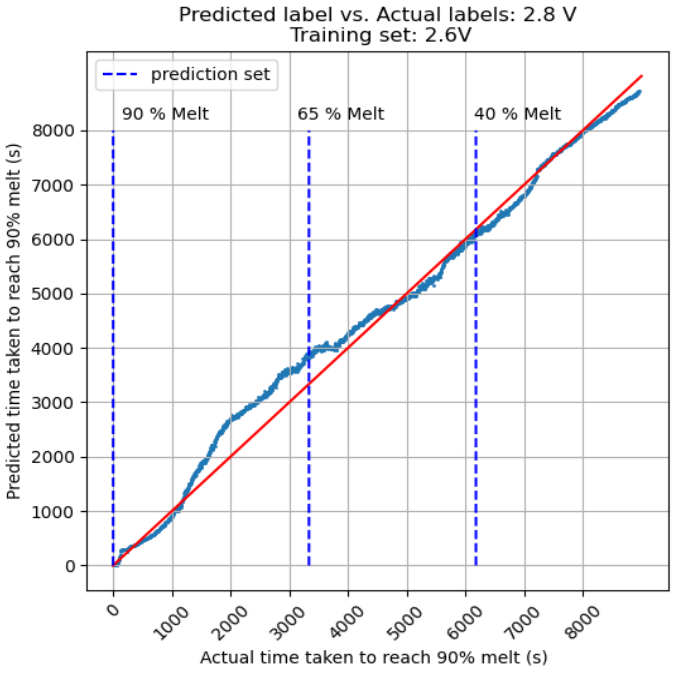

Fig 11 Scatter plot of the ANN predictions as a function of the actual values for 2.8V data (Training set: 2.6 V).

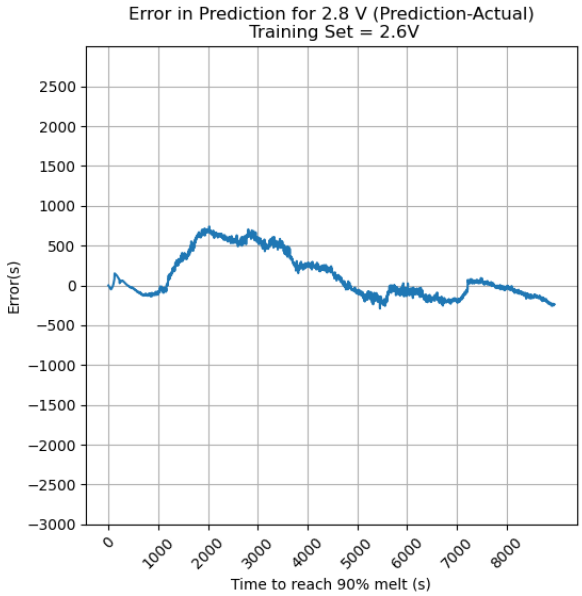

Fig. 12 Error in predictions for 2.8V dataset (Training set: 2.6V)

The ANN trained on 2.6V data (which corresponds to 1.72 W of power input and input current of 0.662 Amps) is further deployed to make predictions on the 2.3 V dataset (which corresponds to power input of 1.33 W and input current of 0.575 Amps). Additional experiments were performed for 2.8 V (which corresponds to 2 W of power input and input current of 0.72 Amps). Fig. 13 shows that a higher deviation occurs when the melt front is in the vicinity of a thermocouple. The deviation is lower in the later stages of the cycle with an average absolute error of 300 seconds in the final 30 minutes. Fig. 14 shows the error at all times in the cycle. An extreme training/prediction combination of 2.8V/2.3V, respectively, shows that the deviations are the greatest near the 40% and 65% melt fractions. However, the error decreases as the experiment progresses towards the 90% melt fraction. Table I shows this metric for all the six training/prediction combinations.

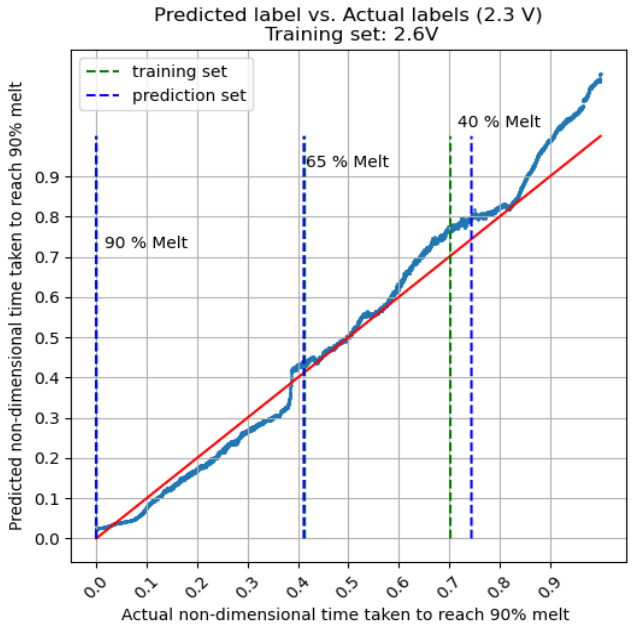

Fig. 13 Scatter plot comparing the ANN predictions with experimental data for test data set of 2.3 V (and training dataset of 2.6 V).

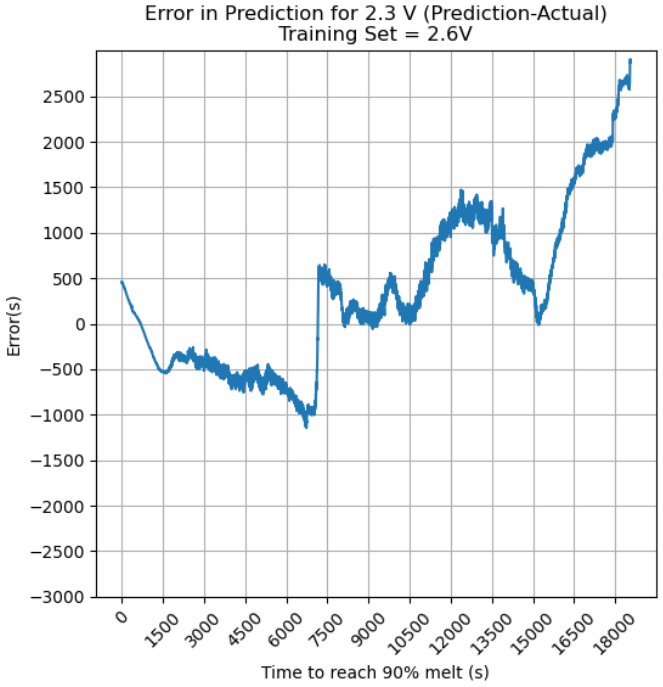

Fig. 14 Error in predictions for 2.3V dataset (Training set: 2.6V)

Table 2: Average absolute error in predictions during the last 1800 seconds before 90% melt (seconds)

		Training Set		
Prediction Set		***2.3V***	***2.6V***	***2.8V***
	2.3V		303.3	251.5
	2.6V	346.8		369.9
	2.8V	325.1	163.2	

Time Taken by the PCM to Reach 80% Melt

When predicting the value of time required for the PCM to reach 80% melt fraction, the 2.6 V and 2.8 V dataset pair yields substantially better results than any of the other combinations. The number of points available for training a neural network are 3806 (for 2.3 V experiments), 2356 (for 2.6 V experiments), and 1768 (for 2.8 V experiments). These results are plotted in Figs.15 - 18. Similar to Table 1, the average absolute error in the last half an hour before 80% melt fraction is achieved - is tabulated in Table 3. The error is of the order of 10 minutes for most combinations.

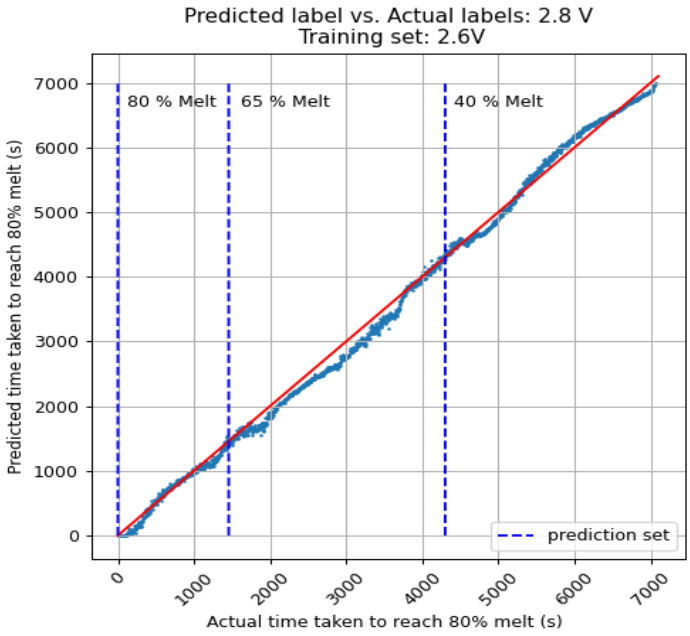

Fig 15 Scatter plot comparing the ANN predictions with experimental data for test data set of 2.8 V (and training dataset of 2.6 V)

Fig 16 Error in predictions for 2.6V dataset (Training set: 2.8V)

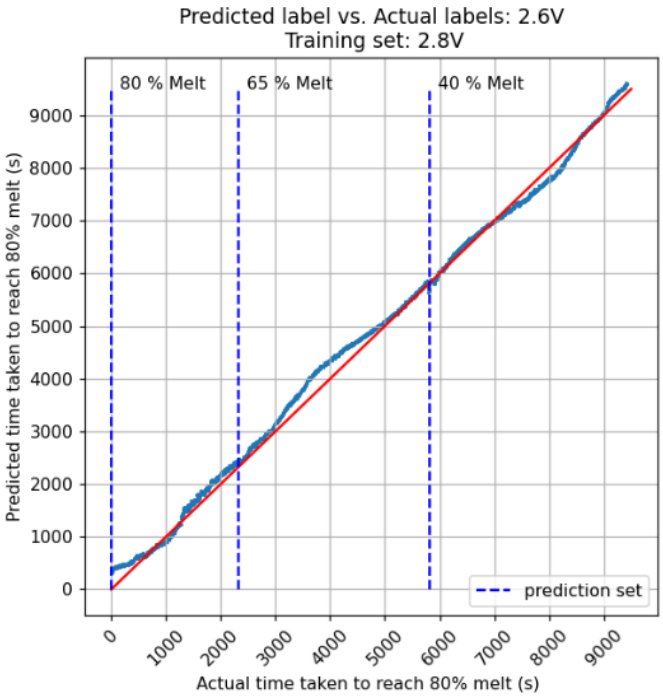

Fig 17 Scatter plot comparing the ANN predictions with experimental data for test data set of 2.6 V (and training dataset of 2.8 V).

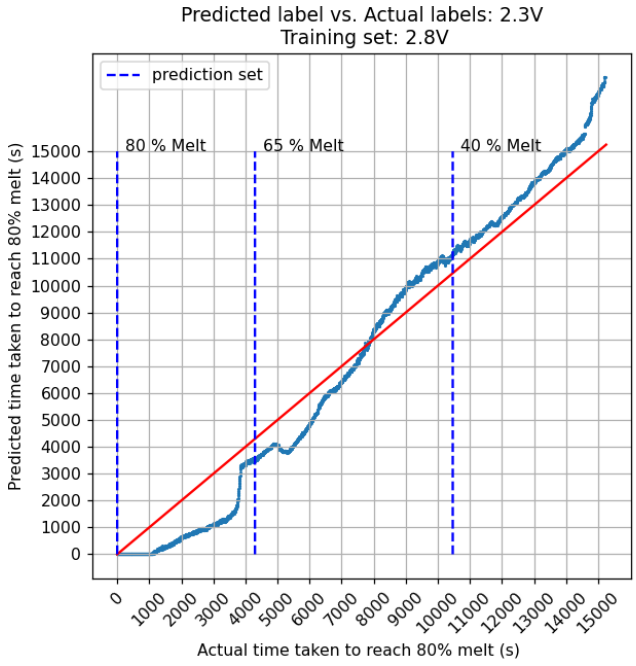

Fig. 18 Scatter plot comparing the ANN predictions with experimental data for test data set of 2.3 V (and training dataset of 2.8 V).

Table 3 Average absolute error in predictions during the last 1800 seconds before 80% melt (seconds)

		Training Set		
Prediction Set		***2.3V***	***2.6V***	***2.8V***
	2.3V		767.8	801.1
	2.6V	681.7		132.3
	2.8V	475.4	60.2	

An experiment with a 2.6V heater voltage with uncalibrated K-type thermocouples (instead of T-type) was conducted to further investigate the efficacy of this method implemented in this study. As expected from the previous graphs, the ANN trained with the 2.8 V dataset performs better than the ANN trained on the 2.3 V dataset. The average deviation for the predictions of the ANN trained on the 2.3 V dataset is 960 s (in the last half an hour). The same metric for the predictions of the ANN trained with the 2.8 V dataset is only 269 s. These errors are of the same order of magnitude as the predictions obtained from the calibrated dataset. We can thus say that the prediction accuracy of the method is insensitive to the malfunctioning of the sensors, i.e., the thermocouples. Hence, this demonstrates that the technique yields reliable outcomes even if the thermocouples are not calibrated (or inaccurately calibrated). The scatter plots are shown in Fig. 19 and Fig. 20.

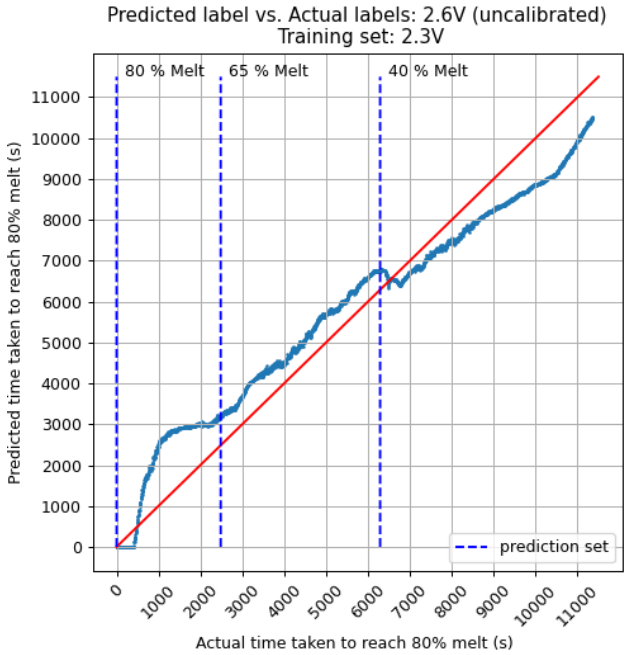

Fig. 19 Scatter plot comparing the ANN predictions with experimental data for test data set of 2.6 V with uncalibrated K-type thermocouples (and training dataset of 2.8 V).

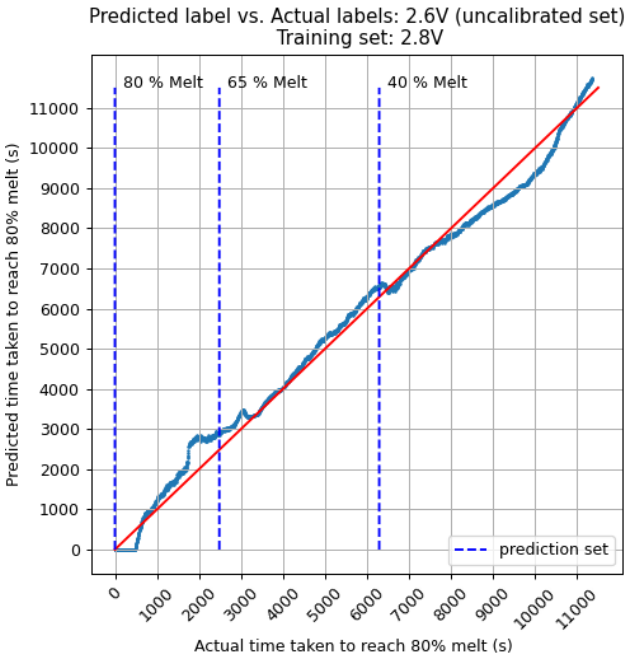

Fig. 20 Scatter plot comparing the ANN predictions with experimental data for test data set of 2.6 V with uncalibrated K-type thermocouples (and training dataset of 2.3 V).

Conclusion and Future Directions

The efficacy of using Deep Learning model for temporal predictions during melting of PCM was explored in this study to demonstrate the feasibility of this approach and with the aim of enhancing the performance of a PCM based TES system (e.g., to improve system reliability while also augmenting the effective energy storage capacity). Highly accurate predictions were achieved on the predicted time for realizing 90% melt fraction using a Feedforward Multilayer Perceptron Network. Although significant deviations were present in the middle stages of the cycle, the error was lower in the later stages of the cycle. The accuracy of predictions for 90% melt fraction are higher than that of 80% melt fraction. A strength of this method is that it is independent of the absolute values of the temperatures. This implies that even if a thermocouple is wrongly calibrated (or if the thermocouple calibration is compromised), the network would still be able to achieve fairly accurate time predictions. Another advantage is that the method does not demand additional equipment or nucleating agents. The ability to make apriori predictions holds significance as it enables a successful implementation of the cold finger technique. Supercooling is thus avoided, leading to an improved transient performance of the TES platform. High storage capacity provided by the inorganic PCMs can be effectively utilized without the reliability issues. This method can be applied to a commercial storage platform as there is no need for additional infrastructure besides a temperature measurement and acquisition system. A parametric optimization of the neural network is a further avenue to be explored. Additional studies are currently underway to forecast the time to reach melt fraction in the 95-100% range. In this endeavor, there is a preference

for underprediction (rather than over-predicting the required time to reach a desired melt fraction). For example, we would like to avoid an overprediction of the time to reach 99% melt. This is due to catastrophic failure considerations (since complete melting is likely to cause the PCM to solidify only after a certain degree of supercooling is achieved). On the other hand, if the time is underpredicted, a portion of the PCM will be solid (unmelted) and serve as the nucleation front when the PCM temperature is reduced to the melting point - thus obviating the need for supercooling for initiating nucleation and initiation of the solidification front (however, there will be a marginal sacrifice in the net energy storage capacity while improving system reliability).

APPENDIX K

RESULTS FROM ARTICLE UNDER REVIEW

"Exploring Efficacy of Machine Learning/ ML (Artificial Neural Networks/ ANN) for Enhancing Reliability of Thermal Energy Storage (TES) Platforms Utilizing Phase Change Materials (PCM)", Authors: G. Ren, A. Chuttar, and D. Banerjee

In order to observe how training data sets could affect the accuracy and reliability of the predictions from the ANN model, all of the collected data sets were categorized into six groups for training the ANN model, and are listed below:

- Group I: 2.6 Volt (low noise) experiment data sets containing two sets of data with a total of 4657 data points.
- Goup II: 2.8 Volt (low noise) experiment data sets containing two sets of data with a total of 3771 data points.
- Group III: 2.6 and 2.8 V (low noise) experiment data sets containing four sets of data with a total of 8428 data points (combination of Group I and II).
- Group IV: 2.6 V (low and high noise) experiment data sets containing four sets of data with a total of 10474 data points.
- Group V: 2.8 Volt (low and high noise) experiment data sets containing four sets of data with a total of 6975 points of data.
- Group VI: 2.6 and 2.8 Volt (low and high noise) experiment data sets containing eight sets of data with a total of 17449 data points (combination of group Group IV and V).

Three sub-sections within the "Results and Discussions" section provide a detailed description of the effects of using different training data sets on the efficiacy of the predictions obtained from the ANN model:

- Part A demonstrates the efficacy of the predicitons by utilizing only low noise training data sets (from Groups I, II, and III).
- Part B demonstrates the efficacy of the predicitons by utilizing both low noise and high noise training data sets (from Groups IV, V, and VI).
- Part C, in contrast, demonstrates the sensitivity of the predictions to variations in experimental procedures (i.e., using different power inputs) and the size of data sets (which also includes all the groups of training data ranging from Groups I-VI).

Results and Discussions

Part A:

Results obtained by using Group I, II, and III for training data - were analyzed. Thus, errors in the predicted values by using low noise training data sets exclusively – for different values of power input (2.6 V and 2.8 V) were implemented and compared with actual experimental data (for 2.7 V).

The ANN model was trained by using data obtained from the 2.6 V experiments with low noise (Group I). The predicted time for reaching 90% melt fraction (for power input of 2.7 V) was plotted as a function of the actual time required to reach 90% melt-fraction and are plotted in Figure 1.

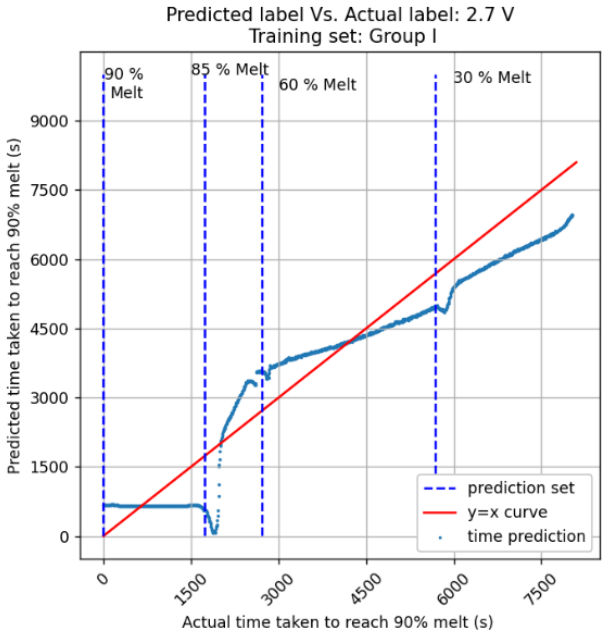

Figure 1: Group-I Training Data. Comparison of results predicted for 2.7 V experiments.

The plot shows that the ANN model underpredicts the time required to reach 90% melt by 930 s ~ 1090 s when the melt fraction is less than 30%. The error in the predictions from ANN model are lowest when the melt fraction progresses from 30% to 60%. However, in this range of melt fraction the ANN model progresses from underprediction (by ~ 660 s) to over-prediction (by ~2040 s). When the melt fraction progresses from 60% to 85% there is a sharp decrease in the plot, showing that the error in the prediction from the ANN model progresses from 2040 s over-prediction to ~1100 s underprediction. When the actual time required to reach 90% melt (value on the abscissa) has a value of 1700 s, the plot undergoes a quick recovery and virtually becomes a flat line (almost horizontal line) – showing that the predicted value to reach 90% melt (value on the ordinate) remains virtually unchanged at 1700 s, and in turn, intersecting with red line (which has a slope of 1, i.e., an angle of 45°) for a value of 630 s on the abscissa. The plot shows that from the

beginning of the melting process to a melt fraction of 60%, the values predicted by the ANN model for the 2.7 V experiments (using training data set of Group I) are accurate to within 18 minutes for a total melting time of 9286 seconds or approximately 155 minutes (and for the actual time to reach 90% melt fraction being 8036 seconds or 134 minutes). However, there is a sudden drop in the prediction accuracy when the melt fraction ranges between 60% and 85%, where the error in the predictions can be as high as 2040 s or 34 minutes. This shows that the efficacy of the predictions from the ANN model is degraded in the melt fraction ranging from 60% to 85% for 2.7 V experiments (when trained using Group 1 data set). The values predicted by the ANN model exceed the actual values (i.e., overprediction occurs) when the values on the abscissa are less than 630s (or approximately 11 minutes). This shows that the predictions from the ANN model should be discarded when the predicted values to reach 90% melt fraction are below 11 minutes (i.e., to avoid catastrophic failure of the TES platform). This also shows that the predictions are most reliable when the melt fraction is less than 60% and it is better to avoid any reliance on the model predictions for melt fractions exceeding 60% (or value of the ordinate less than 2700 s or approximately 45 minutes away from reaching 90% melt fraction). Hence, the predictions are accurate to within 18 minutes as long as the predicted values are more than 45 minutes. This anomalous trend in prediction capability of the ANN model (i.e., the accuracy of the prediction degrades when the predicted values are less than 1 hour to reach 90% melt fraction) can be ascribed to the distortions in the experimental data that occur during the final stages of the melt process. During the final stages of the melting process, a part of the melted PCM rises to the top surface and comes in contact with the thermocouples located at higher elevation (e.g., thermocouples located

at heights corresponding to melt fractions of 85% or higher). As a result, the thermocouples record oscillating values of temperature during the final stages of the melting process (i.e., within an hour of reaching 90% melt fraction). Therefore, this extraneous rise in the noise in the recorded signals (which is unavoidable with the current experimental apparatus) compromises the accuracy of the predictions obtained from the ANN model since the training data set inherently suffers from these types of distortions.

The ANN model was trained by using data obtained from the 2.8 V experiments with low noise (Group II). The predicted time for reaching 90% melt fraction was plotted as a function of the actual time required to reach 90% melt fraction in Figure 2.

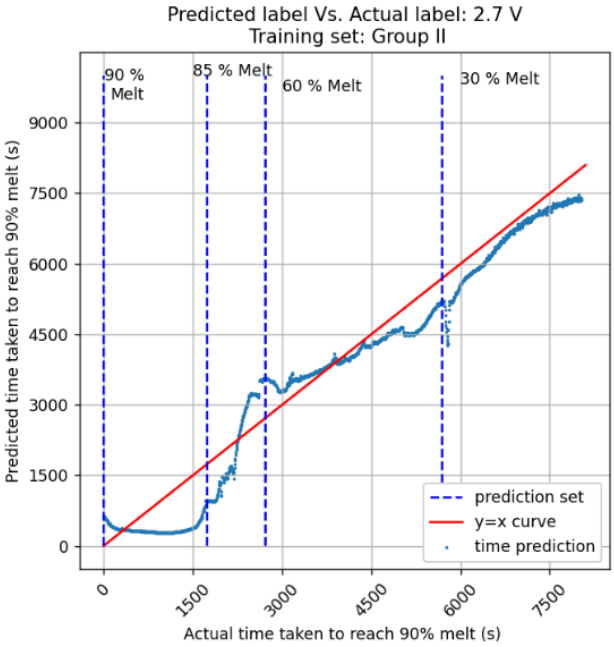

Figure 2: Group-II Training Data. Comparison of results predicted for 2.7 V experiments.

The plot shows that the ANN model underpredicts the time required to reach 90% melt by 120 s ~ 1530 s when the melt fraction is less than 30%. The sudden drop of the prediction accuracy at the actual time required to reach 90% melt (value on the abscissa)

occurs at value of 5770 s. The error in the predictions from ANN model are lowest with high precision when the melt fraction progresses from 30% to 60%. However, in this range of melt fraction the ANN model progresses from underprediction (by ~ 490 s) to over-prediction (by ~830 s). When the melt fraction progresses from 60% to 85% there is a continuous decrease in the plot, showing that the error in the prediction from the ANN model progresses from 880 s over-prediction to ~ 800 s underprediction. When the actual time required to reach 90% melt (value on the abscissa) has a value of 1300 s, the plot becomes a flat line virtually (almost horizontal line) – showing that the predicted value to reach 90% melt (value on the ordinate) remains virtually unchanged at 1300 s, and in turn, intersecting with red line (which has a slope of 1, i.e., an angle of 45°) for a value of 350 s on the abscissa. The plot shows that from the beginning of the melting process to a melt fraction of 60%, the values predicted by the ANN model for the 2.7 V experiments (using training data set of Group II) are accurate to within 25 minutes for a total melting time of 9286 seconds or approximately 155 minutes (and for the actual time to reach 90% melt fraction being 8036 seconds or 134 minutes). However, there is a sudden drop in the prediction accuracy when the melt fraction ranges between 60% and 85%, where the error in the predictions can be as high as 1120 s or 19 minutes. This shows that the efficacy of the predictions from the ANN model is degraded in the melt fraction ranging from 60% to 85% for 2.7 V experiments (when trained using Group II data set). The values predicted by the ANN model exceed the actual values (i.e., overprediction occurs) when the values on the abscissa are less than 310s (or approximately 5 minutes). This shows that the predictions from the ANN model should be discarded when the predicted values to reach 90% melt fraction are below 5 minutes (i.e., to avoid catastrophic failure of the TES

platform). This also shows that the predictions are most reliable when the melt fraction is less than 60% and it is better to avoid any reliance on the model predictions for melt fractions exceeding 60% (or value of the ordinate less than 2700 s or approximately 45 minutes away from reaching 90% melt fraction). Hence, the predictions are accurate to within 5 minutes as long as the predicted values are more than 45 minutes. This unexpected trend in prediction capability of the ANN model (i.e., the accuracy of the prediction degrades when the predicted values are less than 45 minutes to reach 90% melt fraction) can be ascribed to the distortions in the experimental data that occur during the final stages of the melt process. Reason for this discrepancy is the same as previously stated for results obtained in Group I predictions.

The ANN model was trained by using data obtained from the 2.6 and 2.8 V experiments with low noise (Group III). The predicted time for reaching 90% melt fraction was plotted as a function of the actual time required to reach 90% melt fraction in Figure 3.

The plot shows that the ANN model oscillated between underprediction and overprediction. The plot starts with underprediction of 530 s, then proceeds to an overprediction of 310 s, eventually reaches underprediction of 1410 s. The sudden drop of the prediction accuracy is observed at the actual time required to reach 90% melt (value on the abscissa) corresponding to a value of 5770 s. The error in the predictions from ANN model are lowest (i.e., with high precision) when the melt fraction progresses from 30% to 60%. However, in this range of melt fraction the ANN model progresses from mostly underprediction (by ~ 900 s) to short period of over-prediction (by ~950 s). When the melt fraction progresses from 60% to 85% there is a rapid decrease in the ordinate values in the

plot, showing that the error in the prediction from the ANN model progresses from ~ 950 s over-prediction to ~ 1630 s underprediction. When the actual time required to reach 90% melt (value on the abscissa) has a value of 1210 s, the plot becomes a flat line virtually (almost horizontal line) – showing that the predicted value to reach 90% melt (value on the ordinate) remains virtually unchanged at 1210 s, and in turn, intersecting with the red line (which has a slope of 1, i.e., an angle of 45°) for a value of 670 s on the abscissa. The plot shows that from the beginning of the melting process to a melt fraction of 60%, the values predicted by the ANN model for the 2.7 V experiments (using training data set of Group III) are accurate to within 16 minutes for a total melting time of 9286 seconds or approximately 155 minutes (and for the actual time to reach 90% melt fraction being 8036 seconds or 134 minutes). However, there is a sudden drop in the prediction accuracy when the melt fraction ranges between 60% and 85%, where the error in the predictions can be as high as 1630 s or 27 minutes. This shows that the efficacy of the predictions from the ANN model is degraded in the melt fraction ranging from 60% to 85% for 2.7 V experiments (when trained using Group III data set). The values predicted by the ANN model exceed the actual values (i.e., overprediction occurs) when the values on the abscissa are less than 670 s (or approximately 11 minutes). This shows that the predictions from the ANN model should be discarded when the predicted values to reach 90% melt fraction are below 11 minutes (i.e., to avoid catastrophic failure of the TES platform). This also shows that the predictions are most reliable when the melt fraction is less than 60% and it is better to avoid any reliance on the model predictions for melt fractions exceeding 60% (or value of the ordinate less than 2700 s or approximately 45 minutes away from reaching 90% melt fraction). Hence, the predictions are accurate to within 16 minutes as

long as the predicted values are more than 45 minutes. These counter-intuitive trends in the predicted values is caused by both: (1) anomalies in the experimental conditions; and (2) the enhanced noise levels caused by consolidating the various types of training data sets. The mixed training data sets could help improve the prediction accuracy when all the data sets possess similar melting characteristics (e.g., similar values for the toal durations of the experiments).

Figure 4 shows the plot of the error in the predicted values (obtained from the ANN model) as a function of the actual time required to achieve 90% melt fraction. These error values are plotted for three groups of numerical simulations: Group I (training of the ANN model that was performed using data from 2.6 V experiments for training), Group II (training of the ANN model that was performed using data from 2.8 V experiments) and Group III (training of the ANN model that was performed by combining data sets from Group I and Group II).

Plots for Group III show the best prediction (lowest error) when the melt fraction is less than 30%. However, for melt fraction less than 30% - the ANN model overpredicts (by less than 278 s); as observed in the plots for Group III case - where the actual time to reach 90% melt fraction ranges from 5900 s to 7200 s. However, for melt fraction less than 30%, the plots for Group II case show that they are always underpredicted by 180 s ~ 700 s (i.e., between 3 ~ 10 minutes). Hence, the predictions from Group II may be less accurate (as compared to Group III) – but are more reliable (as they do not suffer from over-prediction – as over-prediction is likely to cause catastrophic failure of the TES platform).

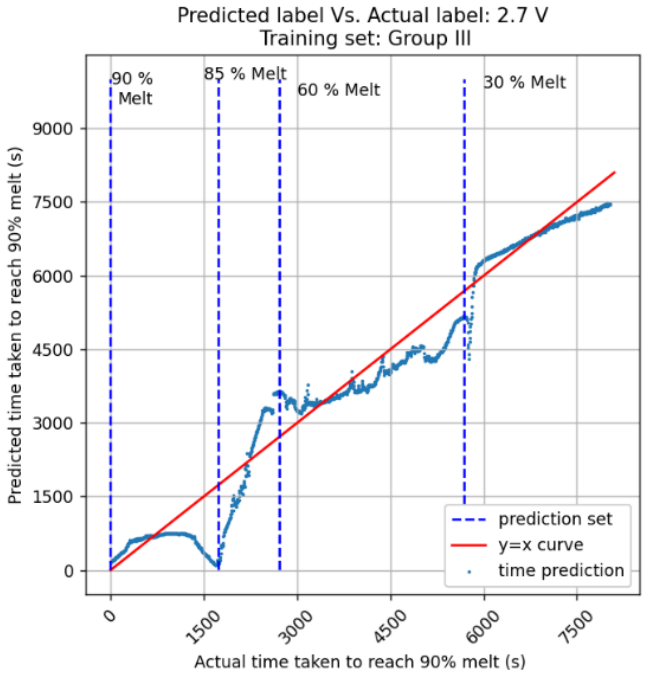

Figure 3: Group-III Training Data. Comparison of results predicted for 2.7 V experiments.

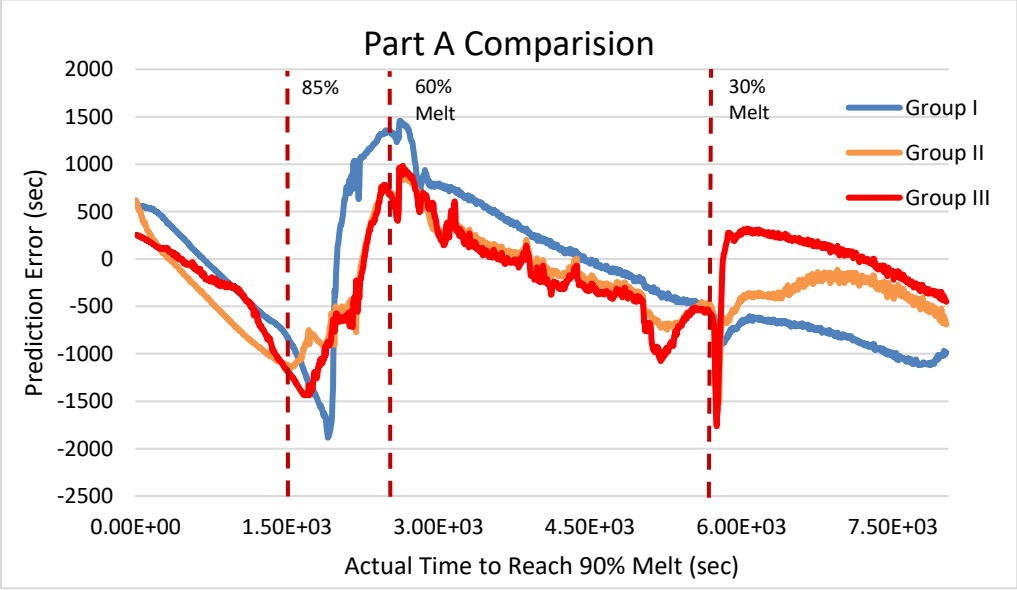

Figure 4: Comparison of error for predicted results for 2.7 V experiments (for training data using Groups I, II and III).

The only segments where Group II plots show over-prediction occur when the melt fraction is in the vicinity of 60% or 90%. In contrast, the plots for Group I oscillate frequently between under-prediction and over-prediction (with the highest error in the range of 1400 s (over-prediction) to 1880 s (under-prediction). Also, there is a sharp-rise and fall in the error values for the Group I plot when the melt fraction changes from 60% to 90%. As a result, predictions obtained for the Group I plot are deemed to be the most un-reliable. These trends can be rationalized by the fact that the total time to reach 100% melt fraction for the Group II data set (10799 s, 9849 s) is similar to that of the 2.7 V experiments (9286 s) while it is much larger in the Group I data set (12057 s and 13028 s). Group III data set being a combination of Group I and Group II data – therefore affords a more reliable prediction by virtue of the larger size of the training data used for calibrating the ANN model.

Part B:

Predictions obtained by using Group IV, V, and VI training data sets were analyzed. Thus, error in the predicted values that were obtained by using mixed (both low and high noise) training data sets at different power input values (2.6 V and 2.8 V) were compared.

The ANN model was trained by using data obtained from the 2.6 V experiments with low and high noise (Group IV). The predicted time for reaching 90% melt fraction was plotted as a function of the actual time required to reach 90% melt fraction in Figure 5. The plot shows that the ANN model oscillated between underprediction and overprediction when the melt fraction is less than 30%. The plots start with underprediction of ~ 360 s (6 minutes), then to an overprediction of ~ 760 s (8 minutes),

eventually reaching underprediction of ~990 s (16 minutes). The error in the predictions from ANN model are lowest with higher consistency when the melt fraction progresses from 30% to 60%. However, in this range of melt fraction the ANN model progresses from underprediction (by ~ 600 s) to overprediction (by ~ 930 s). When the melt fraction ranges from 60% to 85% there is a decrease in prediction accuracy in the plot, showing that the error in the prediction from the ANN model progresses from ~ 930 s overprediction to ~ 900 s underprediction. When the actual time required to reach 90% melt (value on the abscissa) has a value of 1380 s, the plot becomes a flat line virtually (almost horizontal line) – showing that the predicted value for reaching 90% melt (value on the ordinate) remains virtually unchanged at 1400 s, and in turn, intersecting with red line (which has a slope of 1, i.e., an angle of 45°) for a value of 710 s on the abscissa. The plot shows that from the beginning of the melting process to a melt fraction of 60%, the values predicted by the ANN model for the 2.7 V experiments (using training data set of Group IV) are accurate to within 15 minutes for a total melting time of 9286 seconds or approximately 155 minutes (and for the actual time to reach 90% melt fraction being 8036 seconds or 134 minutes). However, there is a sudden drop in the prediction accuracy at the melt fraction of 30% and 85%, where the error in the predictions can be as high as 990 s or 16 minutes. This shows that the efficacy of the predictions from the ANN model is degraded in the vicinity of the melt fraction values of 30% as well as 85% for the 2.7 V experiments (when trained using Group IV data set). The values predicted by the ANN model exceed the actual values (i.e., overprediction occurs) when the values on the abscissa are less than 710 s (or approximately 12 minutes). This shows that the predictions from the ANN model should be discarded when the predicted values reach 90% melt

fraction, i.e., corresponding to values below 12 minutes (i.e., to avoid catastrophic failure of the TES platform). This also shows that the predictions are most reliable when the melt fraction is between 30% and 60%.

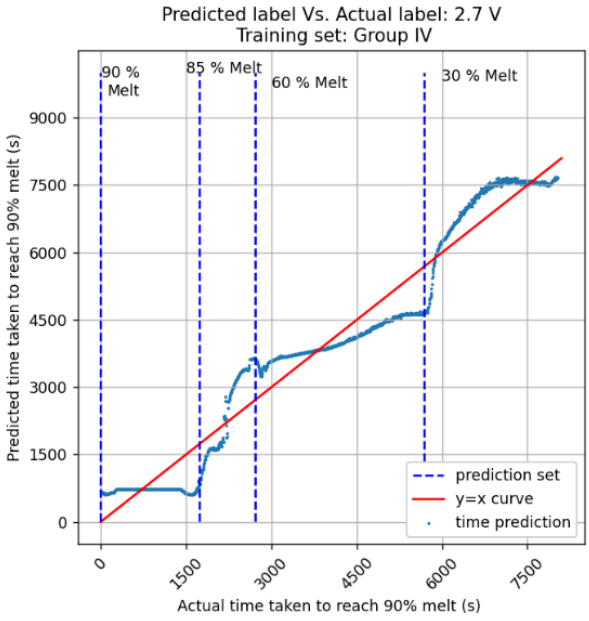

Figure 5: Group IV Training Data. Comparison of results predicted for 2.7 V experiments.

The ANN model was trained by using data obtained from the 2.8 V experiments with low and high noise (Group V). The predicted time for reaching 90% melt fraction was plotted as a function of the actual time required to reach 90% melt fraction in Figure 6. The plot shows that the results from the ANN model seem to demonstrate underprediction from the beginning of melting process until the melt fraction is in the vicinity of 90% (where the predicted values reach 190 s on the ordinate). The maximum error before 30% melt fraction is achieved is 1140 s or 19 minutes (underprediction). In contrast, the maximum underprediction in the predicted values (that occur for melt fractions ranging between 30% to 60%) is 780 s or 13 minutes. Thus, the error in the

predictions from ANN model are lowest when the melt fraction progresses from 30% to 60%. When the melt fraction is in the vicinity of 60% to 85% there is a decrease of prediction accuracy in the plots, showing that the error in the predictions is 1070 s or 18 minutes (underprediction). When the actual time required to reach 90% melt (value on the abscissa) has a value of 1230 s, the plot becomes a flat line virtually (almost horizontal line) – showing that the predicted value to reach 90% melt (value on the ordinate) remains virtually unchanged at 1230 s, and in turn, intersecting with red line (which has a slope of 1, i.e., an angle of 45°) for a value of 440 s on the abscissa. The plot shows that from the beginning of the melting process to a melt fraction of 85%, the values predicted by the ANN model for the 2.7 V experiments (using training data set of Group V) are accurate to within 18 minutes for a total melting time of 9286 seconds or approximately 155 minutes (and for the actual time to reach 90% melt fraction being 8036 seconds or 134 minutes). However, there is a sudden drop in the prediction accuracy before the melt fraction met 30%, where the error in the predictions can be as high as 1140 s or 19 minutes. This shows that the efficacy of the predictions from the ANN model is degraded for the values of melt fraction in the vicinity of 30% as well as 85% for the 2.7 V experiments (when trained using Group V data set). The values predicted by the ANN model exceed the actual values (i.e., overprediction occurs) when the values on the abscissa are less than 190 s (or approximately 3 minutes). This shows that the predictions from the ANN model should be discarded when the predicted values to reach 90% melt fraction are below 3 minutes (i.e., to avoid catastrophic failure of the TES platform). This also shows that the predictions are most reliable from the beginning of melting process to melt fraction of 85%. This overprediction at the end of the melting cycle can be explained as previously

stated in Group IV. The mixed 2.8 V training data sets successfully made the prediction from oscillating between overprediction and underprediction to only underprediction during most of the melting process. This proves that larger volume of data sets could reduce the prediction error.

The ANN model was trained by using data obtained from the 2.6 and 2.8 V experiments with low and high noise (Group VI). The predicted time for reaching 90% melt fraction was plotted as a function of the actual time required to reach 90% melt fraction in Figure 7. The plot shows that the ANN model underpredicts and overpredicts the time required to reach 90% melt by 340 s and 190 s when the melt fraction is less than 30%. The error in the predictions from ANN model are lowest when the melt fraction progresses from 30% to 60%. However, in this range of melt fraction the ANN model progresses from underprediction (by ~ 660 s) to over-prediction (by ~ 610 s). When the melt fraction progresses from 60% to 85% there is a sharp decrease in the plot, showing that the error in the prediction from the ANN model progresses to ~1100 s (underprediction). When the actual time required to reach 90% melt (value on the abscissa) has a value of 1540 s, the plot undergoes a quick recovery and keeps decreasing in prediction error. Consequently, it intersects with red line (which has a slope of 1, i.e., an angle of 45°) for a value of 620 s on the abscissa. The plot shows that from the beginning of the melting process to a melt fraction of 60%, the values predicted by the ANN model for the 2.7 V experiments (using training data set of Group VI) are accurate to within 10 minutes for a total melting time of 9286 seconds or approximately 155 minutes (and for the actual time to reach 90% melt fraction being 8036 seconds or 134 minutes). However, there is a rapid drop in the prediction accuracy when the melt fraction ranges between 60%

and 85%, where the error in the predictions can be as high as 1100 s or 18 minutes. This shows that the efficacy of the predictions from the ANN model is degraded in the melt fraction ranging from 60% to 85% for 2.7 V experiments (when trained using Group VI data set). The values predicted by the ANN model exceed the actual values (i.e., overprediction occurs) when the values on the abscissa are less than 140s (or approximately 2 minutes). This shows that the predictions from the ANN model should be discarded when the predicted values to reach 90% melt fraction are below 2 minutes (i.e., to avoid catastrophic failure of the TES platform). This also shows that the predictions are most reliable and accurate when the melt fraction is less than 60% and it is better to avoid any reliance on the model predictions for melt fractions between 60% and 85% (or value of the ordinate between 2700 s and 1730 s or approximately 30 – 45 minutes away from reaching 90% melt fraction). Thus, the predictions are accurate to within 10 minutes if the predicted values are more than 30 minutes.

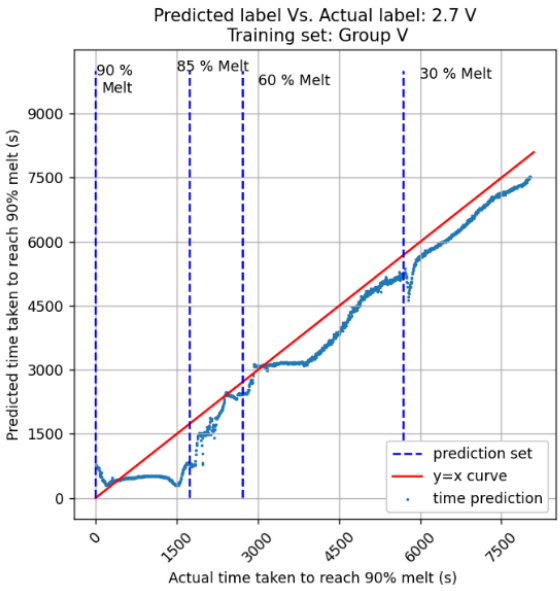

Figure 6: Group V Training Data. Comparison of results predicted for 2.7 V experiments.

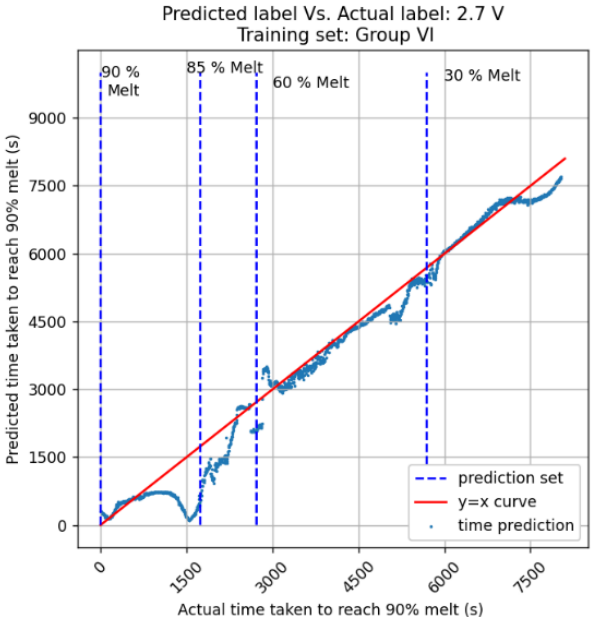

Figure 7: Group VI Training Data. Comparison of results predicted for 2.7 V experiments.

Figure 8 presents the plot of the error in the predicted values (obtained from the ANN model) as a function of the actual time required to achieve 90% melt fraction. These error values are plotted for three groups of numerical simulations: Group IV (training of the ANN model was performed by data from 2.6 V experiments with low and high noise), Group V (training of the ANN model was performed by data from 2.8 V experiments with low and high noise) and Group VI (training of the ANN model was performed by using combined data sets from Group IV and Group V). Plots for Group VI shows the best prediction (lowest error) throughout the entire melting process (until 90% melt fraction). As shown in Figure 8, for melt fraction less than 30%, the ANN model overpredicts (by less than 190 s); as observed in the plots for Group VI case - where the actual time to reach 90% melt fraction ranges from 5900 s to 7200 s. The sudden rise and fall in prediction error in the vicinity of melt fraction of 60% and 90% (with maximum overprediction of

600 s and under prediction of 1436 s) is lower compared with that of Group IV. Also, for melt fraction less than 30%, the plots for Group V case show that they are always underpredicted by 320 s ~ 1140 s (i.e., between 5 ~ 19 minutes). Hence, the predictions from Group V may be less accurate (as compared to Group VI) – but are more reliable (as they do not suffer from overprediction because overprediction is likely lead to catastrophic failure of the TES platform). The only segments where Group V plot indicates overprediction is around the melt fraction of 60% and 90%. In contrast, the plots for Group IV oscillate frequently between underprediction and overprediction with the maximum overprediction of 1000 s and underprediction of 1085 s. Also, there is a large rise and fall in the error values for the Group IV plot when the melt fraction progresses from 60% to 90%. As a result, predictions obtained from the Group IV plots are degraded substantially and are therefore considered to be the most unreliable. These trends can be explained by the fact that the total time to reach 100% melt fraction for the Group V dataset (10799 s, 9849 s, 8458 s, and 8397 s) is similar to that of the 2.7 V experiments (9286 s) while it is much different in the Group IV dataset (12057 s, 13028 s, 11147 s, and 10858 s). Group VI data set is a combination of Group IV and Group V data, and it provides a more reliable and accurate prediction. Therefore, it proves that by consolidating a larger training data set (i.e., by almost quadrupling the data size) the accuracy of the predictions (i.e., forecasting) can be improved significantly (i.e., the error was minimized to less than 10 minutes) for melt fraction values less than 60% and predicted values being more than 1 hour (approximately).

Part C:

Prediction results for the 2.7 V experiments were obtained by using training data sets for the same power input conditions but with different size of input data sets (low noise data sets only as opposed to both low and high noise data sets) were analyzed. Thus, the effect of power input conditions (and the size of the training data sets) on prediction accuracy (and reliability of the predictions) were explored in this study. Figure 9 shows the plot of the error in the predicted values (obtained from the ANN model) as a function of the actual time required to achieve 90% melt fraction. These error values are plotted for two groups of numerical simulations: Group I (training of the ANN model was performed by utilizing data from 2.6 V experiments with low noise) and Group IV (training of the ANN model was performed by utilizing data from 2.6 V experiments with both low noise and high noise).

Plot for Group IV shows the best prediction (lowest error) when the melt fraction is less than 30%. However, for melt fraction less than 30%, the ANN model results are overpredicted (by 730 s) as observed in the plots for Group IV case: where the actual time to reach 90% melt fraction ranges from 5900 s to 7500 s. In contrast, for melt fraction less than 30%, the plots for Group I indicates that it is always underpredicted by 1120 s ~ 600 s (i.e., between 29 ~ 10 minutes). Thus, the predictions from Group I is less accurate (as compared to Group VI) but are more reliable (since overprediction will lead to a catastrophic failure of the TES platform). As melt fraction progresses from 30 % to higher values, the accuracy of the predictions utilizing Group IV data set is observed to be enhanced (until the actual time to reach 90% melt-fraction is 3826 s). This is in sharp contrast to the predictions obtained from Group I. Also, there is a sharp-rise and fall in the

error values for the Group I plot when the melt fraction changes from 60% to 90%. As a result, predictions generated by Group I are considered to be the less accurate. These trends show that larger training data sets can be helpful for improving the prediction accuracy even in the presence of minor levels of noise within the training data sets.

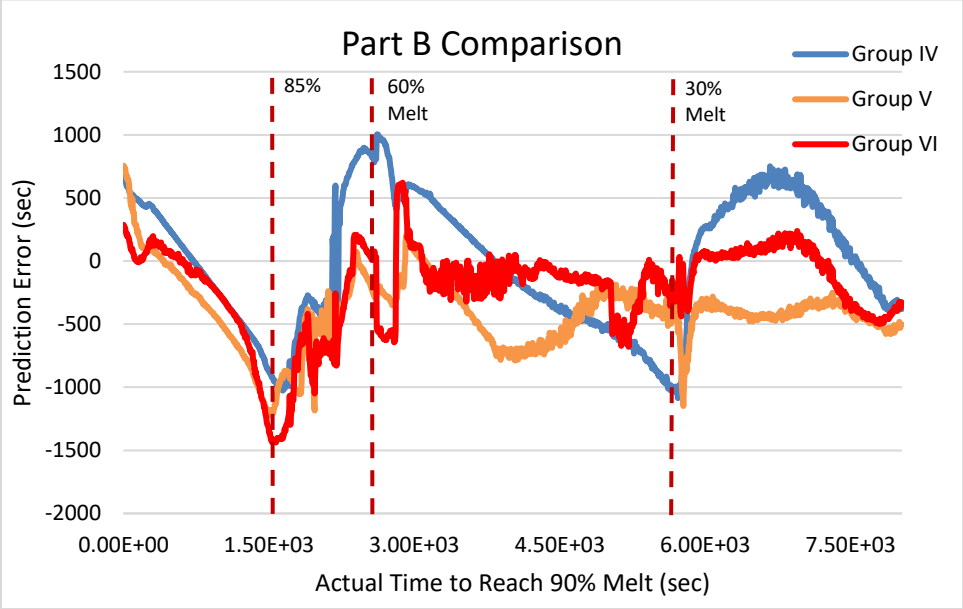

Figure 8: Comparison of error for predicted results for 2.7 V experiments (for training data using Groups IV, V and VI).

Figure 10 shows the plot of the error in the predicted values (obtained from the ANN model) as a function of the actual time required to achieve 90% melt fraction. These error values are plotted for two groups of numerical simulations: Group II (training of the ANN model was performed by data from 2.8 V experiments with low) and Group V (training of the ANN model was performed by data from 2.8 V experiments with low and high noise). Since results from Group V yield underprediction throughout the entire melting process (except the last 400 s), plot for Group V shows the best quality of

prediction: for both accuracy and reliability. However, for melt fraction less than 30%, the ANN model results show underprediction of 1147 s as observed in the plots for Group IV case where the actual time to reach 90% melt fraction is 5775 s. In contrast, for melt fraction less than 30%, prediction generated by Group II results show underprediction of 1454 s, where the actual time to reach 90% melt fraction is 5766 s. Hence, the prediction from Group II is less accurate as compared to that of Group V. After melt fraction of 30%, results from Group II oscillates between overprediction (with maximum of 909 s) and underprediction (with maximum of 1164 s). However, results from Group V are underpredicted within that range. Hence, results from Group II are deemed to be less accurate and less reliable.

Figure 11 shows the plot of the error in the predicted values (obtained from the ANN model) as a function of the actual time required to achieve 90% melt fraction. These error values are plotted for two groups of numerical simulations: Group III (training of the ANN model was performed by using data from 2.6 and 2.8 V experiments with low noise) and Group V (training of the ANN model was performed by using data from 2.6 and 2.8 V experiments with low and high noise). Plot for Group VI are observed to provide results with the best quality, i.e., for both accuracy and reliability. For melt fraction less than 30%, results from both Group III and VI oscillate (i.e., switch from underprediction to overprediction) within different range of values. Group III results show a maximum underprediction of 1764 s and overprediction of 313 s. In contrast, Group VI results show only a maximum underprediction of 475 s and overprediction of 238 s. From melt fraction ranging from 30% to 60%, Group VI prediction presents the maximum underprediction of 656 s and overprediction of 588 s and a minimum error from 4286 s to 3076 s for the

values of time required to reach 90% melt fraction (abscissa value). However, Group III prediction shows maximum underprediction of 1033 s and overprediction of 822 s. Thus, the prediction from Group III is less accurate and reliable as compared to Group VI. These trends demonstrate that larger training data sets with different values of power inputs and a larger training data set (with low levels of noise) can be helpful for improving prediction accuracy and reliability.

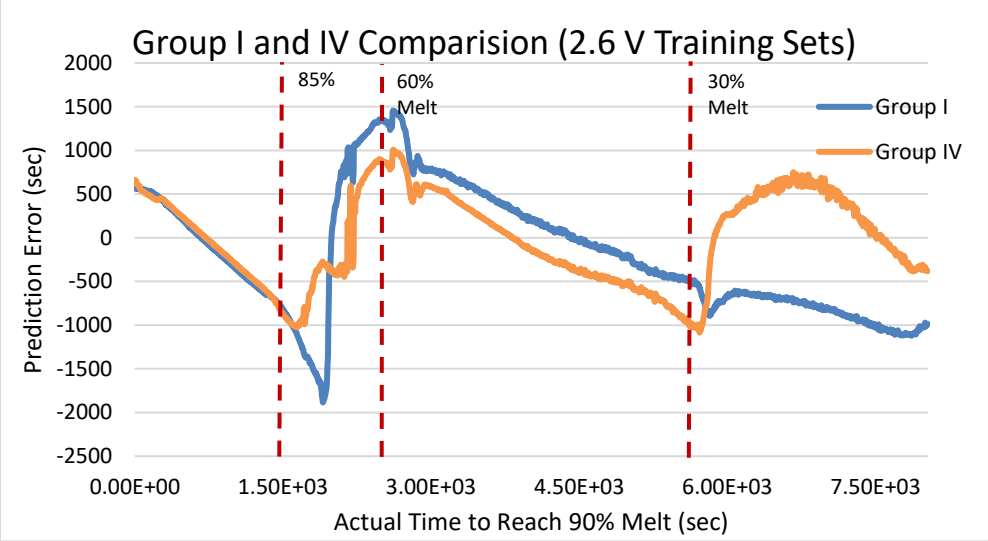

Figure 9: Comparison of error for predicted results for 2.7 V experiments (for training data using Groups I and IV).

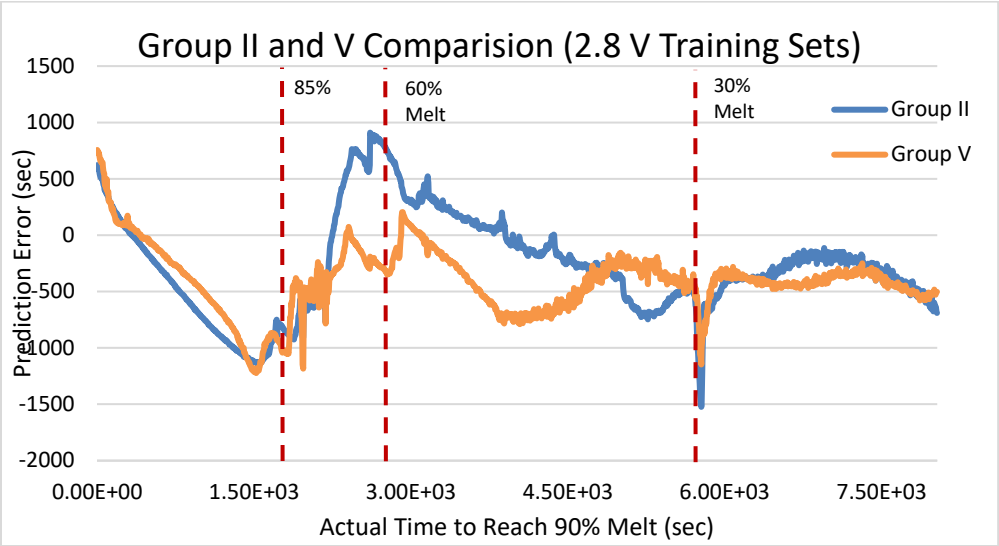

Figure 10: Comparison of error for predicted results for 2.7 V experiments (for training data using Groups II and V).

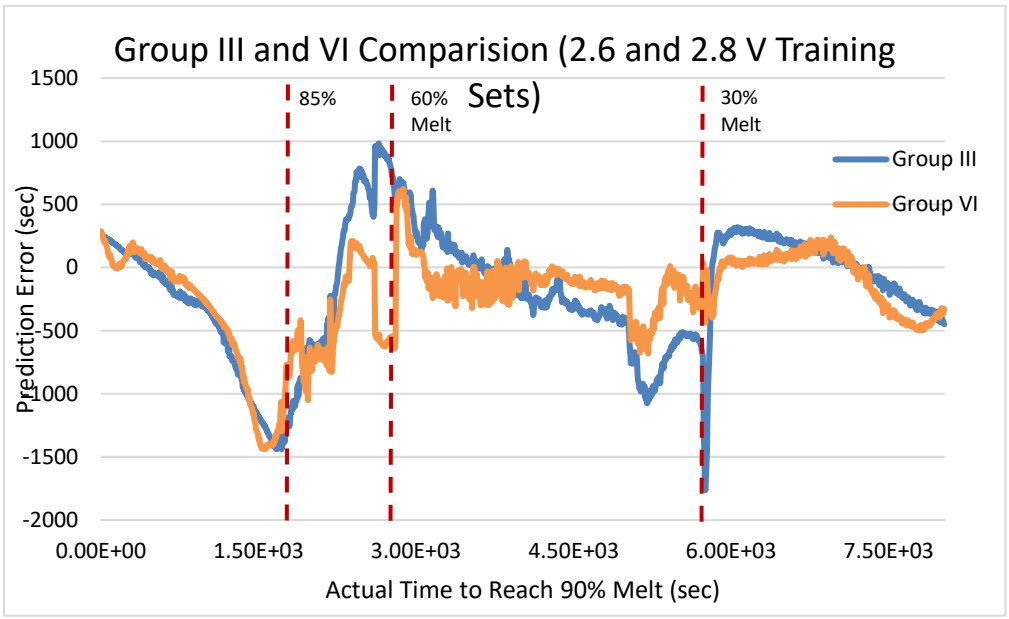

Figure 11: Comparison of error for predicted results for 2.7 V experiments (for training data using Groups III and VI).

Conclusion

In this study, we developed and demonstrated the efficacy for achieving real-time prediction of the actual time remaining to reach a predefined melt fraction (chose by the user) for a candidate PCM during the melting process in a candidate LHTESS. A machine learning (ML) based approach utilizing artificial neuron network (ANN) is explored in this study for determining the efficacy and reliability for different types of training data. The purpose behind this endeavor is to improve the reliability of the ANN model for predicting the time remaining to reach a predefined melt fraction. For instance, highly accurate predictions were achieved for predicting the time remaining for realizing 90% melt fraction at any instant during an experiment (i.e., for real-time predictions during operations), using a feedforward MLP network (also termed as "FMLPN"). The results obtained in this study show that the reliability of this ANN model is maximized when size of the training data set is large (total eight sets of training data), and for conditions where each individual training data set is mutually consistent (i.e., they possess similar melting characteristics). Additionally, the results are almost insensitive to the variations in the different power input conditions. There is remarkable improvement in the prediction accuracy and reliability: provided that the data sets have similar melting characteristics (such as the value of total duration of the melting cycle). An eminent strength of this method is that training data sets obtained for a given set of power input conditions can be used to predict the melting time with high accuracy for another power input condition. For example, training data (from experiments conducted for the input voltage of 2.6 V and 2.8 V) can be used to predict the target values of melt fraction for the 2.7 V experiments with high accuracy (i.e., predictions are within 10 minutes of actual values for duration of

experiments exceeding 2 hours). Also, the large training data set (with both low noise and high noise values) is observed to yield the best prediction accuracy and reliability. Therefore, these results will enable users of this approach to determine what type of data sets provide the best efficacy for the forecasting with sufficient reliability.

The techniques developed in this study therefore demonstrate the ability to predict the actual time remaining to reach the predefined melt fraction (e.g., 90%) with sufficient precision and accuracy. This capability will therefore enable the successful execution of the cold finger technique (CFT) while maximizing energy storage capacity (with minimal impact on the power rating) and enhancing the reliability of real time operations of TES platforms that utilize PCMs. Since CFT mitigates the supercooling problem of PCM, solidification time of PCM can be reduced significantly. This study demonstrates the feasibility and efficacy of ANN techniques for predicting the actual time remaining to reach the predefined melt-fraction with sufficient precision - both accurately and reliably. Future studies are recommended that are focused on the influence of the consistency of the training data sets on the robustness of the predictions obtained from these ANN models. In order to have the most accurate and reliable predictions from the results obtained from the ANN models, consistent and repeatable training data sets are required for different levels of power input. This will enable the elimination of the overprediction problem (which will cause catastrophic failure of the TES platforms deploying CFT techniques).